Exploring Earth-Abundant Thermoelectrics

KIERAN SPOONER
UNIVERSITY COLLEGE LONDON

PRIMARY SUPERVISOR: PROFESSOR DAVID SCANLON
SECONDARY SUPERVISOR: PROFESSOR ROB PALGRAVE

A thesis submitted in partial fulfilment of the requirements for the degree of Doctor of Philospphy at University College London.

AUGUST 10, 2023

Declaration

I, *Kieran Bryce Spooner*, confirm that the work presented in this thesis is my own. Where information has been derived from other sources, I confirm that this has been indicated in the work.

. . . .

KIERAN BRYCE SPOONER
AUGUST 10, 2023

University College London

Abstract

As the need to eliminate and even draw down greenhouse gasses, chiefly CO_2 and CH_4, becomes ever more urgent, so too does the need for tools to generate renewable energy and simultaneously reduce our demand for it. Thermoelectrics tackle both problems: by definition, they can generate electricity directly from thermal energy, and through this process they could also recycle waste heat from our inefficient devices, which waste 50 % of their energy as heat. Much research has gone into thermoelectric materials in recent years, but the need for conflicting materials properties, including a high electrical conductivity and Seebeck coefficient but a low thermal conductivity, have meant high efficiencies are restricted to materials consisting of rare and toxic elements, precluding their use in the volumes required.

This thesis examines a number of potential earth-abundant thermoelectric materials. Through thorough observation of scattering sources for phonons and electrons, we discern if the materials will make effective thermoelectrics, and why. First we look at the effects of a complex structure, through $BaBi_2O_6$; and then take a more design-focused approach by looking at anion substitution to augment the transparent conducting oxide ZnO into Zn_2NX, X = Cl, Br, I. This allows the assessment of these design methods, and other emergent topics, so that still better thermoelectrics may be developed, perhaps in time to postpone the worst effects of the climate crisis.

Impact Statement

The latest Intergovernmental Panel on Climate Change report has warned that it is "almost inevitable" that we will breach the 1.5 °C of heating since pre-industrial levels target laid down by the 2015 Paris Agreement.[1–3] It also states that the current impacts of global heating are already worse than expected.[4] Furthermore, every fraction of a degree rise in temperature risks triggering climate tipping points,[5] where massive irreversible changes occur that risk further accelerating temperature rises in a potential cascade. Recent research suggests six of these tipping points are likely in the 1.5–2.0 °C warming range, including permafrost thawing, ice-shelf collapse and coral die-off.[6] It is therefore imperative that we urgently shift to renewable, carbon-neutral energy sources, for which thermoelectrics are highly interesting candidates.

As materials that convert heat into electricity, thermoelectrics could potentially harvest energy from any heat source, but beyond that they could recycle waste heat from electrical devices, buildings, or even humans and other animals, increasing efficiency and therefore reducing the increase of renewables required. Besides climatic necessities, thermoelectrics could have positive effects on society by contributing to a decentralised energy generation system for the common good, rather than the monopolised system of today which has lead to the cover-up of the climate crisis and many problems besides, which disproportionately affect the poorest.[7] Unfortunately, modern high-efficiency thermoelectrics are commonly composed of rare and/or toxic elements, such as PbTe and Bi_2Te_3, which prevents their wide-scale uptake. Therefore, this thesis aims to explore earth-abundant thermoelectric materials, helping to propose design principles and analysis methods that can help computationalists and experimentalists alike discover the next generation of scalable thermoelectric materials, as part of studying specific materials we hope will fulfil the dual necessities of efficiency and environmental friendliness.

Publications

Relating to thesis work

1. K. B. Spooner, A. M. Ganose, W. W. W. Leung, J. Buckeridge, B. A. D. Williamson, R. G. Palgrave and D. O. Scanlon, $BaBi_2O_6$: A Promising n-Type Thermoelectric Oxide with the $PbSb_2O_6$ Crystal Structure, *Chem. Mater.* **2021**, *33*, 7441.
2. K. B. Spooner, M. Einhorn, D. W. Davies and D. O. Scanlon, ThermoParser: Streamlined Analysis of Thermoelectric Properties, *in submission.*
3. K. B. Spooner and D. O. Scanlon, Investigating the Structures of the ZnO-Derived Nitrohalides Zn_2NX (X = Cl, Br, I), *in preparation*
4. K. B. Spooner and D. O. Scanlon, Thermoelectric Properties of the Mixed Anion Nitrohalides Zn_2NX (X = Br, I), *in preparation.*
5. K. B. Spooner and D. O. Scanlon, On the Efficient Calculation of Lattice Thermal Conductivity in Complex Materials, *in preparation.*
6. K. B. Spooner, S. R. Kavanagh, J. Willis and D. O. Scanlon, Defect Properties of the Mixed Anion Thermoelectric Zn_2NBr, *in preparation.*

Not relating to thesis work

7. K. B. Spooner, A. M. Ganose and D. O. Scanlon, Assessing the Limitations of Transparent Conducting Oxides as Thermoelectrics, *J. Mater. Chem. A* **2020**, *8*, 11948. [*]
8. K. Brlec, K. B. Spooner, J. M. Skelton and D. O. Scanlon,

---

[*] This paper was featured on the back cover.

$Y_2Ti_2O_5S_2$ — a Promising n-Type Oxysulphide for Thermoelectric Applications, *J. Mater. Chem. A* **2022**, *10*, 16813.

9. L. Herring–Rodriguez, K. B. Spooner, M. Einhorn and D. O. Scanlon, $Sr_2Sb_2O_7$: a Novel Earth Abundant Oxide Thermoelectric, *J. Mater. Chem. C* **2023**, *11*, 9124.

10. J. Willis, K. B. Spooner and D. O. Scanlon, On the Possibility of p-Type Doping in Barium Stannate, *accepted.*

11. D. Han, B. Zhu, Z. Cai, K. B. Spooner, S. S. Rudel, W. Schnick, T. Bein, D. O. Scanlon and H. Ebert, Discovery of Multi-Anion Antiperovskite X_6NFSn_2 (X = Ca, Sr) as Promising Thermoelectric Materials by Computational Screening, *in submission.*

12. S. Hachmioune, K. B. Spooner, A. M. Ganose, M. B. Sullivan and D. O. Scanlon, Exploring the Thermoelectric Potential of MgB_4: Electronic Band Structure, Transport Properties and Defect Study, *in preparation.*

13. W. Dou, K. B. Spooner, T. Niu, M. Zhou and D. O. Scanlon, Band Degeneracy Enhanced Thermoelectric Performance in $Sc_2Si_2Te_6$, *in preparation.*

ACKNOWLEDGEMENTS

First I would like to thank the prime mover of this project, Professor David Scanlon, who has nurtured me since my internship with expertise, encouragement and more belief in me than I ever mustered. I would also like to thank the original SMTGers, Doctors Adam Jackson, Alex Ganose, Ben Williamson and Chris Savory who also added significant knowledge and training. Next I thank the sometimes members of the thermoelectrics subgroup Warda Rahim, Luisa Herring Rodriguez, Sabrine Hachmioune and Bastien Grosso for fruitful discussions and occasionally willing lab-rattery. Most especially of those I thank my more frequent co-conspirators Maud Einhorn and Katarina Brlec, for much the same reasons. The other members of the SMTG also had valuable contributions, but I will single out Joe Willis, Seán Kavanagh and Bonan Zhu. While somewhat battery-oriented himself, Arthur Youd added no less valuable pastural contributions, alongside the aforementioned Katarina Brlec.

This work was made possible by the generous support of the European Research Council (grant 758345). It used a number of high-performance computing (HPC) facilities: via our membership of the UK's HEC Materials Chemistry Consortium, which is funded by EPSRC (EP/L000202, EP/R029431, EP/T022213), this work used the ARCHER and ARCHER2 UK National Supercomputing Services (http://www.archer.ac.uk and https://www.archer2.ac.uk); via the UK Materials and Molecular Modelling Hub for computational resources, MMM Hub, which is partially funded by EPSRC (EP/P020194 and EP/T022213), this work used the Thomas and Young HPCs; I acknowledge the use of the UCL Legion, Myriad, Grace and Kathleen High Throughput Computing Facilities (Legion@UCL, Myriad@UCL, Grace@UCL and Kathleen@UCL), and associated support services, in the completion of this work.

Last and by all means first, I would like to thank my mother and father, Natalie and Simon Spooner for supporting me for the last 27 years(!), and my sister Ashleigh Spooner for a slightly shorter period dependent on the onset of her sentience.

CONTENTS

VI Structural Stability of Zn_2NX

reality is for people who lack science

— not Hayao Miyazaki

Part I

Introduction

1 MOTIVATION

Since the link between atmospheric CO_2 and global temperatures was first drawn in 1895,[8,9] the global temperature has risen by 1.16 °C, with the hottest ten years all occurring since 2010.[10] This, and complex consequent effects, have been shown to bring inequitable pestilence,[11] famine,[12] war[13] and death, but technological advances are able to reduce these consequences.[13] An important preventative approach is to rapidly reduce and reverse greenhouse gas emissions, primarily CO_2 and CH_4, of which one of the most significant sources is the burning of fossil fuels. One of the main ways to do this is by the use of renewable energy technologies, such as solar, wind and hydropower, however renewables and nuclear currently only account for 23 % of global energy consumption (according to the substitution method, which accounts for inefficiencies in the combustion of fossil fuels).[14] Thermoelectrics are a renewable energy technology that converts heat into electricity, or vice versa. They are not currently in widespread use, which makes them an important candidate for study to diversify the available renewable energy sources. Additionally, as 50 % of generated energy wasted as thermal energy,[15] they open up a wide array of applications that other renewables do not have.

2 APPLICATIONS

While around 64 % of the global waste heat is from sources below 100 °C,[15] higher temperature sources are more tractable for thermoelectrics, as the Carnot efficiency (the efficiency of an ideal engine, $1 - \frac{T_C}{T_H}$, where T_C and T_H are the cold and hot side temperatures respectively[16]) is higher, assuming a constant cold side temperature (i.e. room temperature). This means that sources from 100–300 °C have the greatest *theoretical* potential for harvesting, with around 63 % of harvestable energy.[15] Practically though, it is also worth considering that the energy in higher temperature sources, such as industrial processes like steel forging,[17] is concentrated in a smaller area, hence less thermoelectric material is needed. Furthermore, thus far many of the highest performing thermoelectric materials have their highest efficiencies at temperatures in excess of 600 °C.

Due to the ubiquity of waste heat, there are many other applications for thermoelectrics. Small thermoelectric modules could be incorporated into the nearly-as-ubiquitous display screens, recycling some of their waste heat to increase efficiency and battery life. This could also be done with any number of electrical devices, or other objects. Even a sedentary computational chemist emits 116 W, which could provide a Watt or two for for a small wearable device operating well below the Carnot efficiency.[18] Ambient heat could be another source, for other small self-powering devices such as environmental sensors. Run in reverse, thermoelectric devices can use electrical current to move thermal energy across themselves, allowing them to be used for heating and cooling. One of the most common refrigeration methods today, evaporative cooling, has existed since at least fifth century BCE Iran,[19] although modern systems can be more clearly traced back to around 1755 CE work by William Cullen, John Hadley and one Benjamin Franklin.[20] Thermoelectric cooling offers several advantages over evaporative cooling: a solid state system requires no moving parts (e.g. fans), making them quiet and reliable: thermoelectric generators powered by nuclear batteries power the only artificial objects to have left our solar system, including Voyagers 1 and 2, which are still powered 46 years after launch.[21] They require no refrigerant gasses, which have variously been toxic, ozone depleting[22] and/or potent greenhouse gasses.[23] While these applications may not have a significant direct effect on the climate crisis (Montréal protocol withstanding), they could encourage competition over device efficiency and greater interest and therefore investment in the technology, accelerating more impactful applications.

More direct impacts might be felt from integrations with other emissions-free energy generation technologies. Thermoelectric generators have been shown to be able to work, sometimes even with enhanced efficiency, inside nuclear fission reactors,[24] where they could be used to reliably power monitoring devices to enhance safety and therefore uptake. Work has also been done studying the integration of thermoelectrics into photovoltaic cells. In a theoretical model of ideally efficient materials (where the thermoelectric material was represented as a Carnot engine and the photovoltaic operated at the detailed-balance limit[25,26]), the overall efficiency was raised from 33.2 % to 35 %, a relative increase of 5.4 % compared to just the photovoltaic.[27] The energy absorbed by the thermoelectric is greater than this increase, but is counteracted by the thermoelectric insulating the photovoltaic, reducing its ability to radiate excess heat, causing an increase in charge recombination and therefore decrease in efficiency.[28] Another method of increasing the efficiency of photovoltaics is placing them above bodies of water, in the whimsically named floatovoltaics. These utilise evaporative cooling by said water to reduce the aforementioned efficiency reduction of the photovoltaics, resulting in relative efficiency gains of around 2 % for a 5 °C temperature difference.[29] Combining these various technologies may provide ways to further enhance efficiencies — thermofloatovolatics may provide a greater temperature gradient for the thermoelectric rather than an efficiency boost for the photovoltaic, or concentrated solar may have a similar effect, but with the added benefit of less thermoelectric and photovoltaic materials needed. The ubiquity of heat enables a ubiquity of utility, and of course, research will be needed, both into materials and device architecture, the former of which we hope to help address here.

3 THERMOELECTRICITY

History of the Thermoelectric Effect

The study of thermoelectricity can be traced back to the discovery in 1794 by Allessandro Volta[30] that dead frogs would spasm when in water touched by the end of an iron rod which had been heated, but not when it was cooled. In 1825, Thomas Johann Seebeck[31] discovered the *thermomagnetischen Wirkung* when a loop composed of two rods of different metals joined end-on-end deflected a compass needle, which Hans Christian Ørsted[32,33] realised the following year to be more fundamentally the *thermélectriques* effect, which was later named after Seebeck as the Seebeck effect. The reverse process, transforming heat into electricity, is known as the Peltier effect, after its discoverer Jean Charles Athanase Peltier.[34]

Modern devices for both the Seebeck and Peltier effects are commonly thermocouples. This comes from the fact that they are made from two thermoelectric materials, one electron-conducting (n-type), and one hole-conducting (p-type). In both materials, when there is a temperature gradient the hot charge carriers move faster than the cold charge carriers, causing the rate of diffusion to be greater towards the cold end, resulting in a potential difference. When there is a potential difference, the holes move with it and the electrons counter to it as usual, transferring heat in the direction of the particle flow. In order for the the effects in the different materials not to cancel, the thermoelectric materials therefore need to be connected electrically in series, but thermally in parallel, as shown in Figure 3.1.

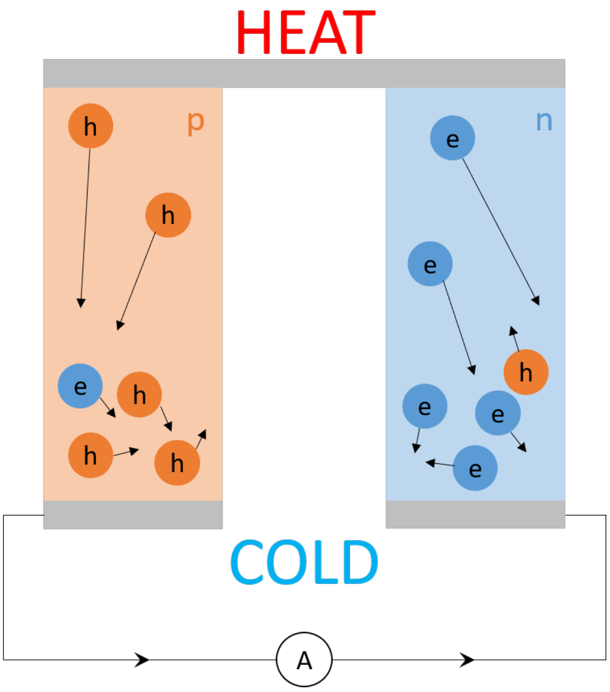

Figure 3.1: A thermocouple, the typical thermoelectric device architecture. Heating one side of a material causes the charge carriers at that end to move faster than those at the cold end, so they diffuse to the cold end, creating a potential difference. When connected into a circuit, this can generate a current. This is the Seebeck effect, the principle behind thermoelectric materials.

Theory

Mathematically, the Seebeck effect is quantified by the Seebeck coefficient (or thermopower), α, which is the ratio of the potential difference, ΔV, to the change in temperature that causes it, ΔT. For the purposes of calculating it, a more practical form is:

$$\alpha = \frac{\Delta V}{\Delta T} = \frac{2k_B^2 m^* T}{3e\hbar^2}\left(\frac{\pi}{3n}\right)^{\frac{2}{3}} \tag{3.1}$$

where k_B is the Boltzmann constant, m^* is the charge carrier effective mass (a measure of the mobility, low effective mass means more mobile, see Equation (3.4)), T is the absolute temperature, e is the fundamental charge, $\hbar$ is the reduced Planck constant and n is the carrier concentration. Here we see the Seebeck coefficient is dependent on temperature, leading to one last thermoelectric effect, the Thomson effect. This is when a single material can generate thermoelectric effects when under the influence of a temperature gradient and current, due to the high temperature areas having a higher Seebeck coefficient, generating more potential difference and therefore transferring more heat.[35] This also occurs in all thermoelectric systems, as all have a combination of temperature and electrical potential gradients.

The efficiency of a thermoelectric is quantified as its dimensionless figure of merit, ZT:

$$ZT = \frac{\alpha^2 \sigma T}{\kappa} \quad \text{where} \quad \kappa = \kappa_l + \kappa_e \tag{3.2}$$

where σ is the electrical conductivity and κ is the thermal conductivity, composed of the lattice (κ_l) and electronic (κ_e) components. The quantity $\alpha^2\sigma$ is known as the power factor (PF), and is often used as an analogue for ZT, where κ may be difficult to measure or calculate, or to separate it from the effects of varying κ, which can be easily engineered. This is related to the efficiency, η by:

$$\eta = \frac{T_h - T_c}{T_h} \left(\frac{\sqrt{1 + ZT} - 1}{\sqrt{1 + ZT} + \frac{T_C}{T_h}} \right), \tag{3.3}$$

where T_h and T_c are the hot and cold side temperatures, respectively. Looking at the electrical conductivity:

$$\sigma = ne\mu = \frac{ne^2\tau}{m^*} \tag{3.4}$$

where μ is the charge carrier mobility and τ is the charge carrier relaxation time, it is clear that the two components of the power factor are at odds: a high Seebeck coefficient requires a small number of poorly mobile charge carriers, while high electrical conductivity requires many low effective mass charge carriers. This is one of the major stumbling blocks for thermoelectrics research and contributes to the lack of high ZT materials.

The thermal conductivity is the other major factor. It is made up of a lattice component, transmitted by phonons (the quanta of lattice vibrations), and an electronic component, transmitted by electrons. The electronic component cannot be reduced without also reducing the electrical conductivity, as ex-

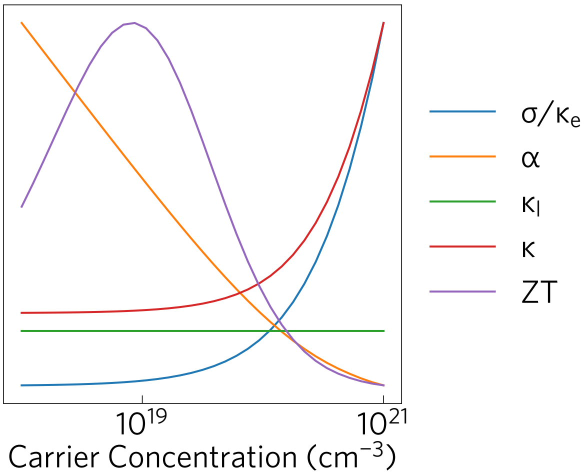

Figure 3.2: A depiction of the interrelated properties that make up ZT. High ZTs require high electrical conductivity, σ and Seebeck coefficient, α, but low thermal conductivity, κ.

pressed by the Wiedemann–Franz law:[36]

$$\kappa_e = L\sigma T \tag{3.5}$$

where L is the Lorenz number. Thermoelectrics need to be conductive, so reducing electron transport to lower the thermal conductivity is not a desirable solution. This lead to the phonon-glass electron-crystal (PGEC) concept,[37] where electrons are allowed to be conducted rapidly like in a crystal, while phonons are forced to move slowly and be scattered like in a glass to minimise thermal conductivity while maintaining an acceptable electrical conductivity. PGEC materials can be made by controlling the structure of materials at the atomic scale,[38] or at the macro scale.[39] An example of the former is adding disorder to the material, to prevent phonons transferring down long lines of atoms which vibrate at similar frequencies, and therefore transmit phonons efficiently. Disorder, either by changing the locations of extant atoms or extrinsically doping a material, can break up these paths, scattering phonons and decreasing the lattice thermal conductivity. Another option is adding rattlers: large, weakly bound atoms or ions which can vibrate relatively freely, efficiently scattering the phonons.

Temperature is another complicating factor. In Equation (3.1) one can see Seebeck coefficient increases with temperature. Furthermore, as temperature rises, increased thermal motion of the atoms increases the rate at which they scatter phonons, lowering lattice thermal conductivity. Combined with the temperature factor in Equation (3.2), ZT is much much higher at high temperatures. This means an important limiting factor for thermoelectrics is often their thermal stability, as a maximum ZT is often not reached before they decompose. It also makes room temperature thermoelectrics very inefficient. If efficient room temperature thermoelectrics were realised, the commercial uses of thermoelectric energy harvesting could be expanded from energy recycling in relatively niche, albeit efficient, high temperature industrial settings to much lower temperatures both industrially and domestically, enabling a vastly increased scope for their deployment. On the other hand, increasing temperature smears out the Fermi–Dirac distribution, the energies which fermions such as electrons occupy, to higher energies. If it excites the minor charge carriers (i.e. holes in an n-type material) across the band gap, this results in ambipolar doping. While this causes a large increase in the electrical conductivity, it can wipe out the Seebeck coefficient as both the electrons and holes move in the same direction, cancelling each other out, resulting in a low ZT at high temperatures and low carrier concentrations. Therefore, high temperature thermoelectrics need larger band gaps than low temperature thermoelectrics, but this makes it more difficult to dope it heavily enough to maximise ZT. The band gap also affects the colour of the material, which while insignificant to the efficiency, may affect where it may be used: a transparent thermoelectric could be particularly versatile.

Thermoelectric Materials

The most efficient thermoelectrics today have ZTs greater than 2, perhaps some of the most famous being PbTe[40–44] and Bi_2Te_3,[45] with ZTs of 2.2 and 2.0 respectively. Unfortunately such materials are inappropriate for wide-scale deployment due to their rare and toxic elements, so new materials are required. A more earth-abundant alternative is SnSe, which has reached ZTs up to 2.6,[46] however it faces difficulties in synthesising it at scale due to tight growth requirements and poor packing ability of the powder, meaning single crystals are necessary. These are particularly hard to grow with respect to doping conditions,[47] a major barrier for thermoelectrics, which require high doping concentrations.[48]

Oxide thermoelectrics are an appealing class to study, as they are heavily studied for other reasons, such as as transparent conductors, of which CdO was the first to be studied in 1907,[49,50] coincidentally while studying the thermopower (Seebeck coefficient). Transparent conducting oxides (TCOs) in particular have a wide array of high-profile uses, from solar panels and device screens to insulating glass coatings,[51] so the wide-scale production knowledge and supply chains already exist. They have a number of desirable characteristics for thermoelectrics. They have a high chemical and thermal stability, for example ZnO has high melting and decomposition temperatures of 2,250 K and 2,247 K respectively;[52] CdO melts at 1,700 K and In_2O_3 melts at 2,185 K,[53] enabling such materials to access the most concentrated energy sources and achieve higher ZTs. While there are some TCOs with toxic metals such as CdO, this can be mitigated due to the strong chemical bonds these compounds leading to a low metal loss factor during fires,[54,55] although that does not speak to the safety in their pre-device lifetime, including mining and processing. As their name suggests, they are highly conductive, with dispersive conduction bands which can be related to linked metal oxide polyhedra.[56] Unfortunately, this is also coupled with low Seebeck coefficients and high lattice thermal conductivities,[57] but there are methods that can improve each of these.

As we have seen, the Seebeck coefficient is dependent on the charge carrier effective mass (Equation (3.1)), leading to the strategy of finding relatively flat-band systems, but this would come at the expense of the electrical conductivity. A more complex picture was constructed by Gibbs *et al.*,[58] who defined the effective mass in two separate ways. The first was the conductivity effective mass, m_c^*, which is defined by feeding the conductivity back into Equation (3.4) to get the effective mass, keeping the relaxation time constant under the constant relaxation time approximation (CRTA). This is an effective measure of the average inertial effective mass, i.e. the most literal meaning of the term, but does not account for the effects of multiple bands at the band edge, which can have a large effect on the Seebeck coefficient. An alternative definition of the Seebeck coefficient is:

$$\alpha = \frac{\sum_i \sigma_i \alpha_i}{\sum_i \sigma_i} \quad \text{where} \quad \alpha_i = \frac{\int g_i(E)E(E-E_F)\frac{\partial f}{\partial E}dE}{eT\int g_i(E)E\frac{\partial f}{\partial E}dE}, \tag{3.6}$$

where i is the band index, g is the electronic density of states (DoS) and f is the Fermi–Dirac distribution.[59] This equation shows the the Seebeck coefficient is weighted by the density of states and the Fermi–Dirac distribution derivative with respect to energy of the system, meaning that a large density of states, which could be supplied by higher band degeneracy at the band edge. The shape of the bands is also consequential, which is where the second effective mass of Gibbs et al.[58] comes in, the Seebeck effective mass m_S^*. This is the effective mass that would get the calculated Seebeck coefficient, if all the bands were a single band, which now takes into account band degeneracy and other factors. From these effective masses, they calculated the Fermi surface complexity factor:

$$N_v^* K^* = \left(\frac{m_S^*}{m_c^*}\right)^{\frac{3}{2}}, \tag{3.7}$$

where N_v^* is the effective valley degeneracy and K^* is the effective anisotropy factor. N_v^* is the number of degenerate states that would exist if there were N_v^* independent valleys, but it also accounts for non-degenerate and non-identical states through:

$$m_S^* = N_v^{*\frac{2}{3}} m_b^*, \tag{3.8}$$

where m_b^* is a conceptual single valley effective mass, which is not well defined. This accounts for band degeneracy at the same k-point, but it is also important to consider the degeneracy of off-Γ band extrema. The Γ point, at the centre of the Brillouin zone, is not affected by any symmetry operations, but other points will be, with the maximum degeneracy occurring off of high-symmetry paths in highly symmetric structures. K^* describes the deviation from spherical band edges, for example ellipsoidal band edges would have an anisotropy parameter, K, of $\frac{m_\parallel^*}{m_\perp^*}$, and non-ellipsoidal band edges are ascribed a K^* as:

$$K^* = \left(\frac{m_b^*}{m_c^*}\right)^{\frac{3}{2}} \tag{3.9}$$

This analysis has been used, for example, on CdTe, which has a singly-degenerate, highly disperse CBM, and therefore and $N_v^* K^*$ of 1;[58] AlAs, which has a single disperse CBM at the X point, which in that structure has threefold degeneracy, and a $N_v^* K^*$ of 3.5;[58] and $\mathrm{Mg_3(Sb, Bi)_2}$, where multiple off-high-symmetry extrema and a threefold-degenerate area of flat dispersion combine to reach peaks of $N_v^* K^*$ of up to 20, corresponding to peaks in the power factors.[60] Gibbs et al.[58] also examined the lead oxychalcogenides PbS, PbSe and PbTe. PbTe in particular is famous as a high-efficiency thermoelectric, reaching a p-type ZT of 2.2 at 800–915 K,[40,41] and in the study of Gibbs et al.[58] it was shown that at 600 K with an N_v^* of 12, the $N_v^* K^*$ was 50, consistent with the long, anisotropic hole pockets in the valence band.

PbTe also has excellent thermal conduction characteristics. Skelton et al.[61] studied the lead chalcogenides under the quasi-harmonic approximation (QHA),[62] allowing temperature-dependent thermal transport to be calculated up to 600 K, above which anharmonic effects become too strong and the QHA becomes less accurate. They found that the increasing the temperature causes the already low lattice thermal conductivity of 1.91 $\mathrm{W\,m^{-1}\,K^{-1}}$ at 300 K to decrease further, partly due to a lowering of the frequency of the modes, known as softening. This approximation proved accurate at low temperatures (100–300 K), but underestimated experimental lattice thermal conductivities by 2–3 times at 600 K. The results do not account for scattering mechanisms such as defects and grain boundaries, and do not recreate experimentally observed effects in PbTe such as avoided crossings in the bands, which is attributed to anharmonic effects.[63] All of these effects would be expected to reduce the lattice thermal conductivity further, so other unaccounted for effects such as anharmonicity beyond the QHA approximation must have significant effects, although this does suggest some fortuitous cancellation of errors within QHA.

Anharmonic effects are an effective way of decreasing the lattice thermal conductivity in other materials too, prime examples of which are in cage structures such as skutterudites and clathrates. These are both cage-like structures with guest atoms: clathrates typically have a polyhedral cage structure made of group 14 atoms or water ice or transition metals and pnictogens and the filler atoms is normally from groups 1, 2, 16 or 17; whereas skutterudites have the formula $\mathrm{EP}_y\mathrm{T}_4\mathrm{X}_{12}$, where EP is an electropositive filler element such as a rare earth metal (y can be 0), T is a transition metal and X is typically a pnictogen. They typify the PGEC concept as the cage acts as a network through which charge carriers can conduct, and the weakly-bound guest can "rattle", effectively scattering phonons and therefore disrupting the thermal conductivity.[64] Computationally, this rattling exhibits itself as a highly localised phonon density of states and flat bands in the phonon band structure. They also cause avoided crossings of the bands, which indicate high scattering rates, and can suppress the height (in energy space) and therefore gradient/ group velocity of the acoustic phonons, which often carry the majority of the thermal conductivity due to a combination of high group velocity, low scattering rates and high occupation.[57] In the review of inorganic clathrates by Dolyniuk et al.,[64] almost all the clathrates studied had low lattice thermal conductivities, below $6\,\mathrm{W\,m^{-1}\,K^{-1}}$, with the exception of Na-Si systems, which have higher electrical conductivities, lower Seebeck coefficients and higher electronic contributions to the thermal conductivity than other clathrates — the lattice thermal conductivity accounts for 70 % of the total thermal conductivity for 75 % of all the clathrates studied. Heavier guest atoms result in lower lattice thermal conductivities, showing the importance of rattling, but heavier frameworks also play a significant role in reducing the thermal conductivity, that is to say the thermal conductivity follows the trend Sn $<$ Ge $<$ Si in this study. This results in thermopower being the major deciding factor in clathrate thermoelectrics, whereas in general lattice thermal conductivity is also a significant distinguishing factor. Another distinction compared to thermoelectrics as a whole is that there are more n-type clathrate thermoelectrics published than p-type ones, but like other thermoelectrics, the n-type materials still have higher electrical conductivities and lower Seebeck coefficients than the p-type ones. Clathrates are required to be electron-balanced in order to exhibit semiconducting behaviour, as their otherwise metallic behaviour results in a low Seebeck coefficient and high electronic contribution to the thermal conductivity, and this can be engineered by creating vacancies in the structure or substituting atoms in. Overall, the highest ZT materials had Seebeck coefficients above $200\,\mathrm{\mu V\,K^{-1}}$, conductivities of 10–$1{,}000\,\mathrm{S\,cm^{-1}}$ and thermal conductivities below $2\,\mathrm{W\,m^{-1}\,K^{-1}}$, leading to a maximum ZT of 0.7 at 300 K for some Sn-based clathrates.

Skutterudites and clathrates have a range of methods with which to optimise them, such as those outlined in a review of $\mathrm{CoSb_3}$-based skutterudites by Liu et al.[65] Like other materials, substituting atoms to create a solid solution can cause a large reduction in the lattice thermal conductivity, by a factor of at least 2 in the cases reviewed. Large size differences in particular increased the incidence of point defects, which can cause strong phonon scattering. Such substitutions can also improve electrical properties, for example doping Te on the Sb site increases the conductivity as well as decreasing the thermal conductivity, resulting in a ZT of 0.93 at 800 K.[66] Additionally doping with Ge on the same site charge-compensates for the Te, increasing the solubility of the Te and further reducing the lattice thermal conductivity, reaching a ZT of 1.1 at 800 K.[67] Adding filler atoms can further enhance the ZT, for example in $Dy_{0.4}Co_{3.2}Ni_{0.8}Sb_{12}$, which reached a ZT of 1.4 at 773 K,[68] and adding multiple filling atoms can improve it further, to 1.7 at 850 K in $Ba_{0.08}La_{0.05}Yb_{0.04}Co_4Sb_{12}$.[69] High pressure torsion, which causes plastic deformation via an increased number of defects, has been used to reach a ZT of 1.9 at 835 K in $Sr_{0.09}Ba_{0.11}Yb_{0.05}Co_4Sb_{12}$, however after heating during the measurement of ZT this reduced to 1.8.[70]

Adding deformations is a widely used method to enhance thermoelectric performance, outside of skutterudites as well as within. Nanostructuring is method to reduce the thermal conductivity of materials through introducing boundaries on the nanoscale, with mean free paths shorter than those of phonons and longer than those of charge carriers, in order to get a net increase in ZT. This can take many forms, from plastic deformation similar to that mentioned above, inclusions of secondary phases and superlattices to creating nanoscale structures such as nanowires and quantum dots.[71] Superlattices, nanowires and quantum dots require fabrication that can currently only be done on a small scale, such as atomic layer deposition (ALD), so methods of bulk nanostructuring are required for widespread use. As an example, one method is doping, which at small scales can be referred to as nanocompositing. $Si_{80}Ge_{20}$ is one such nanocomposite, and has been produced with grain sizes of 10–20 nm, a length shorter than virtually all phonon mean free paths in bulk silicon at 300 K. While we can simulate the scattering of phonons at these grain boundaries by introducing a scattering rate related to the grain size ($\frac{v_g}{L}$ where v_g is the group velocity and L is the length of the grain or distance between impurities, henceforth referred to as the scattering distance), this only accounts for thermal boundary scattering, but due to the wave nature of phonons there will also be scattering of phonons of a similar wavelength to the scattering distance. Therefore, hierarchical structures are required to minimise lattice thermal conductivity, to scatter phonons of a range of wavelengths more effectively, as has been done in PbTe to get a ZT of 2.2 at 915 K. They combine the atomic-scale, through a solid solution with PbSe; nanoscale precipitates of SrTe and the resulting strain from lattice mismatch and mesoscale grain structure from spark plasma sintering.[41] They also propose that an interfacial charge preferentially scatters electrons over holes, reducing the negative effects of ambipolar doping at high temperatures in this p-type material, a phenomenon that has also been observed in $(\mathrm{Bi,Sb})_2\mathrm{Te}_3$.[72] The phonon scattering processes are still not well understood, but previous work using the methods in this thesis have predicted thermal conductivities within a factor of two from experiment.[57] Electronic scattering is another factor, although unlike phonons we seek to avoid it. The difficulty with electrons, is the Boltzmann equation treats them as particles, but their de Broglie wavelength, at least in $\mathrm{Si}_{80}\mathrm{Ge}_{20}$ is around 5–10 nm, so if the nanostructuring is at this scale, the Boltzmann transport equation may no longer be valid. In this thesis, we use the same scattering rate as for phonons, $\frac{v_g}{L}$, and limit the nanostructuring to 20 nm.

Returning to oxides, their study as thermoelectrics began in earnest in 1997 when Terasaki et al.[73] measured a large Seebeck coefficient in p-type $\mathrm{NaCo_2O_4}$ of $100\,\mu\mathrm{V\,K^{-1}}$, approximately 10x that of other candidate high-temperature superconductors, which it was initially studied for. Later work by Ma et al.[74] would show a high density of states at the valence band edge, along with a lighter band approximately 0.1 eV below, which could be accessible and account for its relatively high Seebeck despite its high conductivity of 5×10^4 S cm^{-1}. Later studies, however, have failed to achieve simultaneous high conductivity and Seebeck,[75,76] and even when prepared with a complex grain structure with grain sizes of down to 1 µm, resulting in a thermal conductivity below 1 W m^{-1} K^{-1}, ZT has not exceeded 0.05.[77] Related compounds Na_xCoO_2 and $Bi_2Sr_2Co_2O_y$ have reached ZTs of 1 at 800 K[78] and 1.1 at 973 K[79] respectively, the latter partly due to the reduced lattice thermal conductivity from the whisker-like structure, of width 10–50 µm. Na_xCoO_2 in particular has been studied as a Na intercalation compound for batteries, and the mobile Na that are necessary for that[80] have been attributed for the low lattice thermal conductivity below 1 W m^{-1} K^{-1};[81] but they can also form insulating phases on reacting with water or CO_2 in the air, to the detriment of the thermoelectric performance.[82] Furthermore, the highly anisotropic nature of the material means bulk samples have only reached ZTs of 0.7–0.8 .[82] Computationally, a p-type ZT of 2.10 and 1.92 have been reported for the mixed-anion oxypnictides, LaZnOP and LaZnOAs at 1,000 K,[83] although further work found that they could not be doped to the required level and this has not been realised experimentally.

As is often the case in thermoelectrics, n-type oxide thermoelectrics lag behind their p-type counterparts. The dominant earth-abundant n-type thermoelectric oxides are the perovskite-structured $SrTiO_3$ and $CaMnO_3$. Doped with La and Nb[84] or Dy,[85] $SrTiO_3$ can reach ZTs of over 0.4 at around 1,000 K. Combining La and Nb doping to optimise the carrier concentration with measures to decrease the thermal conductivity, including the dopants themselves, but also TiO_2 inclusions, superstructures thought to arise from variations in the lattice resulting from codoping, and the presence of micro- and nano-sized grains, Wang et al.[86] reached a ZT of 0.65 at 1,100 K. Cation substitution has also been attempted to form $La_{0.5}Na_{0.5}TiO_3$, which resulted in an 80 % reduction in lattice thermal conductivity, reaching a ZT of 0.2 at 1,000 K.[87] Meanwhile, $CaMnO_3$ has stalled at a ZT of 0.2 at 1,000 K when doped with Dy or Yb,[88] where they also parametrise the transport properties in terms of dopant concentration to conclude such efforts are unlikely to yield a ZT in excess of 1. Nevertheless, this does not account for the various thermal engineering techniques employed in $SrTiO_3$, so further improvement may still be possible. $CaMnO_3$ has been computationally predicted to reach ZTs up to 1.37 at 100 K,[89] although they use the GGA level of density functional theory, which as we will discuss later is not appropriate for electronic transport calculations. In this case, it leads to a massively underestimated band gap of 0.7 eV, as opposed to the experimental value of 3.07 eV,[90] which leads to spurious decreasing of the Seebeck coefficient with temperature, consistent with ambipolar doping effects found in small band gap materials, and inconsistent with experimental data. Other work which used a higher level of theory, known as GGA+U, where U is a repulsive interaction that reduces unrealistic delocalisation of electrons in GGA, predicts a band gap of 1.42 eV and a much lower ZT of 0.03 at 1,000 K, without the defect effects that have allowed experimental data to exceed this value.[90]

The most-studied TCO thermoelectrics are ZnO and In_2O_3. Along with other TCOs, their metal-oxygen network provides a conductive route for electrons, but this is not conducive to a high Seebeck coefficient, and efforts tend to focus on reducing the lattice thermal conductivity. The highest ZT for ZnO is 0.3 at 1,273 K for Al doped ZnO (AZO),[91,92] which did not significantly decrease the lattice thermal conductivity below the relatively high value of $5\,\mathrm{W\,m^{-1}\,K^{-1}}$. The highest singly-doped TCO ZT is 0.45 at 1,273 K for Ge doped In_2O_3,[93] which unlike AZO does not experience substitution of the Ge onto the In site, but rather forms inclusions of $In_2Ge_2O_7$. This not only causes a threefold increase in conductivity, but a fivefold decrease in thermal conductivity to $0.6\,\mathrm{W\,m^{-1}\,K^{-1}}$. Still higher

ZTs are achieved by dual doping: Al and Ga doped ZnO reaches a ZT of 0.65 at 1,247 K.[94] Like other dually-doped materials, one dopant, the Ga in this case, serves to enhance the solubility of the other, in this case Al. Thermal conductivity decreased from $8\,\mathrm{W\,m^{-1}\,K^{-1}}$ in AZO to $7\,\mathrm{W\,m^{-1}\,K^{-1}}$ with 1 % Ga to $5\,\mathrm{W\,m^{-1}\,K^{-1}}$ with 2 %, above which excess Ga forms a significant amount of a secondary phase and the thermal conductivity drops to $3\,\mathrm{W\,m^{-1}\,K^{-1}}$ (a small amount of impurity phase forms in all the Ga doped samples). A similar pattern was observed with the electrical conductivity, except the samples with more than 3 % Ga had a drop of four orders of magnitude, making them unsuitable thermoelectrics, but the researchers note that at lower Ga concentrations the increased Al solubility mitigates the reduced electrical conductivity that the Ga would otherwise have caused. All the Ga-doped samples had an increase in the Seebeck coefficient, but it was the $Zn_{0.96}Al_{0.02}Ga_{0.02}O$ which had the largest Seebeck (besides the insulating phases) of $250\,\mathrm{\mu V\,K^{-1}}$ and maximised the ZT. In this work, we will not be able to simulate complex effects such as dual doping and complex hierarchical structure techniques due to limited computational power, however we will be able to observe in granular detail the intricacies of electronic and phononic transport, providing a means to explore how these materials might be enhanced and compare with each other. Thus, despite the discrepancies that can sometimes arise between theory and experiment, we hope this work can advance the field synergistically with the experimental results described above.

Part II

Theory

4 Computational Theory

Quantum Chemistry

Much of this section is based on Computational Materials Science by June Gunn Lee.[95] The basis of density functional theory (DFT) is the time independent Schrödinger equation:[96]

$$\hat{\mathbf{H}}\Psi(x_i, y_i, z_i) = E\Psi(x_i, y_i, z_i), \tag{4.1}$$

where $\hat{\mathbf{H}}$ is the Hamiltonian (total energy) operator, Ψ is the wavefunction and E is energy for particles i at positions (x_i, y_i, z_i). This is a highly complex equation, exactly solvable only for very simple systems such as the hydrogen atom (even the hydride ion is too complex), and so not ideal for extended systems such as semiconductors, which this project is interested in. Because of this, several approximations are required to make it tractable. The first, as has been implied, is that time is neglected. This limits calculations to the ground state, as any other state is only transient, but this is perfectly acceptable for these purposes. Now we consider the energy of the system:

$$E = E_I^{\text{kin}} + E_i^{\text{kin}} + E_{IJ} + E_{Ii} + E_{ij}, \tag{4.2}$$

where E^{kin} is the kinetic energy and E_{xy} is the potential energy energy between nuclei I, J and electrons i, j:

$$E_i^{\text{kin}} = -\frac{1}{2}\sum_i^n \nabla_i^2 \quad \text{where} \quad \nabla^2 = \frac{\partial^2}{\partial \mathbf{x}^2} + \frac{\partial^2}{\partial \mathbf{y}^2} + \frac{\partial^2}{\partial \mathbf{z}^2}, \tag{4.3}$$

$$E_{Ii} = -\sum_{I}^{N}\sum_{i}^{n}\frac{Z_I}{|\mathbf{r}_{Ii}|} \quad \text{and} \quad E_{ij} = \frac{1}{2}\sum_{i\neq j}^{n}\frac{1}{\mathbf{r}_{ij}}, \tag{4.4}$$

in atomic units, where N and n are the numbers of ions and electrons, respectively, ∇^2 is known as the Laplacian operator and $\mathbf{r}$ is the distance between two particles. The second and probably most famous approximation is the Born–Oppenheimer approximation,[97] which acknowledges that the atomic nuclei are so large compared to the electrons, that their motion is negligible on the electron's timescale, so the nuclear kinetic energy, E_I^{kin} can be omitted and the nuclear interaction energy, E_{IJ}, can be combined with the nucleus–electron interaction energy, E_{Ii}. Still, much complexity comes from the remaining interactions, so the Hartree method[98] made the electrons independent, interacting only with an attractive external potential caused by the atomic nuclei, resulting in an external energy E_{ext}, and a repulsive mean field caused by all the electrons, the Hartree potential, causing the Hartree energy, E_{H}:

$$E = E^{\text{kin}} + \overbrace{E_{\text{ext}}}^{E_{Ii}+E_{IJ}} + \overbrace{E_{\text{H}}}^{E_{ij}}. \tag{4.5}$$

Now, the energy of all the electrons is simply the sum of the energies of each electron, or alternatively the total wavefunction is the product of the individual ones, but this is a gross oversimplification of the interactions of the electrons.

One of the oversimplifications of the Hartree method is the omission of the exchange energy. The total wavefunction of a system of fermions (a class of particles with half integer spins of which electrons are part) is always antisymmetric, that is to say that if any two particles swap, the wavefunction changes sign. The Hartree–Fock (HF) method[99] accounts for this by treating the wavefunctions as a Slater determinant.[100] Matrix determinants change sign if you swap any two columns or rows (particles) around, making this a suitable representation of a wavefunction. Furthermore, if any two rows or columns of a matrix are the same, the determinant is 0, ensuring orthogonality of the eigenstates. This describes the Pauli exclusion principle,[101] whereby two particles cannot have the same quantum numbers (or else they would have no wavefunction), demonstrating the applicability of the matrices to this problem. Treating the wavefunction in this way gives a new form for the energy:

$$E = E_{\mathrm{kin}} + E_{\mathrm{ext}} + E_{\mathrm{H}} + E_{\mathrm{x}}, \tag{4.6}$$

where the new term E_{x} is the exchange energy. Due to the Pauli exclusion principle, electrons of the same spin tend to avoid one another, creating areas of depleted electron density near electrons called exchange holes. The exchange energy corresponds to a restoring force towards that hole, and therefore lowers the overall energy. The other improvement of HF is the utilisation of the variational principle, which gives an iterative solution to a problem where both the wavefunction and Hamiltonian depend on the electron density. This states that the ground state is the lowest energy state of a system, and therefore by varying the wavefunctions in order to minimise the energy of the system, the ground state can be approached. In HF and subsequent computational methods, a self-consistent method is used, where trial wavefunctions are used to calculate energies for the electrons of the system, and use the resulting electron densities to generate a new set of wavefunctions. This process is repeated until the input and output energies are the same within some tolerance.

DFT

DFT itself started from the Hohenberg–Kohn theorems.[102] The first is that there is a unique ground state energy determined solely by the ground-state electron density. An external energy is used analogous to the E_{ext} used previously, except now it is a functional of the electron density, not electron positions. The second theorem is that the variational principle is applied to the electron density, and used to find the minimum energy — the ground state. This leaves us with the following equation:

$$E[\rho(\mathbf{r})] = F[\rho(\mathbf{r})] + E_{\mathrm{ext}}[\rho(\mathbf{r})] \geqslant E_{\mathrm{gs}}, \tag{4.7}$$

where $\rho(\mathbf{r})$ is the electron density at a given radius, $\mathbf{r}$, E_{ext} and E_{gs} are the external energy functional and ground state energy and F is the energy functional of the remaining interactions, including the electron kinetic energies, Hartree energy etc. whose form remains to be found.

The implementation of this came with the Kohn–Sham approach,[103] which introduced the Kohn-Sham auxiliary system,[104] which considers non-interacting electrons and an interacting electron density. This splits F into more calculable quantities:

$$F[\rho(\mathbf{r})] = E_{\mathrm{kin}}^{\mathrm{non}} + E_{\mathrm{H}} + E_{\mathrm{xc}}. \tag{4.8}$$

Where $E_{\mathrm{kin}}^{\mathrm{non}}$ is the kinetic energy of the non-interacting electrons, whose form is known. The interacting component, $E_{\mathrm{kin}}^{\mathrm{int}}$, which is relatively small but complex, has been folded into the exchange–correlation energy, E_{xc}, which replaces the exchange energy in HF. This accounts for both the exchange energy and the correlation energy, the latter of which is very similar to the exchange energy in that it is due to the restoring force towards an area of decreased electron density round electrons, but this decreased electron density is caused by the Coulombic repulsion between electrons rather than the Pauli exclusion principle. The exchange–correlation energy is the remaining part to be approximated — the exact exchange energy is not used in DFT.

The exchange–correlation functionals used in DFT, normally referred to simply as the functionals, come in four main flavours based primarily on how they treat the electron density. The first is the local density approximation (LDA), which approximates the exchange–correlation energy based solely on the electron density at that point.

$$E_{xc}^{\mathrm{LDA}}[\rho(\mathbf{r})] = \int \rho(\mathbf{r}) E_{xc}^{\mathrm{UEG}} d\mathbf{r}, \tag{4.9}$$

where UEG is the uniform electron gas. This can work fine for some materials, but is inaccurate for materials with rapidly changing electron densities. It tends to overestimate the exchange energy and underestimate the correlation energy, leading to a cancellation of errors, but this can break down in highly correlated materials. While it is straightforward to discount an electron interacting with itself in separate-electron approaches, by specifying directly in summations or by using the properties of matrix determinants to enforce the Pauli exclusion principle, this is not the case for the electron density. This leads to what is known as the self interaction error, where the correlation energy is underestimated, particularly in orbitals with high electron density.

The more refined version than this is the generalised gradient approximation (GGA), which contains not only the electron density but its differential (gradient), which recreates the real density of more variable-density systems more accurately. Practically, this is implemented as a modification of the LDA:

$$E_{xc}^{\mathrm{GGA}}[\rho(\mathbf{r}), s] = \int \rho(\mathbf{r}) E_{xc}^{\mathrm{LDA}}[\rho(\mathbf{r})] F(s) d\mathbf{r}, \tag{4.10}$$

where $F(s)$ is the enhancement factor, dependent on the GGA functional, and

$$s = C \frac{|\nabla \rho(\mathbf{r})|}{\rho^{\frac{4}{3}}(\mathbf{r})}, \tag{4.11}$$

where C is a constant. The popular Perdew–Burke–Ernzerhof (PBE) functional[105] is one such functional. Whereas LDA underestimates lattice constants by 3–4 %,[106] PBE tends to get structural properties to within 3 %, with a slight tendency to underbind.[95,107–109] Perdew et al.[110] noted that while the gradient term in GGA tended to improve energy predictions, it worsened lattice constant predictions in solids, and so modified

PBE to make a special form for solids, PBEsol, which obtains more accurate lattice parameters than either LDA or PBE by restoring some LDA-like character to PBE. We use PBEsol for calculating the lattice parameters and lattice dynamics in this thesis, the latter of which it has also been shown to be appropriate for,[111] due to its accuracy and computational efficiency, which are especially important when doing large numbers (tens or hundreds of thousands) of phonon calculations.

In both LDA and GGA, band gaps are underestimated by around 50 %, although the range on this value is rather large and can extend to over 100 % in some small band gap systems, i.e. it can turn semiconductors into metals. This can be attributed in part to the definition of the band gap: the correct definition is the (positive) energy of adding an electron to the conduction band minimum plus the (negative) energy of removing an electron from the valence band maximum, but using the Kohn–Sham non-interacting electrons this becomes the energy of the conduction band minimum minus the energy of the valence band maximum, and doesn't consider the change in occupation As an occupied level, such as the valence band maximum, has a higher energy and an unoccupied level, such as the conduction band minimum, has a lower energy, this narrows the band gap. There are several methods that seek to correct this. Meta-GGA, such as the Tran–Blaha (TB, or modified Becke-Johnson, mBJ) functional,[112,113] includes the second derivative of the electron density, which recreates the band gap much more accurately, although underestimates the band widths,[114] making it unsuitable for electronic transport calculations. Here we use a hybrid functional for electronic properties, which replace a certain proportion of the approximate GGA exchange energy with the exact HF exchange energy:

$$E_{xc}^{\text{hybrid}} = E_{xc}^{\text{GGA}} + \alpha \left(E_x^{\text{HF}} - E_x^{\text{GGA}} \right), \tag{4.12}$$

where α is the proportion of exact HF exchange. As HF overestimates the band gap, this cancels out the error in GGA.

Two of the dominant hybrid functionals are PBE0, which is PBE with 25 % HF exchange, and tends to work well for wide bandgap materials; and the Heyd–Scuseria–Ernzerhof (HSE06) functional,[115] which is PBE with 25 % HF exchange at short range that is screened out at longer range so it becomes pure GGA, which works well for smaller bandgap systems, and is used for all the materials in this project. These have been shown to be very accurate,[116–131] but at significant (≈10x GGA) computational expense, so are only used for the electronic calculations, where they are required.

Part III

Methodology

5 VASP

The main formulation of DFT has now been outlined, but there remain several methods to improve efficiency. Here those methods pertaining to the Vienna *Ab-initio* Simulation Package (VASP),[132–135] the primary code used in this project, are outlined.

Pseudopotentials

The first concerns the individual atoms, which are composed of a high energy nucleus and its accompanying electrons, many of which are core electrons which do not participate in bonding. Instead of simulating them all, a "frozen core" is used, where the nucleus and all the core electrons are treated as a single entity, which greatly simplifies the simulation, and parametrises any relativistic effects from fast-moving electrons in the inner core of heavy elements. The valence electrons can also be simplified in a process called pseudisation. This involves removing any nodes in the wavefunctions to make a smooth function, with a simple mathematical form which can easily be simulated. The particular type of pseudopotential used in this project is the projector augmented-wave (PAW) method.[136,137] This starts with a wavefunction which consists of an addition of a radial function to simulate the core and a plane-wave function to simulate some of the non-core parts of the valence electrons; and from this wavefunction pseudopotentials are generated. These PAW potentials can represent the valence electron density as accurately as traditional potentials such as the norm-conserving or ultrasoft pseudopotentials, normally at a cheaper cost. They are then written into the potentials card (`POTCAR`) file, from which VASP can recreate the original wavefunctions.

Bloch's Theorem

As well as simplifying the wavefunctions, the number of atoms simulated can be decreased in a periodic solid by subjecting the smallest repeating unit, or unit cell, to periodic boundary conditions, whereby each atom responds only to atoms within that cell and the periodic images. This can be represented by a periodic potential with a period the length of the lattice:

$$u(\mathbf{r}) = u(\mathbf{r} + \mathbf{R}) \tag{5.1}$$

where u is the potential at position $\mathbf{r}$ and $\mathbf{R}$ is one lattice vector. Electrons are also periodic, and free electrons can be described as plane waves. To put this into a solid, the Bloch theorem states that the valence electrons in a solid are simply free electrons modulated by a periodic potential from the lattice:

$$\psi_{\mathbf{k}}(\mathbf{r}) = u_{\mathbf{k}}(\mathbf{r}) e^{i\mathbf{kr}} \tag{5.2}$$

where ψ is the electron wavefunction and $\mathbf{k}$ is a wavevector. Now, if we translate by some amount $\mathbf{r}_1$, we get the original plane wave modulated by a periodic function, and if $\mathbf{r}_1 = \mathbf{R}$, as $e^{i\mathbf{kR}} = 1$, we recover the original function:

$$\begin{aligned} \psi_{\mathbf{k}}(\mathbf{r} + \mathbf{r}_1) &= u_{\mathbf{k}}(\mathbf{r} + \mathbf{r}_1) e^{i\mathbf{k}(\mathbf{r}+\mathbf{r}_1)} \\ \psi_{\mathbf{k}}(\mathbf{r} + \mathbf{R}) &= \psi_{\mathbf{k}}(\mathbf{r}) e^{i\mathbf{kR}} \\ &= \psi_{\mathbf{k}}(\mathbf{r}) \end{aligned} \tag{5.3}$$

Now there is a mathematical form in which a system can be simulated with the periodicity of the lattice and subject to periodic boundary conditions, so the entire material can be simulated in one unit cell, which is entered into the positions card (`POSCAR`) file, and outputted as the continuation card (`CONTCAR`) file.

k-points

We not only need to simulate the unit cell, but how it relates to the rest of the crystal. We can do that by examining the crystal in reciprocal space, often known as k-space, or momentum space. Like the periodic unit cell, k-space can be reduced down to a single “unit cell”, called the first Brillouin zone, often abbreviated to just the Brillouin zone or BZ, with later identical zones onioned around it.[138] When simulating a system, VASP switches between real space and k-space depending on which is more efficient for a particular calculation; and many of the quantities we show in this thesis are represented in k-space, including the electronic and phononic band structures and several of the thermal transport properties. Phononic properties are actually represented in q-space, which is identical except $q = 2\pi k$. Due to finite computational resources, we calculate properties only at specific points, known as k-points, often focusing on certain important high-symmetry points, for example the Γ point, at (0, 0, 0), is the perfectly in-phase point at which the band extrema are often found. Almost all calculations are calculated on a Γ-centred k-point mesh, which is an evenly spaced grid including the Γ point, and some additionally have other points, such as the high-symmetry paths in the electronic band structures. As k-points are in reciprocal space, larger cells require a less dense k-point grid (Figure 5.1(b)), but the value used is determined explicitly by convergence testing, checking the total energies outputted from VASP for a range of k-point meshes and selecting one sufficiently similar to previous values, in most cases here to a condition of $5\,\mathrm{meV\,atom^{-1}}$. These we specify in the k-points (`KPOINTS`) file. The k-point mesh selected is further simplified through symmetry, which allows the Brillouin zone to be reduced to the irreducible Brillouin zone (Figure 5.1(c)), and the k-points actually sampled are written into the irreducible Brillouin zone k-points (`IBZKPT`) file, which can also be used as the `KPOINTS` file.

Figure 5.1: A large (light) 2D unit cell and a small (dark) cell shown in regular space (a), when transformed into reciprocal space (b) invert the ratio of their sizes. This means that the light cell, while larger in regular space, requires only a 1×1 k-point grid, while the dark cell requires 2×2 (black dots). Symmetry reduces this to one and three k-points in the irreducible Brillouin zone (IBZ, blue, c) respectively.

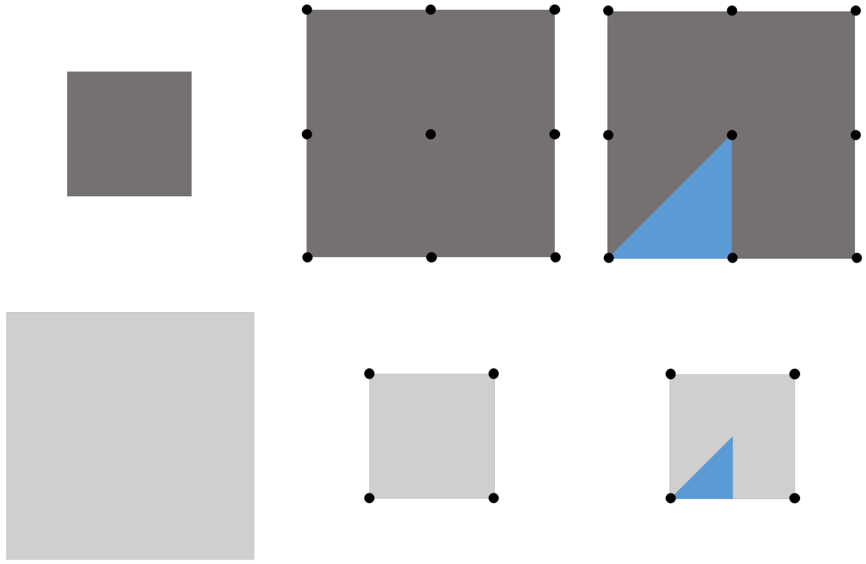

(a) Regular Space (b) Reciprocal Space (c) IBZ

Basis Sets

In order to run the simulation, the wavefunctions of the electrons need to be represented in some way in the simulation, which is done by a set of functions called a basis set. An obvious option would be a grid, not unlike the k-point grid, of Gaussians throughout the cell, or with functions centred on the atoms. Both of these, however, would produce an unphysical tendency for the ions to align to these functions due to a Pulay stress, which is caused by incomplete basis sets if Hellmann–Feynman forces are used[139] (Hellmann–Feynman forces are calculated classically on the electron density from Schrödinger's equation[140]). Instead, VASP uses a plane-wave basis set, which are agnostic to atom position and identity. A perfect plane wave basis set would be complete, so exert no Pulay stress, however an infinite number of plane waves cannot be simulated, so convergence testing is conducted on the energy cut-off (`ENCUT`, specified in the input card (`INCAR`) file) value, the maximum energy of the plane waves used, in the same way as it was with the k-point grid. Even in a sufficiently converged k-point mesh with a converged plane-wave energy cut-off, Pulay stress can still occur if the unit cell changes size sufficiently, so when doing a geometry relaxation the `ENCUT` value has been increased by 30 % to minimise that effect.

6 ELECTRONIC CALCULATIONS

Electronic Structures

In order to calculate the transport properties of the materials, we first calculate the electronic structures. These show the distribution of electron energy levels in k-space, as calculated by VASP, and are shown in two ways in this thesis. The first is the electronic band structure, on the left of Figure 6.1, which shows the valence band in blue and the conduction band in orange along a path between high-symmetry points in k-space, where key features like the conduction band minimum (CBM) and valence band maximum (VBM) tend to occur. The energy scale is given relative to the valence band maximum. This provides an effective visual method to assess a material, showing:

- If there is a bandgap, i.e. if the material is metallic or insulating.
- The ability to promote charge carriers across the bandgap. In thermoelectrics, a large bandgap will make it harder to dope to the optimal level, potentially limiting the ZT, but a small bandgap will allow *all* charge carriers to be thermally excited across the gap, resulting in ambipolar doping and a collapse of the Seebeck effect.
- An indication of the optical absorption frequencies, e.g. a material with a band gap of greater than 3.1 eV will likely be transparent.
- Whether or not the gap is direct, which affects the efficiency of the absorption as indirect bandgaps will require a phonon as well as a photon to excite a charge carrier.

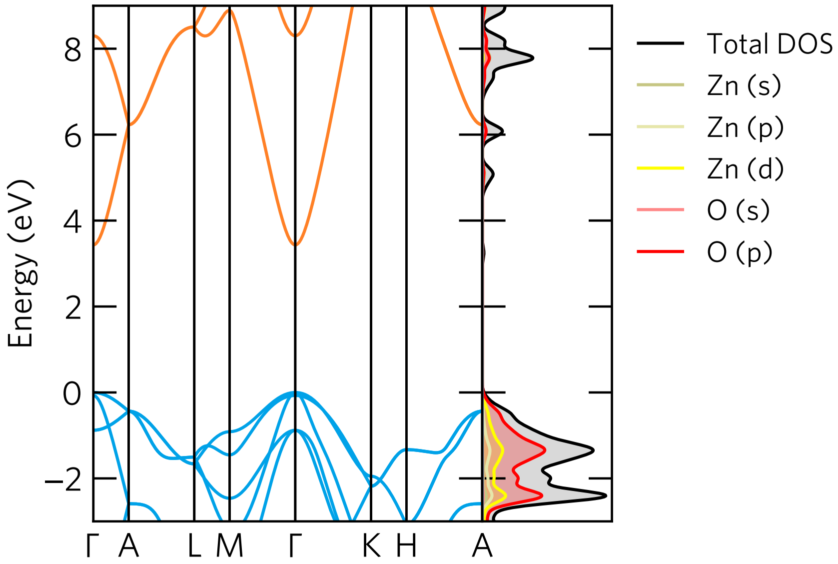

Figure 6.1: The electronic band structure and projected density of states (PDoS) of ZnO. The valence band is in blue and the conduction band is in orange. Plotted with sumo.[141]

- The mobility of charge carriers, which is proportional to the curvature of the bands. This is often quantified as the charge carrier effective mass:

$$\mu = \frac{e\tau}{m^*} \quad \text{where} \quad m^* = \frac{\hbar^2}{\frac{d^2E}{dk^2}}. \tag{6.1}$$

  If the mobility is high, the electrical conductivity will likely be high when doped.
- The Seebeck effect, which is higher if there are many states at the band edge, e.g if there are degenerate bands, flat bands or off-high-symmetry band edges.

The other version is the density of states (DoS), which calculates the energies on an even mesh in k-space, which is essential to getting a comprehensive view of the electronic transport, and is used as an input for the transport property codes. It is also necessary to plot a DoS graph, on the right of Figure 6.1, which can show the bandgap, but also the atomic makeup of the orbitals, which can give a clearer understanding of which atoms mediate charge transport.

In this thesis, we use the sumo package[141] to do this analysis, which plots the graphs, calculates the size and nature of the bandgaps and uses the parabolic band fitting method to calculate the effective masses. We use the Bradley–Cracknell formalism[142] for choosing the high-symmetry path, which hits the most important high-symmetry paths, but is not as comprehensive as for example SeeK-path.[143,144]

Boltzmann Transport Equation

The Boltzmann transport equation, described by Ludwig Boltzmann in 1872, statistically describes the movement of a fluid under some potential gradient, here the flow of electrons under electrical and temperature gradients, and phonons under a temperature gradient. For the electron transport, the conductivity tensor between two states, m and n, σ_{mn}, is given by:

$$\sigma_{mn}(i, \mathbf{k}) = e^2 \tau_{i,\mathbf{k}} v_m(i, \mathbf{k}) v_n(i, \mathbf{k}), \tag{6.2}$$

or in terms of energy:

$$\sigma_{mn}(\varepsilon) = \frac{1}{N} \sum_{i,\mathbf{k}} \frac{\sigma_{mn}(i, \mathbf{k}) \delta(\varepsilon - \varepsilon_{i,\mathbf{k}})}{d\varepsilon}, \tag{6.3}$$

where e is the charge of an electron, τ is the relaxation time, i is the band index, $\mathbf{k}$ is the wavevector, N is the number of k-points, v is the electron velocity and ε is the band energy. Note:

$$v = \frac{1}{\hbar} \frac{d\epsilon}{d\mathbf{k}}, \tag{6.4}$$

i.e. the electron velocity is proportional to the gradient of the bands in the electronic band structure. This is used to formulate the Onsager coefficients, named after Lars Onsager:[145]

$$L^{(a)}(\mu; T) = \int \sigma(\varepsilon)(\varepsilon - \mu)^a \left(-\frac{\partial f(\varepsilon; T)}{\partial \varepsilon} \right) d\varepsilon, \tag{6.5}$$

in atomic units where $L^{(a)}$ are the Onsager coefficients and f is the Fermi–Dirac distribution:[146,147]

$$f(\varepsilon; T) = \frac{1}{e^{\frac{\varepsilon - \mu}{k_B T}} + 1} \tag{6.6}$$

and μ is the chemical potential, in this case the Fermi Energy ε_F; and k_B is the Boltzmann constant. From the Onsager coefficients, we can calculate the transport properties, the conductivity:

$$\sigma = L^{(0)}, \tag{6.7}$$

Seebeck coefficient:

$$\alpha = \frac{L^{(1)}}{eTL^{(0)}} \tag{6.8}$$

and electronic contribution to the thermal conductivity:

$$\kappa_e = \frac{1}{e^2T}\left(\frac{{L^{(1)}}^2}{L^{(0)}} - L^{(2)}\right). \tag{6.9}$$

The fact that the scattering lifetimes are weighted by the derivative of the Fermi–Dirac distribution (i.e. a sharp function centred round the Fermi level) will become important later. With respect to the electronic thermal conductivity, this is sometimes approximated by the Wiedemann–Franz law,[36] either with a fixed Lorenz number (suitable for degenerate conductors/ metals) or a variable one,[148] but we use the explicit Onsager coefficient version in Equation (6.9).

Relaxation Time Approximations

The majority of the terms in the Equation (6.5) can be obtained from the electronic energies from a Density of States (DoS) in VASP, with the exception of the relaxation time, τ. The simplest method is the constant relaxation time approximation (CRTA), where the relaxation time is approximated to be constant, typically 1×10^{-14} s. This is the method implemented in the Boltzmann Transport Properties (BoltzTraP) code.[149] As computational power has increased, calculating some of the scattering rates explicitly has become tractable, so an update, BoltzTraP2 was released with a more accessible Python interface, and the ability to specify non-constant relaxation times, to act as a base on top of which other codes could be built.[150] In this thesis, we use the AMSET code,[151] which uses the momentum relaxation time approximation (MRTA) to calculate the scattering rates, which it feeds into BoltzTraP2 to calculate the transport properties. The MRTA assumes that electron lifetimes are scalar quantities, and that they are the same whichever direction the electron goes between two states. The specific flavour of MRTA used in AMSET is the self-energy relaxation time approximation (SERTA), which neglects back-scattering of the electron from the second state. Elastic scattering gives scattering rates, τ^{-1} as:

$$\tau^{-1} = \frac{2\pi}{\hbar} |g_{nm}(\mathbf{k}, \mathbf{q})|^2 \delta(\varepsilon_{n\mathbf{k}} - \varepsilon_{m\mathbf{k+q}}), \tag{6.10}$$

where the electron is scattered by a phonon of wavevector $\mathbf{q}$. Inelastic scattering is more complicated, including terms for the phonon energy $\hbar\omega_{\mathbf{q}}$ and Bose-Einstein occupation $b_{\mathbf{q}}$:

$$\begin{aligned} \tau^{-1} = {} & \frac{2\pi}{\hbar} |g_{nm}(\mathbf{k}, \mathbf{q})|^2 \\ & \times ((b_{\mathbf{q}} + 1 - f_{m\mathbf{k+q}}) \delta(\varepsilon_{n\mathbf{k}} - \varepsilon_{m\mathbf{k+q}} - \hbar\omega_{\mathbf{q}}) \\ & + (b_{\mathbf{q}} + f_{m\mathbf{k+q}}) \delta(\varepsilon_{n\mathbf{k}} - \varepsilon_{m\mathbf{k+q}} + \hbar\omega_{\mathbf{q}})), \end{aligned} \tag{6.11}$$

but in both cases they contain the scattering matrix g, which is characteristic for each scattering mechanism.

Scattering Rates

The first scattering mechanism is the acoustic deformation potential (ADP) scattering, for which the scattering matrix is given by:

$$g_{nm}^{\mathrm{ADP}}(\mathbf{k}, \mathbf{q}) = \sum_{\mathbf{G} \neq -\mathbf{q}}^{\text{acoustic}} \frac{\sqrt{k_B T} \widetilde{\mathbf{D}}_{n\mathbf{k}}}{\sqrt{\mathbf{C}}} \langle \psi_{m\mathbf{k+q}} | e^{i(\mathbf{q}+\mathbf{G}) \cdot \mathbf{r}} | \psi_{n\mathbf{k}} \rangle, \tag{6.12}$$

where $\mathbf{G}$ is a lattice vector, $\widetilde{\mathbf{D}}_{n\mathbf{k}} = \mathbf{D}_{n\mathbf{k}} + \mathbf{v}_{n\mathbf{k}} \bigotimes \mathbf{v}_{n\mathbf{k}}$, $\mathbf{D}_{n\mathbf{k}}$ is the deformation potential and $\mathbf{C}$ is the elastic constant. The deformation potential is the change in electron band energies caused by distortion of the lattice, which causes electrons to scatter by ADP scattering. This is the only process that is not electronically screened, as it is not mediated by charged entities.

Next we have the ionised impurity (IMP) scattering:

$$g_{nm}^{\mathrm{IMP}}(\mathbf{k},\mathbf{q}) = \sum_{\mathbf{G}\neq-\mathbf{q}} \frac{\sqrt{n_{\mathrm{IMP}}}Ze}{\epsilon_{\mathbf{s}}} \frac{\langle\psi_{m\mathbf{k}+\mathbf{q}}|e^{i(\mathbf{q}+\mathbf{G})\cdot\mathbf{r}}|\psi_{n\mathbf{k}}\rangle}{|\mathbf{q}+\mathbf{G}|^2+\beta^2}, \tag{6.13}$$

where n_{IMP} is the concentration of ionised impurities of charge Z, $\epsilon_{\mathbf{s}}$ is the static dielectric constant (note in this case the static dielectric constant refers to the sum of the ionic and high frequency dielectric constants) and β is the inverse scattering length. This describes scattering off of ionised impurities, either intrinsic or extrinsic, which are required to reach the optimum carrier concentration in thermoelectrics.

The polar optical phonon (POP) scattering is given by:[152]

$$g_{nm}^{\mathrm{POP}}(\mathbf{k},\mathbf{q}) = \sqrt{\frac{\hbar\omega_{\mathrm{po}}}{2}} \sum_{\mathbf{G}\neq-\mathbf{q}} \sqrt{\frac{1}{\epsilon_\infty} - \frac{1}{\epsilon_{\mathbf{s}}}} \frac{\langle\psi_{m\mathbf{k}+\mathbf{q}}|e^{i(\mathbf{q}+\mathbf{G})\cdot\mathbf{r}}|\psi_{n\mathbf{k}}\rangle}{|\mathbf{q}+\mathbf{G}|^2+\beta^2}, \tag{6.14}$$

where ϵ_∞ is the high-frequency dielectric constant. ω_{po} is the dipole-weighted polar-optical phonon frequency at the Γ point, which an approximation instead of using all the phonon frequencies at all q-points, as the dominant contribution to this mechanism is long range (i.e. near the Γ point) optical phonons via an interaction with a dipole. As the dipole interaction goes to zero with the frequency, this method does not consider the acoustic phonons.[153,154] This describes the scattering of electrons by optical phonons.

Finally we have the piezoelectric (PIE) scattering:

$$g_{nm}^{\mathrm{PIE}}(\mathbf{k},\mathbf{q}) = \sum_{\mathbf{G}\neq-\mathbf{q}}^{\mathrm{acoustic}} \frac{\sqrt{k_B T}\mathbf{h}}{\sqrt{\mathbf{C}}} \frac{\langle\psi_{m\mathbf{k}+\mathbf{q}}|e^{i(\mathbf{q}+\mathbf{G})\cdot\mathbf{r}}|\psi_{n\mathbf{k}}\rangle}{|\mathbf{q}+\mathbf{G}|^2+\beta^2}, \tag{6.15}$$

where $\mathbf{h}$ is the piezoelectric tensor. This scattering results from the piezoelectric effect, where an electric current causes the movement of dipolar portions of the material or vice versa, causing scattering. This can only happen if the material lacks an in-version centre.

The inverse scattering length, β, is defined as:

$$\beta^2 = \frac{e^2}{\epsilon_s k_B T V} \int D(\varepsilon) f(\varepsilon)(1 - f(\varepsilon)) d\varepsilon, \tag{6.16}$$

where V is the volume of the unit cell and $D(\varepsilon)$ is the electronic density of states. This accounts for the screening of the latter three processes by other electrons.

A simple method to represent grain boundary scattering, where the mean free path of the electrons is essentially capped at a certain distance, is also implemented.

7 VIBRATIONAL CALCULATIONS

Phonon Dispersions

Phonons are quantised lattice vibrations, which we use to understand the vibrational properties of a material, including kinetic stability and thermal transport. Phonon dispersions (Figure 6.2) are much like electronic dispersions, in that they show the energy (frequency) of the phonons along a high-symmetry path in k-space, and the gradients of the bands are equal to the group velocities of the phonons. They differ in that there are a fixed number of modes ($3N$ where N is the number of atoms), do not have a bandgap (or at least not in the important way non-metallic electronic structures have) and phonons are bosons rather than fermions, so they do not obey the Pauli exclusion principle, allowing multiple phonons to occupy the same state. The energies of the phonons are absolute, and the first three modes, the acoustic modes, always drop to zero at the Γ point, which corresponds to the in-phase movement of all the atoms, i.e. a translation of the crystal. Negative frequency modes show that a displaced atom has a negative restoring force, i.e. that it wants to go somewhere other than its original position, and the material is not kinetically stable.

Figure 7.1: The phonon dispersion and projected DoS of ZnO.

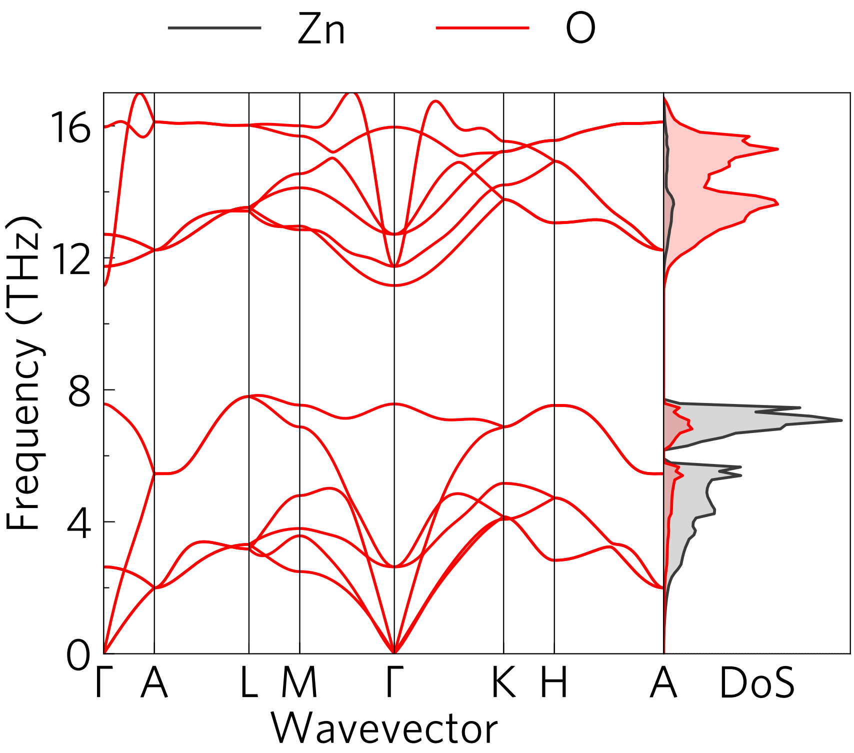

Force Constants

In order to calculate the phononic transport properties, we start with the crystal potential energy, Φ, which can be expanded as:

$$\begin{aligned}\Phi = &\Phi_0 \\ &+ \sum_{lk}\sum_{\alpha}\Phi_{\alpha}(lk)u_{\alpha}(lk) \\ &+ \frac{1}{2}\sum_{ll'kk'}\sum_{\alpha\beta}\Phi_{\alpha\beta}(lk,l'k')u_{\alpha}(lk)u_{\beta}(l'k') \\ &+ \frac{1}{3!}\sum_{ll'l''kk'k''}\sum_{\alpha\beta\gamma}\Phi_{\alpha\beta\gamma}(lk,l'k',l''k'')u_{\alpha}(lk)u_{\beta}(l'k')u_{\gamma}(l''k'') \\ &+ ...,\end{aligned} \tag{7.1}$$

where l are the unit cells, k are the atoms, α, β etc. are the modes, u are the displacements and Φ_0, Φ_α, $\Phi_{\alpha\beta}$ and $\Phi_{\alpha\beta\gamma}$ are the zeroth, first, second and third order force constants respectively. Here we use the Phonopy code[155], which uses the supercell approach, whereby atoms are displaced by 0.01 Å to induce a restoring force:

$$F_\alpha(lk) = -\frac{\partial \Phi}{\partial u_\alpha(lk)}, \tag{7.2}$$

which can be used to calculate the second-order force constants:

$$\frac{\partial^2 \Phi}{\partial u_\alpha(lk)\partial u_\beta(l'k')} = -\frac{\partial F_\beta(l'k')}{\partial u_\alpha(lk)}. \tag{7.3}$$

This enables us to calculate the dynamical matrix:

$$D^{\alpha\beta}_{kk'}(\mathbf{q}) = \sum_{l'} \frac{\Phi_{\alpha\beta}(0k, l'k')}{\sqrt{m_k m_{k'}}} e^{i\mathbf{q}\cdot(\mathbf{r}(l'k')-\mathbf{r}(0k))}, \tag{7.4}$$

where $\mathbf{r}$ is the atomic position, m is the atomic weight and $\mathbf{q}$ is the wavevector (in phonon calculations, q-points are used, which are analogous to k-points, except $\mathbf{q} = 2\pi\mathbf{k}$). When the dynamical matrix acts on the polarisation vectors of the modes, $\mathbf{e}_{\mathbf{q}j}$, the phonon frequencies, ω of those modes j can be obtained:

$$D(\mathbf{q})\mathbf{e}_{\mathbf{q}j} = \omega^2_{\mathbf{q}j}\mathbf{e}_{\mathbf{q}j}, \tag{7.5}$$

which can be constructed into a phonon dispersion, and also a phonon DoS. This same method can be applied, but with three phonons $\alpha\beta\gamma$ and a triple partial derivative, to obtain the third-order force constants and upwards. This accounts for some anharmonicity, which results in a complex shift to the frequencies of $\Delta\omega_{\mathbf{q}j} + i\Gamma_{\mathbf{q}j}$. The first term is a shift in the energy of the modes, while Γ is the imaginary phonon self-energy, from which the scattering lifetimes can be obtained. The factor of 2 in the definition varies by source,[156] but in Phono3py, the third-order version of Phonopy,[157] the scattering lifetimes are:

$$\tau_\alpha = \frac{1}{2\Gamma_\alpha(\omega_\alpha)}. \tag{7.6}$$

We can then obtain the lattice thermal conductivity:

$$\kappa_l = \frac{1}{NV}\sum_\alpha C_\alpha \mathbf{v}_\alpha \otimes \mathbf{v}_\alpha \tau_\alpha, \tag{7.7}$$

where N is the number of unit cells of volume V, $\mathbf{v}$ is the group velocity, the band gradient; and C is the heat capacity, which is a function of frequency:

$$C_\alpha = k_B \left(\frac{\hbar\omega_\alpha}{k_B T}\right)^2 \frac{e^{\frac{\hbar\omega_\alpha}{k_B T}}}{\left(e^{\frac{\hbar\omega_\alpha}{k_B T}} - 1\right)^2}. \tag{7.8}$$

Part IV

ThermoParser

8 INTRODUCTION

So far we have shown that thermoelectrics are complicated, requiring the calculation of phononic and electronic transport as integral parts of their assessment. This is reflected in the codes needed to simulate them — on top of the DFT code (e.g. VASP), there is one for electronic transport (e.g. AMSET), and normally two for the phononic transport, typically Phonopy and a third order+ code, here Phono3py. Each code has its own file format: in our case VASP uses a range of bespoke plain-text files and xml and binary files, AMSET uses json and hdf5 files, Phonopy uses yaml and plain text files and Phono3py uses hdf5. While some formats such as yaml are human-readable, others such as hdf5 are not, and either way they may be difficult to parse for some and tiresome for everyone. Each code has its own naming formats, for example Phono3py uses “qpoint” where AMSET uses “kpoints”; and data arrangement, e.g. AMSET supplies its data with the full 3×3 matrix where Phono3py gives the reduced 6×1 form:

$$\begin{bmatrix} xx & xy & xz \\ xy & yy & yz \\ xz & yz & zz \end{bmatrix} \equiv \begin{bmatrix} xx & yy & zz & yz & xz & xy \end{bmatrix} \tag{8.1}$$

Each also has its own preferred units and normalisation customs, and there may be variations between versions, e.g. some versions of Phono3py normalise their contributions to lattice thermal conductivity per mode per q-point, termed “mode_kappa”, by the number of points in the q-point mesh (an artificial construct used to make the calculation tractable, see Section 5.3), and some do not. Each of these intricacies compound the risk of human error in the calculations.

ZT is a complex property made of electrical conductivity, Seebeck coefficient, temperature and electronic and lattice contributions to the thermal conductivity, and each of the electrical transport properties can be broken down into influences such as mobility and scattering rates, of which six different types are used here. The lattice thermal conductivity is influenced by factors such as group velocity, scattering rate and mode occupation. Many of the quantities above have different values depending on temperature and carrier concentration, and can be broken down by band and q-point. The point is, there are many different quantities that can be described in many different ways, which interact, adding yet more ways to analyse them.

To help overcome these factors, we have written the code ThermoParser, which helps in all stages of thermoelectric calculations, from generating inputs to parsing data from multiple inputs into a consistent format, and then retrieving, analysing and visualising the data in both simple and complex ways. The code is written in as a Python package to enable people to have full control to creatively display their own data how they want, but also allows all basic functions to be done via a command-line interface (CLI), enabling quick and easy analysis of data whilst maintaining a high degree of customisability. The code is fully documented, which can be found at `https://smtg-ucl.github.io/ThermoParser/`.

9 ThermoParser

Input Generation

The smallest, but perhaps most broadly useful function is the ability to generate k-point files comprising of weighted and unweighted k-points. When calculating DoSs, which are used by electronic structure codes such as BoltzTraP and AMSET, the energies are required to be calculated both as accurately as possible, and as densely as possible with respect to the number of k-points. Accurate calculations require calculating the electronic wavefunction on a relatively dense mesh, which weighted on the weights of the k-points in the irreducible Brillouin zone in the overall cell in k-space. This is expensive to calculate, and requires a lower density of k-points than are useful for the DoS calculation, so two meshes can be combined: a weighted mesh to ensure accurate wavefunctions, and an unweighted mesh, which is not used to calculate the wavefunctions, and so is much cheaper to obtain a dense mesh of energy values. ThermoParser can construct this file, and suggest parallelisation options to further optimise the calculation.

Data Creation

Strictly speaking, the first major step facilitated by ThermoParser is the generation of data via BoltzTraP, although this ability has not been used in this thesis. BoltzTraP is a code which calculates electronic transport properties via the constant relaxation time approximation, which in itself is an efficient code for running a low level of theory very quickly. In its Python implementation, however, within a package called pymatgen, it is parsed into dictionaries, where each data point is explicitly linked to the condition it was simulated under, e.g. `{'seebeck': {'1000': 100}}`, signifying that the Seebeck at 1000 temperature is 100. This has the advantage of being relatively clear as to which conditions the simulation was run under, where the norm is to have independent sets of data, where it is left to the reader to infer that if there are ten temperatures and the second dimension of the Seebeck coefficient is ten long, the second dimension is probably temperature. On the other hand, this is relatively slow, computationally speaking, to write and read. This problem was foundational to the current form of ThermoParser. ThermoParser runs the efficient algorithms for extracting the Onsager coefficients from BoltzTraP, while detecting and handling some common bugs that vary by installation, and calculates the actual transport properties itself, placing the data in non-nested dictionaries, but providing the arrangement of the data along with other metadata as detailed in the next section. It is then saved as a hdf5 file.

Data Consolidation

Once the data has been created by the various codes, in order to be easily handled it is read by ThermoParser into a single format. The chosen format is a single dictionary, where each property has its own entry, and the order of the dimensions is first categorical variables such as scattering mechanism, then temperature, other condition variables such as carrier concentration, intrinsic variable such as band and q-point and lastly direction. This need not be remembered, as all the useful additional data is saved in the `meta` dictionary, an example of which is given below:

```
data[‘meta’] =
{‘kappa_source’:
```

```
    ‘phono3py’,
 ‘units’:
    {‘mode_kappa’:
        ‘W m-1 K-1’,
     ‘lattice_thermal_conductivity’:
        ‘W m-1 K-1’,
     ‘temperature’:
        ‘K’,
     ‘qpoint’:
        ‘’},
 ‘dimensions’:
    {‘mode_kappa’:
        [‘temperature’, ‘qpoint’, ‘band’, 3, 3],
     ‘lattice_thermal_conductivity’:
        [‘temperature’, 3, 3],
     ‘temperature’:
        [‘temperature’],
     ‘qpoint’:
        [‘qpoint’, 3]}}
```

This gives the source of the data (Phono3py), as well as the units and dimensions of each quantity (“3” refers to the direction, so `kappa` is a 3×3 matrix whereas `qpoint` is a 3×1 matrix). The units are made consistent between the codes by default, often adhering to SI units or the convention of the field. Any dependent variables are loaded in automatically, so all the data needed to know what everything refers to is always present. There is also a configuration file which allows alternative units and conversions to be specified, which are reflected in the metadata and later in the axis labels.

Data Handling

In order to turn the raw data into useful data, several operations are often done, such as specifying conditions such as temperature, and calculating further properties such as ZT. As well as being important for humans to understand the data, the metadata is read by ThermoParser to facilitate some of these processes, particularly for specifying conditions. An example of this in action at the command line is the `get` function:

```
$ tp get amset bmfp/transport_47x39x49.json -q
    power_factor -t 800 -n -2e19
The power factor in the avg direction at 800 K and
    -2.154e+19 carriers cm^-3 is 0.0626 W m-1 K-2.
```

This obtains a specific piece of data, only from the file and without interpolating (with the exception of ZT where it may be necessary if the calculated conditions are different for the electronic and phononic transport properties). Here the requested carrier concentration (`-n -2e19`) is not in the file and the direction has not been specified, but the actual conditions used have been stated verbosely to ensure transparency, along with all the units.

Data Visualisation

Finally there is the data visualisation, which is featured heavily in the rest of this thesis. There are a range of basic plot-types in common use, which are implemented at the command line, or constructable with four lines of code and one import through the Python package:

```
import tp
fig, ax, _ = tp.axes.large.one()
data = tp.data.load.phonopy_dispersion('band.yaml')
tp.plot.phonons.add_dispersion(ax,␣data)
fig.savefig('band.pdf')
```

These include phonon dispersions (Chapter 18) and ZT heatmaps (Sections 13.4 and 22.3 and chapter 23). An important modification of the dispersion is the stacked dispersion (Section 13.3), which can help with supercell convergence and is not trivial due to the varying x-axis scales.

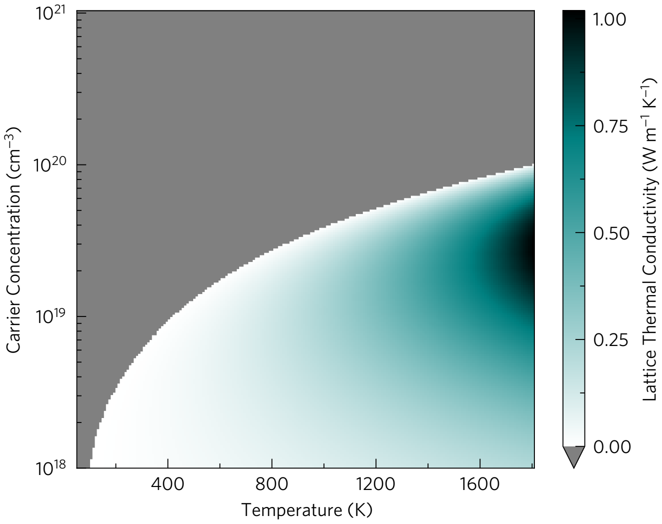

Figure 9.1: Maximum lattice thermal conductivity able to achieve a ZT of two for $BaSnO_3$.

There are also plot-types which are new to ThermoParser, to the best of our knowledge. Third order phonon calculations are extremely expensive, and one may not want to do them if a material is unlikely to become a good thermoelectric, so we developed the kappa-target plot shown in Figure 9.1, which gives the maximum lattice thermal conductivity allowable if one wants to reach a particular ZT. In this case, a lattice thermal conductivity of $1\,\mathrm{W\,m^{-1}\,K^{-1}}$ would be required to get a high ZT at even high temperatures, so if the goal of the study is to get a high moderate-temperature ZT, one might choose to move to another material. Another example is the average-rates plot (Sections 13.2 and 22.1), which shows the average of the charge carrier scattering rates weighted by the derivative of the Fermi-Dirac distribution at that carrier concentration and temperature, in the same way as is used to calculate the conductivity, therefore giving a more representative picture of the effect of the scattering rates than a raw plot of the rates.

The third application is using the Python interface to easily compare disparate sets of data. For example, many properties related to the lattice thermal conductivity, such as the group velocities and scattering lifetimes, cover a large range of values and so are best represented on a logarithmic scale. One might want to compare these properties to the phonon DoS in order to attribute characteristics to certain atoms, as we have done in

Section 22.2. ThermoParser makes plotting linear-scaled quantities on a log scale or vice versa straightforward, so the user only has to focus on what they want, and whether they should.

10 CONCLUSION

We have designed and written a Python package, ThermoParser, which assists with all stages of the thermoelectrics workflow, from writing inputs to retrieving and plotting data. It is built on a file system designed to be transparent and human-understandable, while also being customisable and expandable. It has several options for making more efficient use of the users time, from DFT calculation optimisation to goal analysis, and can quickly retrieve desired data. The largest section is dedicated to plotting the data, which offers a range of commonplace and new plot-types accessible easily from the command line for all, and it is also highly customisable, allowing users with a little Python experience to create complex new plots quickly to suit their needs. It is widely used within the group,[57,83,158–160] and also by a few people internationally, and we hope it will make thermoelectrics analysis more approachable and accessible to all who are interested.

Part V

Thermoelectric Evaluation of $BaBi_2O_6$

11 INTRODUCTION

The work in this chapter was published in the paper following paper, which is Ref. 158 and from which parts of this chapter are adapted:

- K. B. Spooner, A. M. Ganose, W. W. W. Leung, J. Buckeridge, B. A. D. Williamson, R. G. Palgrave and D. O. Scanlon, $BaBi_2O_6$: A Promising n-Type Thermoelectric Oxide with the $PbSb_2O_6$ Crystal Structure, *Chem. Mater.* **2021**, *33*, 7441.

As previously discussed, conductive oxides make interesting thermoelectric candidates due to their high n-type electrical conductivities, high thermal stabilities, and are well understood in general due to decades of research. That is, except for their high lattice thermal conductivities characterised by extremely long phonon mean free paths.[57] Therefore, the first method we will look at is simply finding a complex-structured oxide, in the hope that it will retain the favourable properties of conductive oxides, with a much reduced lattice thermal conductivity. $PbSb_2O_6$ was first discovered in the Cetine mine in Italy in 1996,[161] and so gave the former name of that mine, Rosia mine, to the crystal structure — Rosiaite. (The crystal structure itself was discovered at least 55 years previously in a range of antimonates and arsenates.[162]) It is a layered structure consisting of alternating layers of (1) edge-sharing SbO_6 octahedra, occupying two-thirds of the octahedral sites, and (2) Pb cations above the vacant octahedral sites. The Sb_2O_6 layers consist of a metal-oxygen network with metals in the np^0 ns^0 electronic structure, found in many traditional conductive oxides such as ZnO, which should be ideal for conducting charge carriers, while being more complex than such materials and so hopefully exhibiting stronger phononic scattering. Meanwhile, the Pb ions present a favourable site for doping, which will minimise the disruption to the conductive framework, and could possibly act as rattlers.

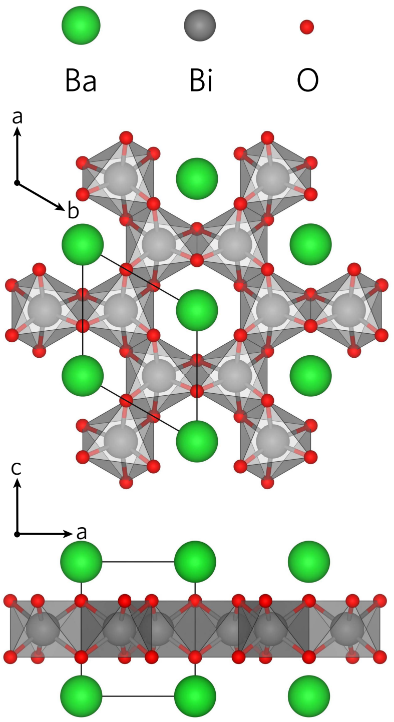

Figure 11.1: Crystal structure of BaBi$_2$O$_6$, through the layers (top) and along the layers (bottom). Ba, Bi, and O atoms are denoted by green, grey, and red spheres respectively. Drawn with Vesta.[164]

Unfortunately, due to the toxic Pb this is not a suitable material for a wide-scale thermoelectric, but in 2004 Mizoguchi et al.[163] synthesised a range of stannates, antimonates and bismuthates, including several antimonates and bismuthates in the rosiaite structure. Of those, CdSb$_2$O$_6$ contains the toxic Cd, so is unsuitable, and many others (and all those of other structures) were made of relatively light elements such as Mg, Ca and first and second row transition metal elements. Heavy elements vibrate at relatively low frequencies, and also have a high mass contrast with the O ions, preventing phonons from easily transmitting down these channels, so we determined the most promising candidate to be BaBi$_2$O$_6$ (Figure 11.1). While it is true that Bi is not especially earth abundant, at 2.5 ppm in the silicate earth by weight,[165] it is still around 30 times more abundant than the Se in SnSe (0.075 ppm), and does not have the toxicity of Pb in PbTe. Also, around 36 % is made of the highly abundant Ba (6,600 ppm) and O (around 500,000 ppm), whereas the Te in Bi$_2$Te$_3$ is only about five times more abundant than Bi (12 ppm). Besides elemental abundance, the synthesis method is also important to the sustainability of the material. Mizoguchi et al.[163] synthesised orange crystals of BaBi$_2$O$_6$ hydrothermally from NaBiO$_3$ and BaCl$_2 \cdot 6\,$H$_2$O at 410 K, and our experimental collaborators successfully reduced that to 360 K (90 °C),[158] making this a very low-energy synthesis.

Mizoguchi et al.[163] then used diffuse reflectance spectra and the Kubelka–Munk method[166] to ascertain the bandgaps, which was 2.6 eV for BaBi$_2$O$_6$, in agreement with its orange hue. This is a reasonable value for a thermoelectric: several of the other

$PbSb_2O_6$ structure had very large bandgaps of 4–5 eV, which makes it difficult to dope them sufficiently to achieve the required conductivity for thermoelectric performance. On the other hand, small bandgaps make it too easy to excite charges, resulting in ambipolar doping, which can approximately erase the Seebeck effect. Another rosiaite structure, $SrBi_2O_6$, also has a reasonable bandgap of 2.0 eV, but is less attractive due to elemental scarcity of Sr (19.9 ppm) compared to Ba; nevertheless it could make an informative comparative study at a later date. (While $CdSb_2O_6$ is reported to have a calculated bandgap of 2.1 eV, this uses the Perdew–Wang-86 (PW86) GGA functional,[167] which is likely an underestimation; the experimental bandgap is variously reported as 3.8 eV or 4.4 eV.) Saiduzzaman et al.[168] conducted a study on the photocatalytic properties of $BaBi_2O_6$ and other rosiaite-structured materials. They noted that the strong hybridisation of the Bi 6s and the O 2p orbitals caused a large conduction band dispersion, which reduced the band gap below the large values seen in other rosiaite-structured materials, contributing to its effective photodegradation of phenol. The high dispersion will also make it n-type conductive if dopable, which hopefully, owing to the not-too-big bandgap (in this study measured to be 2.33 eV), will be possible. The antimonates $PbSb_2O_6$ and $BaSb_2O_6$ had less disperse conduction bands and wider bandgaps. Indeed, several other bismuth oxides have been studied as thermoelectrics already.[79,169–171] The important distinction though is that the oxides with trivalent Bi are in p-type materials where the bismuth oxide component is insulating,[79,169,170] whereas in oxides with pentavalent Bi, the bismuth oxide component is n-type conductive.[171] (Bi can also function as a trivalent anion in oxide thermoelectrics,[172] and while the Bi contributes to the conductivity, in that case there is a much lesser interaction with the O due to their shared anionic character.) $BaBi_2O_6$ has pentavalent Bi, and is therefore hoped to be an effective thermoelectric.

12 METHODOLOGY

The energy cutoff and k-mesh density convergences, geometric relaxation and electronic dispersion calculations were conducted on the nine-atom primitive cell. The convergences, calculations for the second- and third-order force constants and density functional perturbation theory (DFPT) calculations used the PBEsol functional,[110] which is cheap and effective for calculating the structure of solids,[107–109] and has been shown to be accurate for lattice dynamics calculations.[111] The geometry relaxation and all optoelectronic calculations used the hybrid HSE06 functional,[115] which calculates accurate electronic properties.[116–131] The energy cutoff and k-mesh density were converged to within $10\,\mathrm{meV\,atom^{-1}}$, resulting in $400\,\mathrm{eV}$ and $3 \times 3 \times 3$ respectively, although an energy cutoff of $520\,\mathrm{eV}$ was used for the geometric relaxation to avoid Pulay stress.[139] These values were used as minimum values for all subsequent calculations. The geometry relaxation was done to within forces of $0.01\,\mathrm{eV\,Å^{-1}}$ on the atoms and within an electronic energy difference of $1 \times 10^{-5}\,\mathrm{eV}$ for electronic calculations, and the corresponding values for the phononic calculations are $1 \times 10^{-4}\,\mathrm{eV\,Å^{-1}}$ and $1 \times 10^{-8}\,\mathrm{eV}$ as these calculations are very sensitive. The second- and third-order force constants were calculated in $4 \times 4 \times 4$ (576 atom) and $2 \times 2 \times 2$ (72 atom) supercells repectively, the latter smaller as it required 2216 calculations, and a larger supercell would require more displacements in a much larger cell. The density of states (DoS) used for the electronic transport calculations used a $12 \times 12 \times 12$ k-mesh, which was interpolated therein to $91 \times 91 \times 75$, while the DFPT and optics calculations used

$14 \times 14 \times 12$ and $10 \times 10 \times 9$ meshes respectively, which were all converged to within 10 % for the outputs of each of those calculations.

13 Results

Geometry

The results of our HSE06 geometry relaxation is in good agreement with the experimental results of our collaborators[158] and of Mizoguchi et al.[163] (Table 13.1). There is a slight reduction in the c parameter in PBEsol, which makes is closer to the experimental results of Saiduzzaman et al.,[168] although overall it is probable HSE06 is more accurate due to its greater agreement with the majority of the experimental results in the c direction and all of them in the ab plane.

Electronic Properties

As hoped, the band structure and density of states (DoS, Figure 13.1) resemble other conductive oxides, with an O p state dominated valence band maximum (VBM), and a metal (in this case Bi) s state dominated conduction band minimum (CBM). The CBM is highly disperse, indicating it should be conductive if n-type doped, and to confirm this we calculated the charge carrier effective masses via the parabolic band fitting method (Table 13.2), and found that the electrons were lightest within the plane at $0.368\,m_\mathrm{e}$, but they were also light in the out-of-plane direction, at $0.527\,m_\mathrm{e}$.

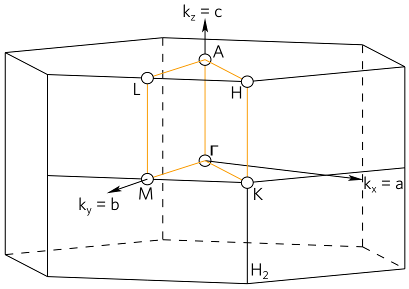

Figure 13.2: High-symmetry k-point path of the P31m space group to which $BaBi_2O_6$ belongs.

The MRTA results show that electronic scattering in $BaBi_2O_6$ varies in a complex way with carrier concentration and temperature (Figure 13.3). At low carrier concentrations, the lack of ionised impurities means that the ionised impurity (IMP) scat-

Table 13.1: The lattice parameters of BaBi$_2$O$_6$ obtained by our experimental collaborators[158] and our computational results, with percentage difference from our experimental results; and the experiments of Mizoguchi et al.[163] and Saiduzzaman et al.[168]. In all cases $\alpha = \beta = 90°$ and $\gamma = 120°$, and experiments were conducted at room temperature.

(Å (%))	Experiment[158]	PBEsol	HSE06
a, b	5.576(4)	5.610 (+0.61)	5.590 (+0.25)
c	5.789(7)	5.721 (-8.6)	5.806 (+0.29)

(Å)	Mizoguchi et al.[163]	Saiduzzaman et al.[168]
a, b	5.576(3)	5.575534(6)
c	5.785(7)	5.7381(1)

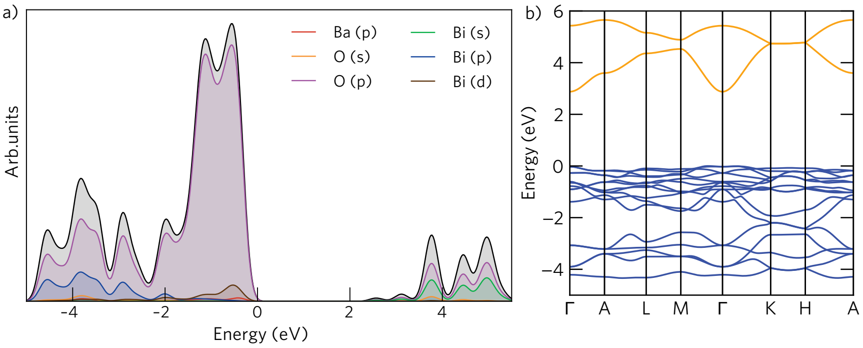

Figure 13.1: (a) density of states and (b) band structure of BaBi$_2$O$_6$ plotted with sumo.[141] In (b), the conduction band is in orange and the valence band in blue, with the valence band maximum set to 0 eV. The k-point path is using the Bradley–Cracknell formalism,[142] and the paths are shown in Figure 13.2.

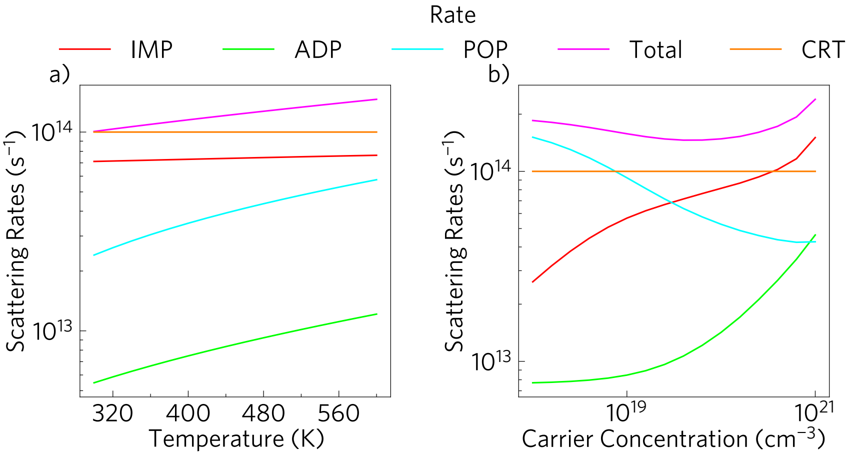

Figure 13.3: The rates are averaged over k-points and weighted by the normalised energy derivative of the Fermi–Dirac distribution. IMP is ionised impurity scattering (red), ADP is acoustic deformation potential scattering (green) and POP is polar optical phonon scattering (blue), which are summed to get total (pink). The constant relaxation time approximation (CRTA) results are also shown (orange).

tering is low, but around 1×10^{19} carriers cm^{-3} it becomes the dominant scattering mechanism. A 2D version of this plot is shown in Figure 13.5, which makes it clear that across carrier concentrations, polar optical phonon (POP) scattering increases with temperature at a higher rate than IMP scattering, which is favourable for thermoelectrics as they commonly operate best at high temperatures and carrier concentrations. It also reaches the lowest values at around 1×10^{19} carriers cm^{-3}, the optimal carrier concentration for many thermoelectrics. This is in stark contrast to constant relaxation time (CRT) scattering, which has a flat rate of 1×10^{14} s^{-1}, which is quantitatively only right at temperatures below 480 K and carrier concentrations below 4×10^{18} carriers cm^{-3}, conditions where thermoelectrics are not normally efficient. Qualitatively, it is never correct.

Table 13.2: The effective masses of the charge carriers in BaBi$_2$O$_6$ from HSE06, calculated by parabolic band fitting in the sumo package.[141] The layers are in the ab plane.

	Direction	m^*_e (m_e)
e$^-$	a, b	0.368
e$^-$	c	0.527
h$^+$	a, b	1.351

The consequences of these effects are shown in Figure 13.5. The electrical conductivity and the electronic contribution to the thermal conductivity are similar at low temperatures and carrier concentrations between the two methods, but at high carrier concentrations, as IMP scattering becomes large, CRT scattering overestimates the conductivity, up to a factor of two at 1×10^{20} carriers cm^{-3}. At low carrier concentrations, POP is dominant, which increases more rapidly with temperature than IMP scattering. This also results in an overestimation in conductivity of about a factor of two at low carrier concentrations

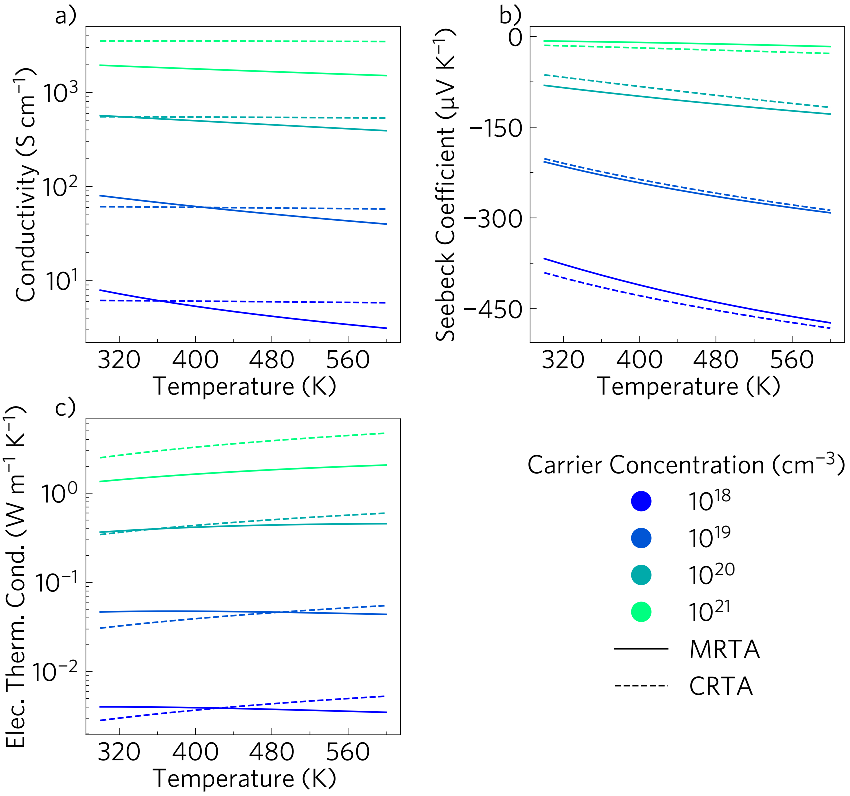

Figure 13.4: Direction-averaged (a) electrical conductivity, (b) Seebeck coefficient and (c) electronic thermal conductivity of $BaBi_2O_6$ against temperature for several carrier concentrations using the MRTA (solid lines) and CRTA (dashed lines).

and high temperatures. As the Seebeck coefficient does not depend on scattering, and the electronic thermal conductivity is normally low compared to the lattice thermal conductivity at carrier concentrations commonly optimal to thermoelectrics, this will lead directly to the overestimation of ZT.

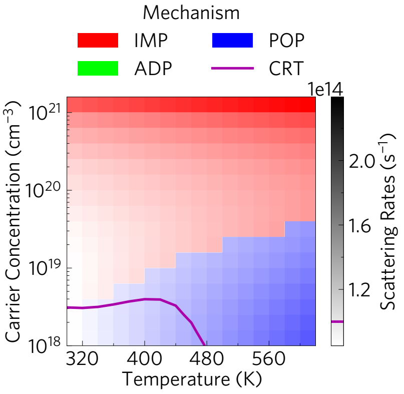

Figure 13.5: A 2D version of Figure 13.3. The darkness shows the overall scattering rate, while the colour indicates which is dominant. The contour shows the standard constant relaxation time rate of $1 \times 10^{14}\,s^{-1}$.

Phononic Properties

The convergence of the phonon dispersion of $BaBi_2O_6$ is shown in Figure 13.6. The supercells in which there are an odd number of cells in the *ab* plain have imaginary modes, indicating structural instability. This has consequences for the subsequent calculations: we need to do our calculations on structurally stable materials, which leaves us with the $2 \times 2 \times 2$, $4 \times 4 \times 3$ and $4 \times 4 \times 4$ supercells. Both the number of calculations and the computational expense increase rapidly with supercell size, so we have selected the $2 \times 2 \times 2$ supercell for the third order calculations, which is not strongly converged, but is kinetically stable

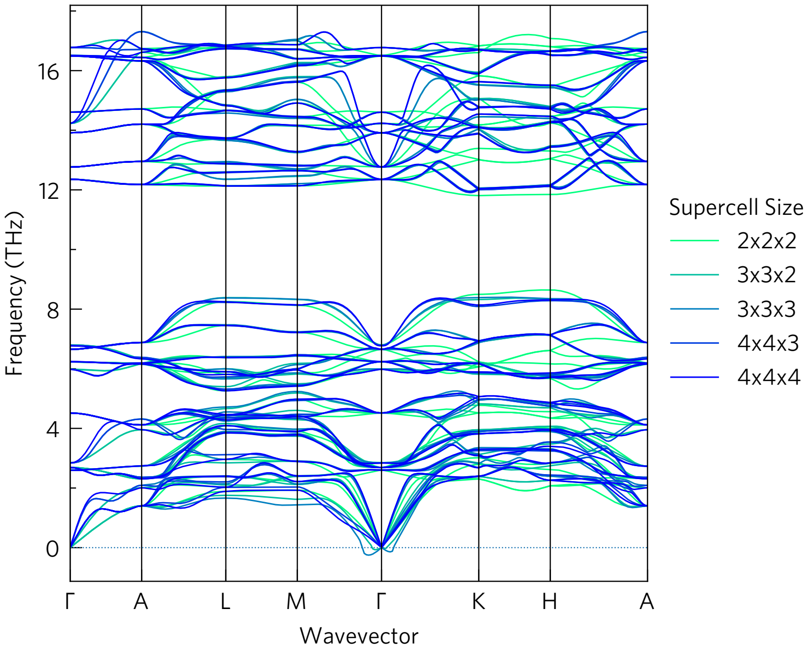

Figure 13.6: (a) Phonon dispersion of BaBi$_2$O$_6$ as calculated within the harmonic approximation (PBEsol/DFT) at the equilibrium (athermal) lattice constants using Phonopy[155] and plotted with ThermoPlotter.[158] The k-point path is using the Bradley–Cracknell formalism,[142] and the paths are shown in Figure 13.2.

and not excessively expensive. The $4 \times 4 \times 4$ cell was used for the relatively cheaper second order calculations, as two phonon interactions have longer range than three phonon interactions.

In terms of actual material properties, the relatively flat phonon modes of BaBi$_2$O$_6$ (away from the Γ point acoustic modes) indicate low phonon group velocity. Looking at the data from the third order force constant calculations (Figure 13.8), we can also see some more in-depth information about the phononic transport properties. For example, in Figure 13.8(a), we can see that the greatest contribution to the lattice thermal conductivity is from low frequency modes. This can be tracked back to the long phonon lifetimes or mean free paths in (c) or (d) respectively. The other component is the group velocities (Figure 13.8(b)), and while they are not so pronouncedly larger at low frequencies as the lifetimes or mean free paths, they are lower than the experimental record-holding oxide thermoelectric ZnO, likely due to the heavier atoms (Figure 13.7). Overall, this leads to a lattice thermal conductivity that is quite low, as shown in Figure 13.9(a): less than 4 W m^{-1} K^{-1} above 300 K in the in-plane direction and less than 2.5 W m^{-1} K^{-1} in

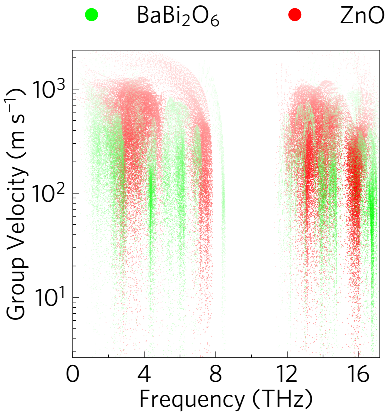

Figure 13.7: Comparison of the phonon group velocities of BaBi$_2$O$_6$ (green) with ZnO (red). Colour intensity denotes data density.

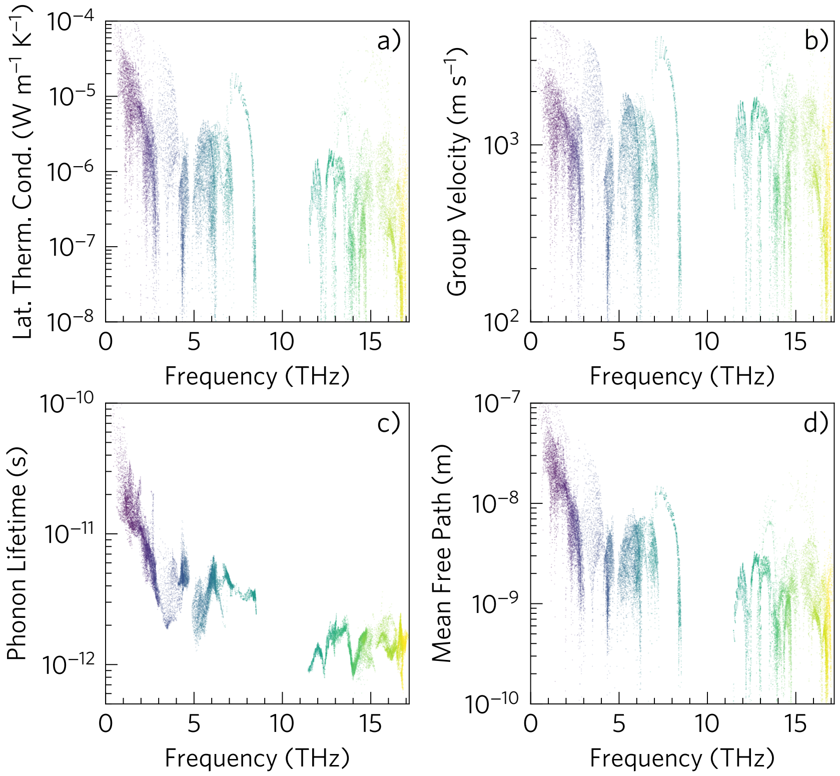

Figure 13.8: (a) Lattice thermal conductivity, (b) group velocity, (c) phonon lifetimes and (d) mean free paths of phonons at each band and q-point against frequency. Colour indicates band index.

the out-of-plane direction. At the 600 K, this is 2.08 W m^{-1} K^{-1} and 1.23 W m^{-1} K^{-1} respectively.

ZT

Bringing the electronic and phononic properties together, a *ZT* of 0.18 is reached in the in-layer direction, or 0.19 in the out-of-layer direction at 600 K, slightly below its melting temperature.

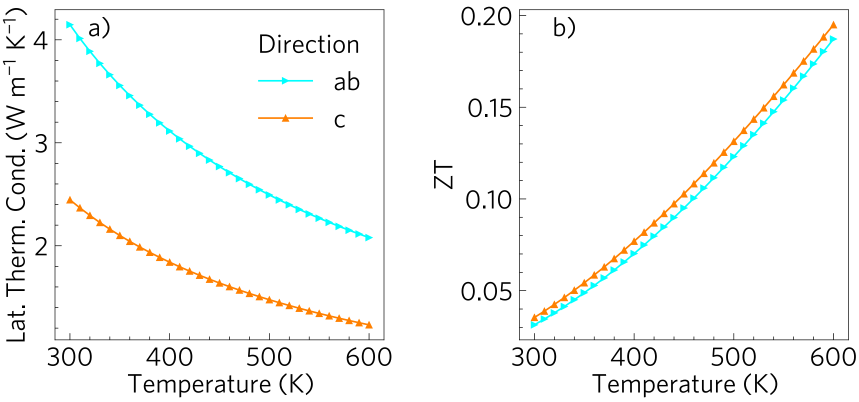

Figure 13.9: (a) Lattice thermal conductivity and (b) ZT of $BaBi_2O_6$ against temperature in the in-plane (ab) and out-of-plane (c) directions. (b) is for 6.3×10^{19} carriers cm^{-3}, the optimal carrier concentration at 600 K.

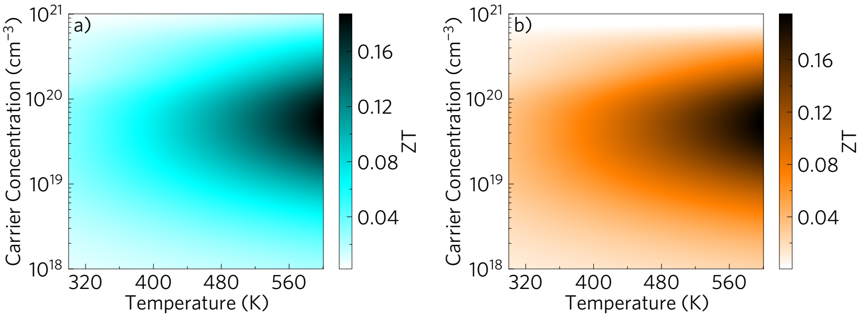

Figure 13.10: ZT of single-crystal BaBi$_2$O$_6$ against temperature and carrier concentration in the (a) in-layer (ab) and (b) out-of-layer (c) directions. The darkest colours indicate the highest ZT.

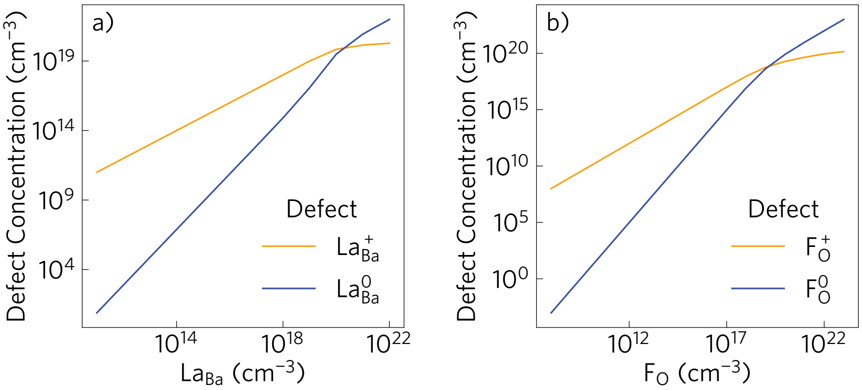

Figure 13.11: Effect of extrinsic (a) La$_{Ba}$ and (b) F$_O$ doping in BaBi$_2$O$_6$.

The average ZTs between 300–600 K are 0.10 and 0.11 respectively. This occurs at 6.3×10^{19} carriers cm^{-3}, which our defect calculations show is achievable with 3×10^{21} cm^{-3} of F or only 9×10^{19} cm^{-3} of La. These numbers are higher than the number of carriers required as (particularly at higher dopant concentrations) neutral defects can be formed rather than charged ones, leading to diminishing returns. This is shown in our SC-Fermi[173] analysis (Figure 13.11), where we can see this is right on the edge of what F can supply, indicating La to be a more promising dopant.

14 DISCUSSION

Perhaps the most direct benchmark to compare $BaBi_2O_6$ to is $SrTiO_3$, as the highest-ZT earth-abundant oxide thermoelectric in this temperature range. While the ZT of $BaBi_2O_6$ is 14–18 % smaller than that of $SrTiO_3$ at 570 K (0.22),[174] these calculations are for perfect (infinite) crystals, while realistic devices would have grain boundaries and other defects, besides the ionised impurities accounted for here. Figure 14.1(a) shows the cumulative lattice thermal conductivity against frequency. As one might expect, the low frequency modes, up to 4 THz in this case, are dominated by the heavier atoms, Ba and Bi. This is also the region below which 80 % of in-plane, and 90 % of out-of-plane lattice thermal conductivity arises. Ba in particular forms a layer of its own in the out-of-plane direction, so could be particularly potent in disrupting the phonon transport. This makes La a particularly interesting dopant, as it is an effective dopant, and can also possibly disrupt phonon transport through the Ba site it favours so La could play double duty as an electron enabler and a phonon finagler. Due to the small mass difference between La and Ba though, perhaps other Ba site dopants could be more effective at disrupting phonon transport, but maybe at the cost of reduced effectiveness as an electron donor.

In Figure 14.1(b), we show the cumulative lattice thermal conductivity against mean free path. In a famous case of nanostructuring, the PbTe-derived $AgPb_{18}SbTe_{20}$ was nanostructured to a grain size of 20 nm,[40] enhancing its ZT from ~0.5[175] to 2.2. Taking this to be a generally achievable level of nanostructuring, although testing on this specific material would of course be

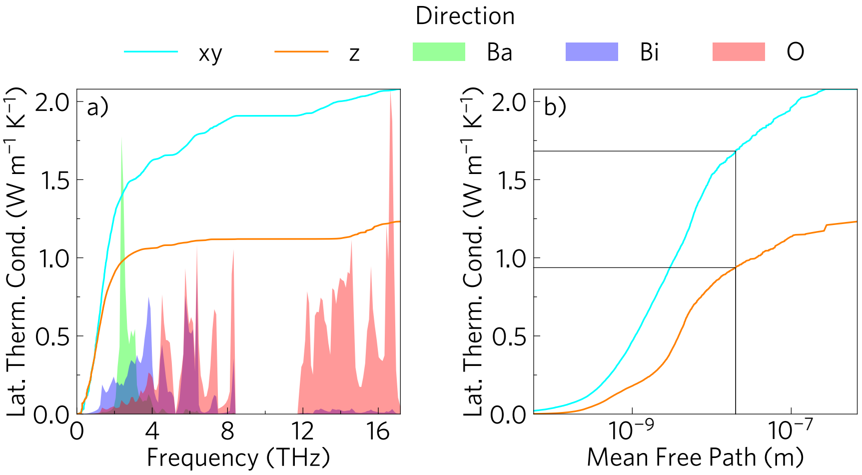

Figure 14.1: The direction-averaged cumulative lattice thermal conductivity at 600 K of BaBi$_2$O$_6$ against (a) frequency, with the phonon density of states overlaid and (b) mean free path, with markers showing the lattice thermal conductivity of the phonons of mean free path less than 20 nm.

necessary, we can see that around 20–25 % of the lattice thermal conductivity comes from phonons with mean free paths longer than 20 nm at 600 K. This results in a $\frac{1}{3}$ reduction in lattice thermal conductivity, from 1.8 W m^{-1} K^{-1} to 1.2 W m^{-1} K^{-1} when direction-averaged (Figure 14.2(d)).

Unfortunately, nanostructuring also disrupts the electronic transport, but fortunately, since we are using the MRTA, we can simulate this as well. Figure 14.2(a–c) show the effects of nanostructuring to 20 nm on the electronic transport properties. Scattering has little effect on the Seebeck coefficient, but reduces the electrical conductivity and power factor by 10–25 %, with the lowest decreases in that range occurring at the highest temperatures due to the naturally higher scattering due to thermal excitation in that range. Overall this leads to a slight increase in ZT to 0.22 (Table 14.1, Figure 14.3), the same as that of SrTiO$_3$, however given this is a new material and has not been subject to the level of study SrTiO$_3$ has, we hope it can exceed this value. The average ZT between 300–600 K is 0.12.

It may also find use beyond thermoelectrics, such as as an electron transport layer (ETL). ETLs are an integral part of electronic devices, needed to shuttle electrons between other components, which require high n-type conductivity. BaBi$_2$O$_6$ fulfils this requirement, with electron mobilities of 30–40 cm^2 V^{-1} s^{-1}

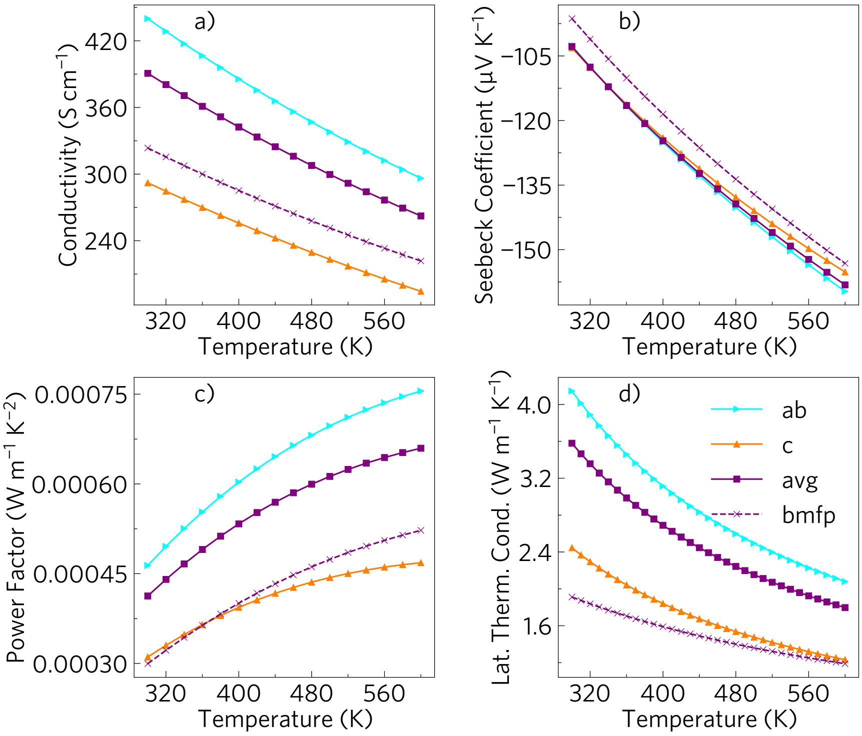

Figure 14.2: The (a) electrical conductivity, (b) Seebeck coefficient, (c) power factor and (d) lattice thermal conductivity in each direction, directionally averaged and nanostructured to 20 nm.

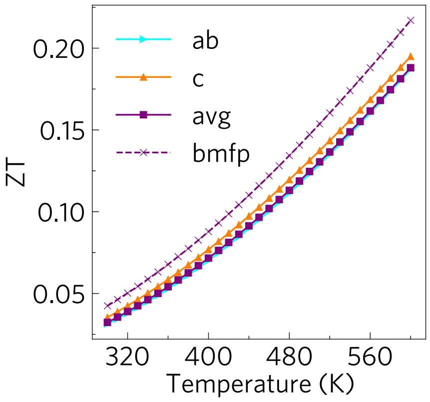

Figure 14.3: The ZT in each direction, directionally averaged and nanostructured to 20 nm.

Direction	CRTA		
	n (cm^{-3})	PF (W m^{-1} K^{-2})	ZT
ab	4.0×10^{19}	8.38×10^{-4}	0.21
c	4.0×10^{19}	4.82×10^{-4}	0.21
avg	4.0×10^{19}	7.20×10^{-4}	0.21
bmfp	4.0×10^{19}	7.20×10^{-4}	0.30

Direction	MRTA		
	n (cm^{-3})	PF (W m^{-1} K^{-2})	ZT
ab	6.3×10^{19}	7.00×10^{-4}	0.17
c	6.3×10^{19}	4.44×10^{-4}	0.19
avg	6.3×10^{19}	6.15×10^{-4}	0.18
bmfp	6.3×10^{19}	5.22×10^{-4}	0.22

Table 14.1: ZT from the CRTA and MRTA in the in-layer (ab), out-of-layer (c) and average directions, the latter additionally with a boundary mean free path of 20 nm applied, along with the carrier concentration (n) and power factor (PF) at that point at 600 K.

at 300 K with 1×10^{20} carriers cm^{-3}, which we have shown is achievable with La doping. While this is not best-in-class, it compares favourably with other high-mobility ETLs such as WO_3, which has a mobility of around 10 cm^2 V^{-1} s^{-1} at similar temperatures.[176,177] A good ETL must also have a compatible physical structure with the components it contacts, and the electronic structure must also be aligned appropriately. For example, in a solar cell, once the photovoltaic material absorbs a photon, the resultant excited electron must move into the ETL, and to facilitate this the ETL's conduction band must be slightly lower in energy than the photovoltaic's. For these reasons a wide range of ETLs are desired, and $BaBi_2O_6$ could be a valuable addition to that library, although further study would need to look into its band alignment to confirm if it would be appropriate for any particular application.

15 CONCLUSION

We set out to analyse $BaBi_2O_6$ for thermoelectric properties by using hybrid DFT and state-of-the-art electronic calculations, which fortuitously revealed a high n-type conductivity, which means it could be suitable as an ETL. These calculations also give a moderate Seebeck coefficient, and our phononic transport calculations show a low lattice thermal conductivity. Our calculations show an easy-to-manufacture powder of $BaBi_2O_6$ could have a ZT of 0.18 at 600 K, competitive with the current leading earth-abundant thermoelectric oxide $SrTiO_3$ at a similar temperature, which has been more intensely studied and optimised. Meanwhile, due to its layered nature, lattice thermal conductivity is suppressed in the out-of-plane direction, leading to single-crystal $BaBi_2O_6$ having a ZT of 0.19 in that direction. The detailed data we are able to extract from Phono3py has shown that the majority of the lattice thermal conductivity comes from low frequency, Ba-dominated modes, which could be a target for efforts to reduce this, such as with La doping. Through using the MRTA, we were also able to give a more accurate estimation of the conductivity, which is lower than the CRTA predicts, and a more complete picture of the effectiveness of nanostructuring leading to a ZT of 0.22 rather than 0.30. Overall, we have shown $BaBi_2O_6$ to be an effective earth-abundant oxide thermoelectric and ETL, and offered ways in which it might be improved further, beyond its current competitors.

ACKNOWLEDGEMENTS

This was split between myself, Dr. Alex M. Ganose and our experimental collaborator Dr. W. W. Winnie Leung, the latter of whom was supervised by Prof. Robert G. Palgrave. Regarding the computational work, Alex ran the electronic and phononic structure calculations, and defect calculations and most of the analysis of the defects, while I ran the additional calculations required for the MRTA (DFPT and optics calculations), and did the majority of the rest of the computational analysis. I have therefore excluded most of the defects and experimental sections, but have retained the electronic and phononic band structures as they are fundamental to later arguments.

Part VI

Structural Stability of Zn_2NX (X = Cl, Br, I)

16 INTRODUCTION

Our first method looked at finding a complex structured material from some chemical principles, but our next one will try and improve an existing one. As previously mentioned, ZnO has the highest experimentally realised ZT for a transparent conducting oxide (TCO). While the base material has an extremely high lattice thermal conductivity, nanostructuring has overcome this,[40,57] allowing it to combine favourable electrical and thermal conductivity. Nevertheless, grain boundaries scatter electrons as well as phonons, so it would be beneficial to find other ways to reduce the lattice thermal conductivity, which doesn't necessarily reduce the electrical conductivity. Ion substitution is one way in which new materials can be found with similar properties to existing one, by replacing an ion with a charge-balanced combination of other ions. To use an example from photovoltaics, CdTe is a photovoltaic which has been studied since at least the 1950s,[178,179] reaching efficiencies of 21.5 %,[180] but faces controversy around the toxic Cd and somewhat toxic Te.[181] By replacing the Te with S and/or Se and substituting Cd to Cu, and In and Ga, one can obtain the non-toxic $Cu(In,Ga)(S,Se)_2$, termed CIGS or CIGSSe,[182]which has reached efficiencies of 23.4 %.[183] Due to the low abundances of In and Ga, these can be substituted to Zn and Sn to make $Cu_2ZnSn(S,Se)_4$ (CZTS or CZTSSe)[184,185] to make a much more abundant material, who's efficiency has unfortunately stalled at 11 %.[186] Therefore, the method is no guarantee of success, or certainly not for photovoltaics. Nevertheless, in 2013 Liu et al.[187] successfully synthesised the anion-substituted daugh-

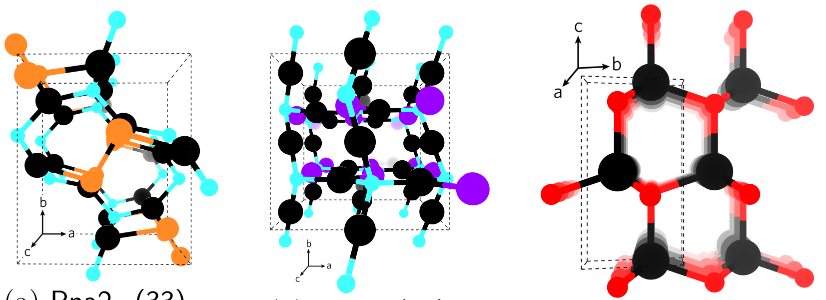

(a) $Pna2_1$ (33) (b) Pnma (62) (c) $P6_3mc$ (186)

Figure 16.1: (a) The $Pna2_1$ (33) structure reported experimentally for Zn_2NCl and Zn_2NBr,[187] (b) The Pnma (62) structure reported experimentally for Zn_2NI[187] and (c) The $P6_3mc$ (186) structure of ZnO.

ter elements of ZnO, Zn_2NX (X = Cl, Br, I). As single crystals they were colourless, indicating some similarity to the transparent ZnO, and this was backed up by a HSE06 band structure calculation, giving a 3.7 eV bandgap of Zn_2NCl. This calculation also showed a disperse conduction band, one of the beneficial properties of ZnO for not only thermoelectrics, but as a TCO. While these calculations were also done for the other materials, the less accurate PBE and PBE+U were used, which yielded much smaller bandgaps.

Experimentally using single-crystal XRD, they determined the structure of Zn_2NCl and Zn_2NBr to be the $Pna2_1$ (33) structure shown in Figure 16.1(a), which contains the hexagonal motif familiar from the ZnO $P6_3mc$ (186) structure (Figure 16.1(c)), whereas Zn_2NI forms the Pnma (62) structure (Figure 16.1(c)). Our calculations dispute this, so this chapter will be on our analysis of the structure of these materials, as well as ZnO itself to validate our methods.

17 METHODOLOGY

The initial convergence and geometry calculations were done on the 16-atom primitive cells, with energy cutoff and k-point convergence to $5\,\mathrm{meV\,atom^{-1}}$ in PBEsol for all materials, with results shown in Table 17.1. Geometry was relaxed until ionic forces were less than $1 \times 10^{-5}\,\mathrm{eV\,Å^{-1}}$ and electron energy was converged to within $1 \times 10^{-8}\,\mathrm{eV}$ with LDA, PBE and PBEsol functionals. These relaxed geometries are where the total energy was calculated. Phonon calculations were conducted on each structure and converged visually against supercell size, any imaginary modes were mapped and the relaxations and phonon calculations were repeated for the structures in the wells.

Material	Phase	ENCUT	k-mesh
Zn_2NCl	$Pna2_1$ (33)	250	$6 \times 5 \times 7$
Zn_2NCl	Pc (7)	250	$6 \times 5 \times 7$
Zn_2NBr	$Pna2_1$ (33)	300	$5 \times 5 \times 6$
Zn_2NI	Pnma (62)	300	$5 \times 6 \times 4$
Zn_2NI	$Pna2_1$ (33)	300	$5 \times 5 \times 6$
ZnO	$P6_3mc$ (186)	450	$5 \times 5 \times 3$

Table 17.1: Plane-wave energy cutoffs (ENCUTs) and k-point grids used used for the primitive cells of each material, converged to $5\,\mathrm{meV\,atom^{-1}}$.

18 Results

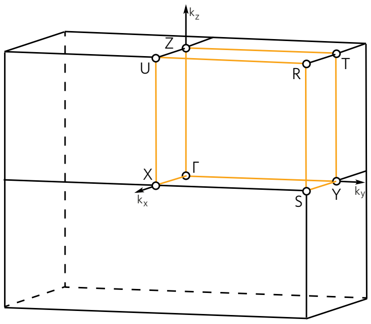

Figure 18.1: High-symmetry k-point path of the space groups to which Zn_2NX belong.

We first relaxed the structures of Liu et al.:[187] The $Pna2_1$ (33) phase of Zn_2NCl and Zn_2NBr and the Pnma (62) phase of Zn_2NI, as well as the $P6_3mc$ (186) phase of ZnO. ZnO and Zn_2NBr showed no imaginary modes with any of the functionals (Figure 18.2), showing them to be stable. Zn_2NCl was found to be unstable with all three functionals, with PBE and PBEsol giving visually similar results, distinct from those of LDA (Figure 18.3). When when the imaginary mode at Γ was mapped, in PBE and PBEsol this resulted in a double well potential (Figure 18.4(a)). The structures in the wells were in the Pc (7) spacegroup, and had no imaginary modes (Figure 18.4(b)). The imaginary mode at Γ with LDA did not produce a double well, and we have not so far managed to find a way to remove it. The phonon dispersions of Zn_2NI were highly kinetically unstable with all three functionals, exemplified by PBEsol in Figure 18.5(a). Mapping the largest imaginary mode at Γ resulted in a double well in all three cases, and the structure

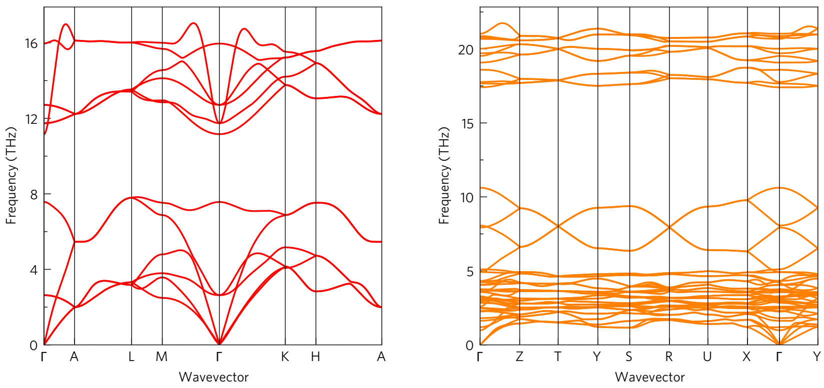

(a) ZnO $P6_3mc$ (186)

(b) Zn_2NBr $Pna2_1$ (33)

Figure 18.2: The PBEsol phonon dispersions of (a) ZnO in the $P6_3mc$ (186) structure ($6 \times 6 \times 4$ supercell) and (b) Zn_2NBr in the $Pna2_1$ (33) structure ($3 \times 3 \times 4$ supercell).

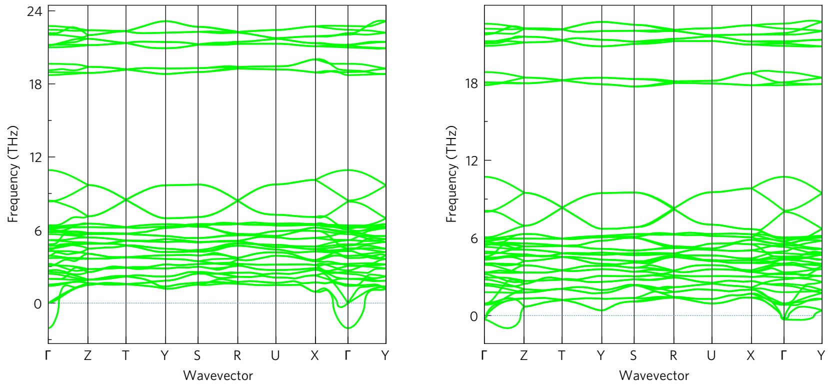

(a) LDA

(b) PBEsol

Figure 18.3: The unstable LDA and PBEsol phonon dispersions of Zn_2NCl in the $Pna2_1$ (33) structure in the $3 \times 3 \times 4$ and $2 \times 2 \times 3$ supercells respectively.

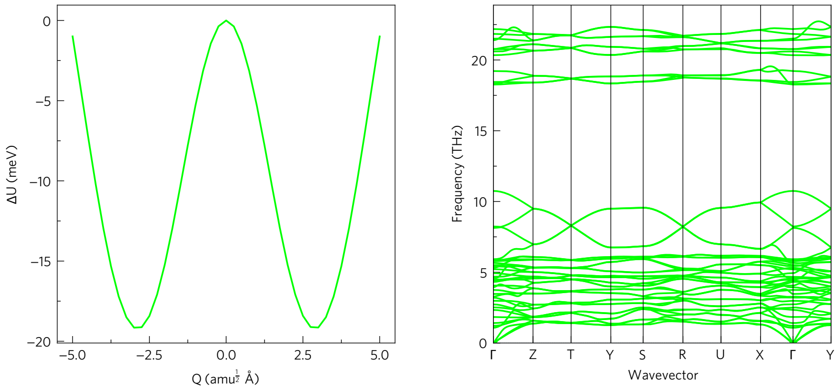

(a) PBEsol Zn_2NCl $Pna2_1$ (33) modemap at Γ

(b) Dispersion after Γ correction

Figure 18.4: (a) the energy wells around the imaginary phonon modes at the Γ-point in the PBEsol phonon dispersion of Zn_2NCl in the $Pna2_1$ (33) structure, and (b) the phonon dispersion after changing the structure to the Pc (7) structure in the left-hand energy well and re-relaxing.

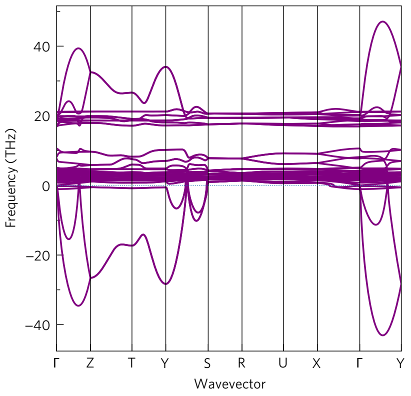

(a) Zn$_2$NI Pnma (62)

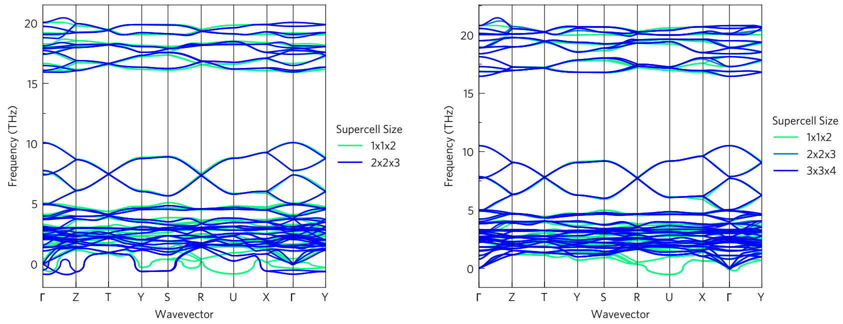

(b) Zn$_2$NI Pna2$_1$ (33) — PBE (c) Zn$_2$NI Pna2$_1$ (33) — PBEsol

Figure 18.5: The phonon dispersion of Zn$_2$NI (a) in the experimental Pnma (62) structure using the PBEsol functional and (b,c) in the Pna2$_1$ (33) structure of the other nitrohalides using the PBE and PBEsol functionals respectively, showing convergence against supercell size. (a) is representative of all the Pnma (62) dispersions.

in the well was the same Pna2$_1$ (33) structure as Zn$_2$NCl and Zn$_2$NBr were found to be in experimentally. The wells for LDA and PBEsol were around 10–20 meV, on par with those of the Zn$_2$NCl wells, and resulted in kinetically stable structures (Figure 18.5(c)). PBE, however, had a very shallow double well of only 0.1 meV, and did not result in a stable structure (Figure 18.5(b)). The unstable mode at Γ was mapped in the new structure, resulting in an unusual single well, with a plateaux where the other well would normally be (Figure 18.6(a)). The structure in the well was also in the Pna2$_1$ (63) structure, this time kinetically stable (Figure 18.6(b)).

As well as kinetic stability, we can also assess the thermodynamic stability. As the structures all contain the same atoms, this can be done by simply comparing the total energies in VASP, which while not physically meaningful, are still meaningful relative to other iso-atomic structures. Interestingly, all structures, regardless of stability, have extremely similar ener-

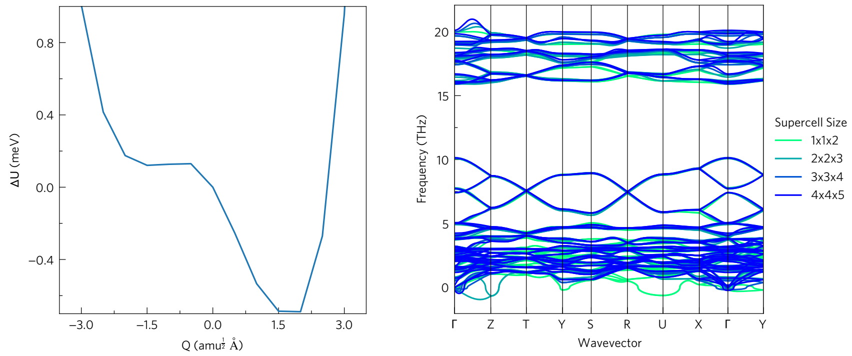

(a) PBE Zn_2NI $Pna2_1$ (33) energy at Γ

(b) Dispersion after Γ correction

Figure 18.6: The energy well around the imaginary phonon mode at Γ in the PBE phonon dispersions of Zn_2NI in the $Pna2_1$ (33) structure, and the phonon dispersion after changing the structure to that in the energy well and re-relaxing.

Material	Space Group	a (Å)	b (Å)	c (Å)	E (eV atom^{-1})
Zn_2NCl	$Pna2_1$ (33)	6.009	7.071	5.773	-3.909
	Pc (7)	6.009	7.069	5.774	-3.909
Zn_2NBr	$Pna2_1$ (33)	6.162	7.430	5.978	-3.794
Zn_2NI	Pnma (62)	6.311	6.183	7.755	-3.625
	$Pna2_1$ (33)	6.314	6.165	7.741	-3.626
ZnO	$P6_3mc$ (186)	3.237	3.237	5.222	-4.852

Table 18.1: PBEsol lattice parameters, energies and kinetic stabilities.

gies, within 1 meV atom^{-1} relative to other iso-atomic structures (Table 18.1). This could provide some justification for the Pnma (62) structure found in experiment, as while not kinetically stable, it is very nearly thermodynamically stable, and external factors such as the environment of the reaction could have favoured the Pnma (62) structure to the $Pna2_1$ (33) structure.

19 DISCUSSION

We have studied the structures of Zn_2NX (X = Cl, Br, I) using LDA, PBE and PBEsol functionals. First, we calculated the phonon dispersion of ZnO in each functional, which confirmed all three functionals correctly predict that the ZnO wurzite structure is kinetically stable, adding credibility to the subsequent results. This also gives the opportunity to compare the lattice parameters of a well established structure (Table 19.1) to help assess the relative reliability of the functionals. Reeber[188] studied the lattice parameters of ZnO at a range of temperatures down to 4.2 K. This allows us to compare our athermal calculated lattice parameters with experimental values with reduced thermal expansion compared to room temperature measurements, and therefore more accurately compare the functionals to experiment. We find PBEsol gives the closest values to experiment of 3.237 Å in the *ab* direction and 5.22 Å in the *c* direction, which differ from experiment by only −0.34 % in the *ab* direction and 0.35 % in the *c* direction, while PBE had differences of 1.2 % in the *ab* direction and 1.9 % in the *c* direction; and LDA had differences of −1.6 % in the *ab* direction and −0.81 % in the *c* direction. It is also notable that even at 296 K, approximately room temperature, PBE overestimates the lattice parameters of ZnO, beyond any plausible claim of thermal expansion. By another metric, the $c : a$ ratio, PBEsol actually performs poorest. All three functionals overestimate the ratio, but PBE and LDA only overestimate by 0.69 %, while PBEsol overestimates by 0.84 %, however this difference is relatively slight compared to the difference to experiment, so overall we will consider PBEsol to be the more accurate functional here.

The main results presented here suggest the structures of Zn_2NX (X = Cl, Br, I) all share space groups closely related to the $Pna2_1$ (33) one reported previously for the chloride and bromide.[187] The bromide results here are in strong agreement with experiment, predicting the same $Pna2_1$ (33) structure to be kinetically stable, with lattice parameters in good agreement (Table 19.1), particularly considering the experimental temperature of 293 K will likely lead to some lattice expansion in the experimental structure — and again, since PBE already overestimates the a and c lattice parameters, it is possible this is not the most appropriate functional.

The chloride, on the other hand, disagrees slightly with experiment. In this case, all three functionals underestimate the lattice parameters relative to the experiment, but more importantly they all also find the $Pna2_1$ (33) structure to be kinetically unstable. Mapping their modes reveals in PBE and PBEsol, the atoms rearrange slightly, particularly in the b direction, to get two lower symmetry Pc (7) structures to 1×10^{-4} Å precision. This new structure is not thermodynamically more stable than the experimental one, so possibly the experiment did make the $Pna2_1$ (33) structure, despite its kinetic instability. Another possible explanation is that there is a mix of the two Pc (7) structures in the experiment, which were averaged in the XRD data, so they appear to be the $Pna2_1$ (33) structure. The final functional, LDA has so far not yielded a kinetically stable structure.

The iodide was the anomaly in the experiment, forming a Pnma (62) phase. Here, however, that structure showed significant kinetic instabilities, and we found it to be kinetically stable in the same $Pna2_1$ (33) structure with LDA and PBEsol as Zn_2NBr. This has lead to some unexpected insights into the system. Firstly, the phonon dispersion of Zn_2NI in the $Pna2_1$ (33) structure at first appears to be significantly different from

Table 19.1: Lattice parameters from our calculations and previous experimental values,[187,188] to which the percentage difference has been given (the ZnO differences are given to the first 4.2 K measurement, and the differing definitions of the long axis are taken into account for Zn_2NI). In all cases $\alpha = \beta = \gamma = 90°$ for Zn_2NX, and $\alpha = \beta = 90°$ and $\gamma = 120°$ for ZnO.

Material	Source	Space Group	a (Å (%))	b (Å (%))	c (Å (%))
Zn_2NCl	LDA	$Pna2_1$ (33)	5.939 (-3.0)	6.973 (-5.6)	5.703 (-3.9)
	PBE	Pc (7)	6.102 (-0.36)	7.219 (-2.9)	5.880 (-0.95)
	PBEsol	Pc (7)	6.009 (-1.9)	7.069 (-4.3)	5.774 (-2.7)
	Experiment (100 K)[187]	$Pna2_1$ (33)	6.1241(9)	7.3884(11)	5.9362(9)
Zn_2NBr	LDA	$Pna2_1$ (33)	6.098 (-1.9)	7.314 (-4.4)	5.905 (-3.0)
	PBE	$Pna2_1$ (33)	6.249 (+0.55)	7.627 (-0.34)	6.100 (+0.23)
	PBEsol	$Pna2_1$ (33)	6.162 (-0.85)	7.430 (-2.9)	5.978 (-1.8)
	Experiment (293 K)[187]	$Pna2_1$ (33)	6.2149(9)	7.6529(11)	6.0859(8)
Zn_2NI	LDA	$Pna2_1$ (33)	6.257 (-1.6)	7.620 (-4.2)	6.097 (-2.5)
	PBE	$Pna2_1$ (33)	6.403 (+0.69)	7.946 (-0.11)	6.278 (+0.40)
	PBEsol	$Pna2_1$ (33)	6.315 (-0.69)	7.738 (-2.7)	6.165 (-1.4)
	Experiment (100 K)[187]	Pnma (62)	6.3590(13)	6.2529(12)	7.9549(16)
ZnO	LDA	$P6_3mc$ (186)	3.195 (-1.63)	3.195 (-1.6)	5.162 (-0.78)
	PBE	$P6_3mc$ (186)	3.286 (+1.16)	3.286 (+1.16)	5.301 (+1.9)
	PBEsol	$P6_3mc$ (186)	3.237 (-0.34)	3.237 (-0.34)	5.222 (+0.37)
	Experiment (4.2 K)[188]	$P6_3mc$ (186)	3.2482	3.2482	5.2028/ 5.2040
	Experiment (296 K)[188]	$P6_3mc$ (186)	3.2500	3.2500	5.2047

those in Zn_2NCl and Zn_2NBr (Figure 19.1(a,b). On closer inspection, we realised that the b and c axes were inverted in Zn_2NI compared to Zn_2NCl and Zn_2NBr, and that adjusting the high-symmetry path accordingly fixed this. Therefore, one must be careful when changing structures through ModeMap to account for deviations from the labelling formalisms in the new structure. We then tried this same trick on the original Pnma (62) structure, and found that this made the phonon dispersion significantly similar to all the $Pna2_1$ dispersions (Figure 19.1(c,d)), showing to a large degree the phononic transport in the two structures is similar. Following on from this, the same transformation was performed on the unit cell of the Pnma (62) structure of Zn_2NI, resulting in view which looks substantially similar to that of the $Pna2_1$ (33) structure shown in Figure 16.1(a). Therefore, one must also be careful of how labelling formalisms may affect perceived interpretations of the data. The most significant difference between the two Zn_2NI structures (besides the imaginary modes) is that in the $Pna2_1$ (33) structure, there is a gap in the upper set of optical modes at around 18 THz which is not present in the Pnma (62) structure. Such gaps can cause a flattening of the bands, and hence a reduction in group velocity and lattice thermal conductivity, and the avoided crossings of the bands in particular (e.g. at around 19.5 THz to the left of the R point) can be evidence of scattering of phonons, such as by rattling atoms, but also of symmetry disallowed transitions.

With respect to the thermodynamic stability of Zn_2NI, the $Pna2_1$ (33) structure is only 1 meV atom^{-1} lower in energy than the Pnma (62) structure. Another interesting thing to note is the plateaux in the modemap shown previously in Figure 18.6(a). Normally, you either get a single well, which indicates that the ‘imaginary’ mode is not real, and does not lead to a more stable structure, or a double well, which indicates the ‘imaginary’ mode is real and leads to a more stable structure. The lowest energy structure was a $Pna2_1$ (33) structure as men-

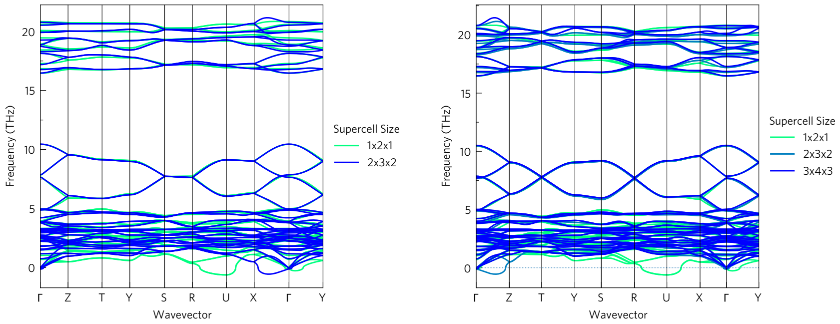

(a) Pna2_1 (33), ModeMap structure

(b) Pna2_1 (33), b and c inverted

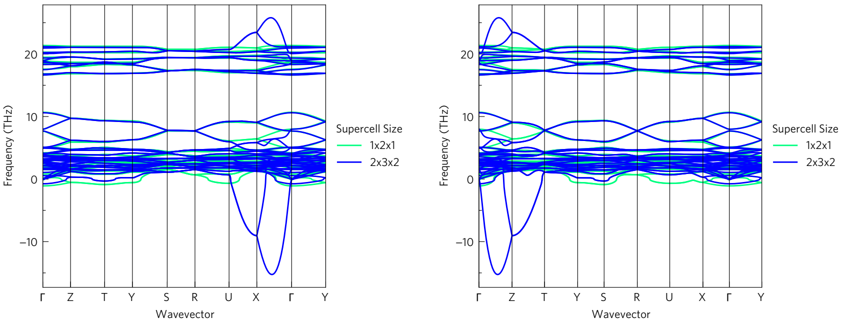

(c) Pnma (62), experimental structure

(d) Pnma (62), b and c inverted

Figure 19.1: Phonon dispersion of Zn2NI in (a, b) the Pnma (62) structure and (c, d) the Pna2_1 (33) structure. The standard orientation for the Pnma (62) structure has c as the long axis, whereas in the Pna2_1 (32) structure, b is the long axis. This means the phonon dispersion of the Pna2_1 (32) structure (c) produced by ModeMap has a different path to that obtained from previous experiments, which followed the conventional orientation for the Pna2_1 (32) structure, and instead shares more with the Pnma (62) dispersion, imaginary modes excepted. Inverting the b and c axis reveals both structures share very similar phonon dispersions to those of the other nitrohalides (b, d), and this inverted path is what is shown in the other figures.

tioned, but the structure at the lowest point in the plateaux is in the Pnma (62) space-group to low precision. This may indicate that there is some kinetic stability to the Pnma (62) structure, and help explain why this was isolated experimentally. Li et al.[189] studied high pressure phases of Zn_2NI, and found that while the Pnma (62) phase is found at 10 atm, at 100,000 atm the $Pna2_1$ phase is formed. A complimentary experiment to theirs and ours would be to measure the phase space with respect to temperature of all three compounds. According to the experiments of Liu et al.[187], the higher symmetry Pnma (62) structure of the iodide is formed at 100 K, and here we report that the lower symmetry Pc (7) structure of the chloride is formed athermally. Therefore, we predict that the larger halide forces a more symmetric structure to form to accommodate it, but temperature effects can cause smaller halide materials to adopt more symmetric structures, and that high pressures can cause larger halide materials to adopt less symmetric structures.

20 CONCLUSION

We have analysed the structures of Zn_2NX (X = Cl, Br, I) using the Phonopy and Modemap codes. To verify our methods, we first applied them to ZnO and found it to be stable with LDA, PBE and PBEsol, with PBEsol providing the most similar structure to near-athermal experiments. Our analysis of Zn_2NBr found that it was also stable in the experimental $Pna2_1$ (33) structure with all three functionals, and that PBEsol was again most accurate, followed closely by PBE. Our PBE and PBEsol calculations in Zn_2NCl, on the other hand, suggest there might be some slight symmetry breaking disorder, resulting in a Pc (7) structure, which may appear as a $Pna2_1$ (33) structure in XRD experiments, or form naturally due to the negligible difference in thermodynamic stability and temperature effects. Likewise, Zn_2NI was experimentally reported in a Pnma (63) structure, but here was found in the same $Pna2_1$ (33) structure as Zn_2NBr. Again, the DFT energy, which here works as a proxy of thermodynamic stability, of the $Pna2_1$ (33) structure is only $1\,\mathrm{meV\,atom^{-1}}$ more negative than the experimental structure, so temperature effects could allow the more symmetric structure to form. We have also shown that when symmetry path formalisms are ignored, phonon transport in all these structures, stable or otherwise, are very similar, although higher symmetry structures tend to have flatter bands and more avoided crossings than lower symmetry structures. As higher symmetry structures are more likely to form at elevated temperatures, and these features reduce the lattice thermal conductivity, this could be a boon for their use as thermoelectrics, although the calculations conducted here will be too simple to account for such effects. This study lays the basis for further study into Zn_2NX, highlighting important structural questions and elucidating the structures that can be more easily studied in future computational work, for example on transparent conductors or thermoelectrics.

Part VII

Thermoelectric Evaluation of Zn_2NX ($X = Cl, Br, I$)

21 METHODOLOGY

The energy cutoff and and k-mesh values for the electronic calculations in this part are shown in Table 21.1. All values were converged to within 10 % of the final value of all the parameters calculated from them. The data for AMSET refers to the interpolated k-mesh used, calculated on top of the DoS mesh listed above it. The supercell sizes and q-meshes are shown in Table 21.2. As each Phono3py run took 27672 calculations, the supercell sizes are based on computational affordability and convergence of the phonon dispersions, but the q-meshes are converged to within 10 % of the lattice thermal conductivity.

During the calculation of the lattice thermal conductivity of Zn_2NBr, a large drift in the third-order force constants was encountered. Force constant drift is when the forces on the atoms do not cancel out, resulting in a net force which would cause the material to move or drift, a clearly unphysical behaviour. Small values of less than $1\,\mathrm{eV\,Å^{-1}}$ are normal as noise, but in this case a drift of $5.59\,\mathrm{eV\,Å^{-1}}$ was observed. This drift can have the effect of underestimating the lattice thermal conductivity, which can be diagnosed by symmetrising the force constants, i.e. asserting zero drift, and recalculating the lattice thermal conductivity. In this case, the unsymmetrised lattice thermal conductivity was $0.251\,\mathrm{W\,m^{-1}\,K^{-1}}$ at 300 K, but the symmetrised one was 2.32 times bigger at $0.586\,\mathrm{W\,m^{-1}\,K^{-1}}$. While this method may be used to diagnose the problem, symmetrised force constants cannot be assumed to be correct, either. In order to correct this, we repeated the force constant calculations, varying the displacement size from the default of 0.03 Å (for reference,

Table 21.1: Plane-wave energy cutoffs (ENCUTs) and k-point grids used used for the primitive cells of each material, converged to within 10 % for the calculated values for each calculation type.

Calculation	Material	ENCUT	k-mesh
DFPT	Zn$_2$NBr	600	$16 \times 14 \times 17$
	Zn$_2$NI	800	$14 \times 12 \times 15$
	ZnO	700	$10 \times 10 \times 6$
Optics	Zn$_2$NBr	300	$6 \times 5 \times 7$
	Zn$_2$NI	300	$6 \times 5 \times 7$
	ZnO	450	$5 \times 5 \times 3$
DoS	Zn$_2$NBr	300	$8 \times 7 \times 9$
	Zn$_2$NI	300	$8 \times 7 \times 9$
	ZnO	450	$7 \times 7 \times 4$
AMSET	Zn$_2$NBr	—	$47 \times 39 \times 49$
	Zn$_2$NI	—	$47 \times 39 \times 49$
	ZnO	—	$83 \times 83 \times 45$

Table 21.2: Supercell sizes used for the second- and third-order force constant calculations and q-point meshes used to calculate the phononic transport properties.

Material	Zn$_2$NBr	Zn$_2$NI	ZnO
Supercell — 2nd	$2 \times 2 \times 3$	$2 \times 2 \times 3$	$5 \times 5 \times 4$
Supercell — 3rd	$3 \times 3 \times 4$	$3 \times 3 \times 4$	$3 \times 3 \times 2$
q-point mesh	$25 \times 21 \times 25$	$25 \times 21 \times 26$	$40 \times 40 \times 21$

the default value for Phonopy is 0.01 Å, and there have been no problems with drift in the second-order force constants in either Phonopy or Phono3py in our experience). Due to the extreme number of calculations this entailed, we also tested the effect of supercell size on the drift by doing the same calculation on the $1 \times 1 \times 2$ supercell, which is far cheaper owing to the smaller supercell size of 32 rather than 192 atoms and only requiring 4,632 calculations per run. We measured two quantities, the drift, and the unsymmetrised:symmetrised ratio, which are shown in Tables 21.3 and 21.4 respectively. We found that the drift in the force constants in the smaller supercell was broadly predictive of the magnitude of the drift in the larger supercell, but the ratio of the lattice thermal conductivities converged to

Table 21.3: Maximum drift in the force constants of Zn$_2$NBr.

Displacement (Å)	Drift (eV Å^{-1})	
	$1 \times 1 \times 2$	$2 \times 2 \times 3$
0.01	10.9	-35.9
0.03	5.23	5.59
0.04	3.43	3.53
0.07	1.66	-0.333

Displacement (Å)	κ_l ($\mathrm{W\,m^{-1}\,K^{-1}}$) $1 \times 1 \times 2$	 $2 \times 2 \times 3$
0.01	1.55	3.60
0.03	1.08	2.33
0.04	1.10	1.45
0.07	1.00	1.04

Table 21.4: Directionally averaged unsymmetrised:symmetrised ratio of the lattice thermal conductivity of Zn_2NBr at 300 K.

unity more quickly in the smaller supercell. From this we propose that calculating the drift in a smaller supercell may be a computationally efficient means of roughly determining the most accurate displacement size in a larger supercell, but it is not a foolproof method. The unsymmetrised:symmetrised ratio, while useful at diagnosing the problem in a large supercell, is not predictive in a smaller supercell. For this work, we have selected a displacement size of 0.07 Å for Zn_2NBr, and have left Zn_2NI and ZnO at 0.03 Å, as they had no drift problems.

22 RESULTS

Electronic Transport

The electronic band structures and DoSs are shown in Figures 22.1 and 22.2. Like their parent ZnO, the CBMs of Zn_2NX are mostly comprised of Zn s states, followed by N (O in ZnO) s states. Unlike ZnO, they have Zn d states and halide states which also contribute a small amount to the CBM. This has no immediately clear effect on the CBM itself, but other Zn states do. Zn_2NX (X = Cl, Br, I) have large, optically transparent bandgaps of 3.29 eV, 3.29 eV and 3.11 eV respectively, slightly lower than ZnO's 3.4 eV, in agreement with the experiment of Liu et al.[187] which isolated colourless crystals. In Zn_2NX, however, as you go to heavier halides, high-energy Zn s and p states lower in energy, which are located within 3.1 eV of the CBM, in contrast to ZnO (Table 22.1). This means when they are doped, electrons at the CBM can absorb visible light to excite to the next band, rendering Zn_2NX coloured when doped enough to be effective thermoelectrics (or for any other electrical application). The wide gap between CBM and CBM+1 would likely render Zn_2NCl a reddish colour, depending on dopant concentration, but down the halide group they would change colour as the gap shortens. Even in the iodide, the gap remains much too large for CBM+1 to have an effect on the electronic transport properties. In the VBM, the X p states rise in energy down the group, piling up at the VBM along the Z direction, causing less dispersion, but at the same time the dispersion along the Y direction increases. Should Zn_2NX be p-type, this would be

Table 22.1: Hybrid HSE indirect and direct bandgaps and effective masses of electrons at the CBM and holes at the VBM of ZnO (37.5 % HF exchange) and Zn_2NX (X = Cl, Br, I, 25 % HF exchange), given in eV. Effective masses are calculated using parabolic band fitting in sumo.[141]

Material	Zn_2NCl	Zn_2NBr	Zn_2NI (63)	Zn_2NI (33)	ZnO
E_g^{ind} (eV)	3.28	—	3.24	3.11	—
E_g^{dir} (eV)	3.29 (Γ)	3.29 (Γ)	3.30 (Γ–X)	3.11 (Γ)	3.43 (Γ)
$E^{\text{dir}}_{\text{CBM}\rightarrow\text{CBM+1}}$ (eV)	2.14	1.74	0.692	1.03	4.86
m^*_{e} (m_{e})	0.243	0.215	0.202	0.186	0.257
$m^*_{\text{h,x}}$ (m_{e})	0.738	1.15	1.14	1.00	—
$m^*_{\text{h,y}}$ (m_{e})	0.738	0.666	—	0.303	2.36
$m^*_{\text{h,z}}$ (m_{e})	0.747	3.30	—	29.6	2.86

a boon to the thermoelectric properties, as the high density of states would enhance the Seebeck coefficient while the dispersion along the Y direction would give a high electrical conductivity, but due to their similarity to ZnO, this seems unlikely. Nevertheless, computing the band alignment of these materials will be necessary to resolve this.

They also have highly disperse conduction bands around the minima, much like ZnO. Using the parabolic band fitting method in sumo, the effective masses of the electrons at the conduction band minimum was calculated, and found to be 0.243 m_e, 0.215 m_e and 0.202 m_e respectively. These are lighter than even ZnO, an established conducting oxide, which has an electron effective mass of 0.259 m_e. This suggests that they may be more conductive than ZnO, although this also depends on the scattering rates.

The remaining properties were calculated only for Zn_2NBr and the $Pna2_1$ (33) form of Zn_2NI (and ZnO). To complete the picture of the electrical conductivity, we will first examine the electronic scattering rates. These are shown in Figure 22.3. Comparing Zn_2NBr in (a) and ZnO in (c), the overall scattering rates of ZnO are 1.5–2 times higher than for Zn_2NBr, and Zn_2NI's is lower again. There are several important factors in this. ZnO has a large piezoelectric coefficient in the z direction of

Figure 22.1: Electronic dispersions of (a) Zn_2NCl and (b) Zn_2NBr. The valence bands are blue and the conduction bands are orange, with the VBM normalised to 0 eV. The orbital-decomposed DoS is on the right of each dispersion. The k-point path is determined by the Bradley–Cracknell formalism.[142]

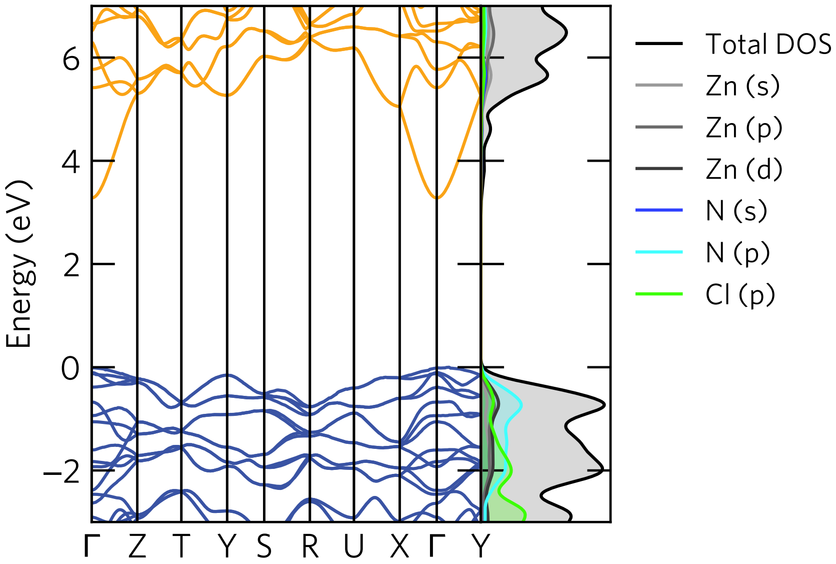

(a) Zn_2NCl

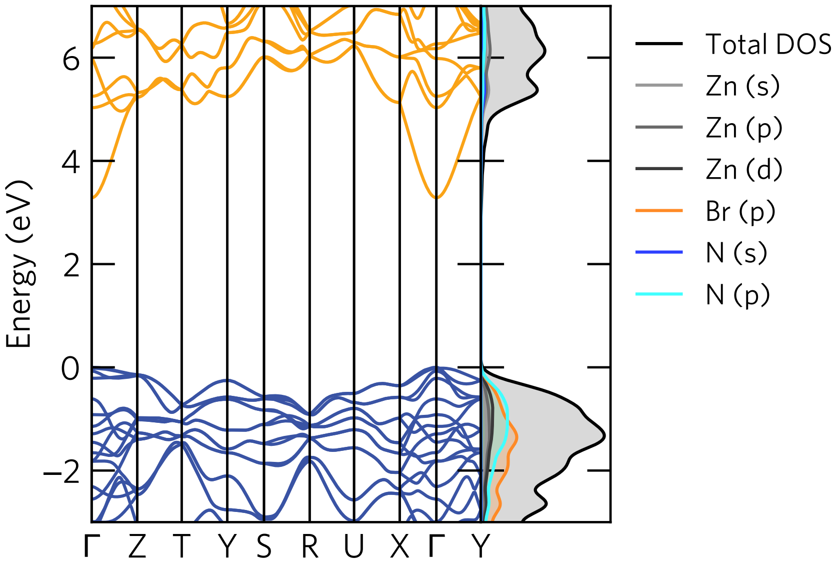

(b) Zn_2NBr

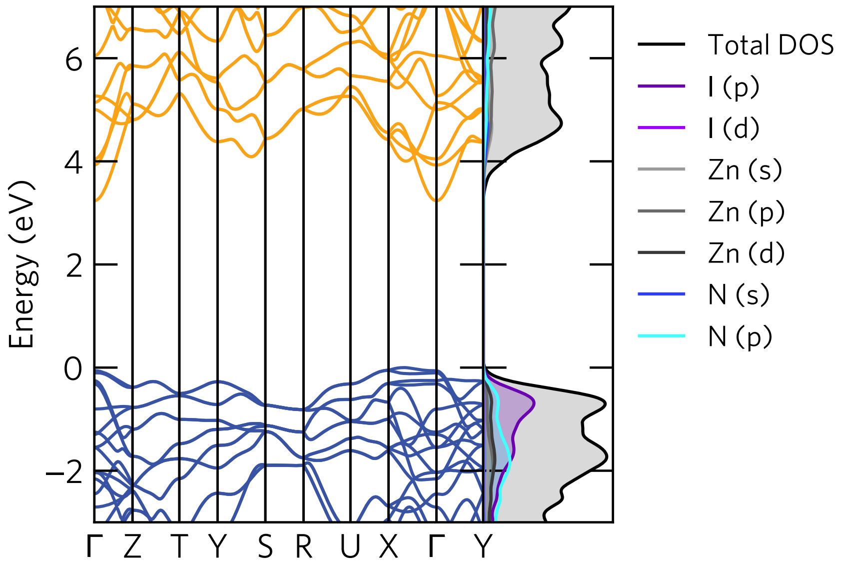

(a) Zn$_2$NI Pnma (63)

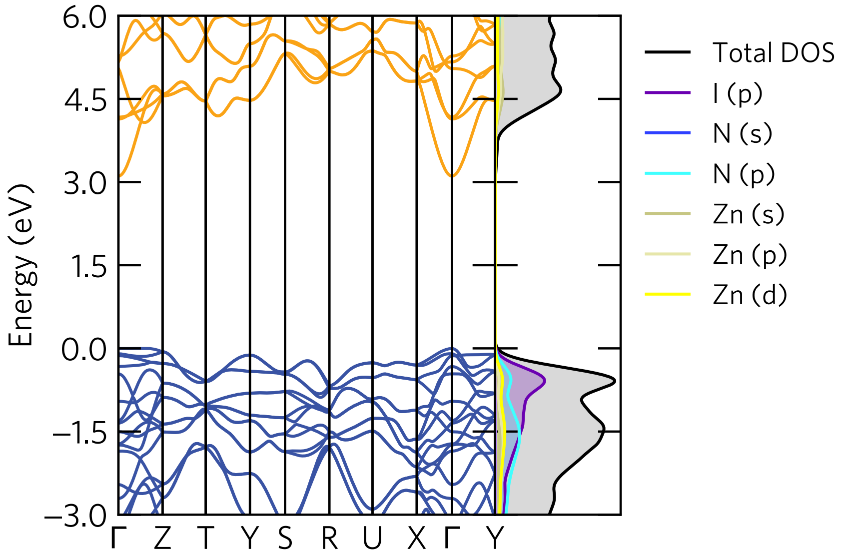

(b) Zn$_2$NI Pna2$_1$ (33)

Figure 22.2: Electronic dispersions of Zn$_2$NI in the (a) Pnma (63, experimentally observed) and (b) Pna2$_1$ (33, computationally stable) spacegroup. The valence bands are blue and the conduction bands are orange, with the VBM normalised to 0 eV. The orbital-decomposed DoS is on the right of each dispersion. The k-point path is determined by the Bradley–Cracknell formalism.[142]

$2.07\,\mathrm{C\,m^{-2}}$, however Zn_2NX, with their more complex structure and more covalent bonds owing to the halide's lower electronegativity, have coefficients of $-0.21\,\mathrm{C\,m^{-2}}$ and $-0.44\,\mathrm{C\,m^{-2}}$. This more or less eliminates one of the main scattering mechanisms in ZnO. Under all but the highest carrier concentrations, polar-optical phonon scattering is the dominant scattering mechanism in all the compounds, which is approximated as being proportional to the root of the dipole-weighted optical phonon frequency at the Γ point in AMSET. This factor is much lower in the nitrohalides (6.54 THz and 5.63 THz) than in the oxide (11.5 THz), owing to the heavier atoms reducing the frequency of the phonons.[190] Finally, there is also the dielectric constant, which is higher in Zn_2NX (10–16 ε_0 and 10–19 ε_0) than in ZnO (8.0–8.9 ε_0). This is due to the greater number of electrons in the halides, especially in the iodide, which screen the ionised impurity, polar-optical phonon and piezoelectric scattering, reducing the scattering further. Together these factors and the more disperse conduction band edges will make Zn_2NX highly conductive, increasingly so down the group.

The electronic transport properties are shown in Figure 22.4. The high scattering in ZnO causes the CRTA to significantly overestimate the conductivity, especially at high temperatures, where there is particularly strong polar-optical phonon and piezoelectric scattering; and a high carrier concentrations, where there is particularly strong ionised impurity scattering. This is not true for Zn_2NBr, which the CRTA only *normally* overestimates the conductivity, especially at high carrier concentrations due to high ionised impurity scattering. The trend continues in Zn_2NI, where the CRTA is as likely to underestimate the scattering as overestimate it, due to the factors listed previously. By considering both the CRTA and MRTA, we can ascribe differences in conductivity to the band structure and the scattering. While the CRTA conductivity does increase in the order ZnO < Zn_2NBr < Zn_2NI, the difference is slight, all within about 30 % of each other. In contrast, the MRTA conductivity

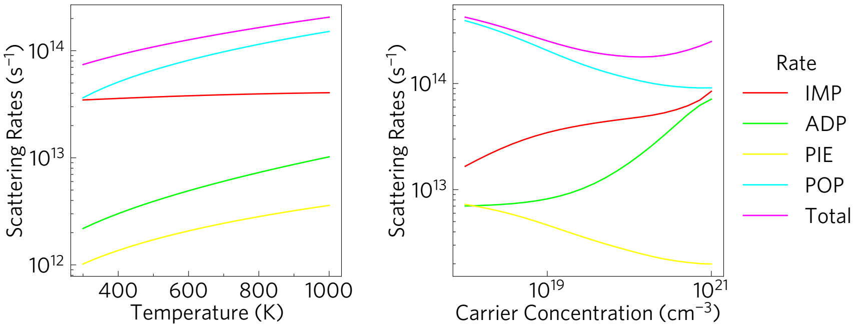

(a) Zn_2NBr

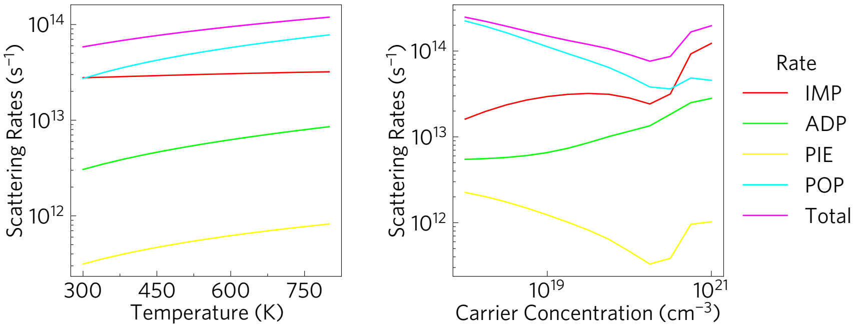

(b) Zn_2NI

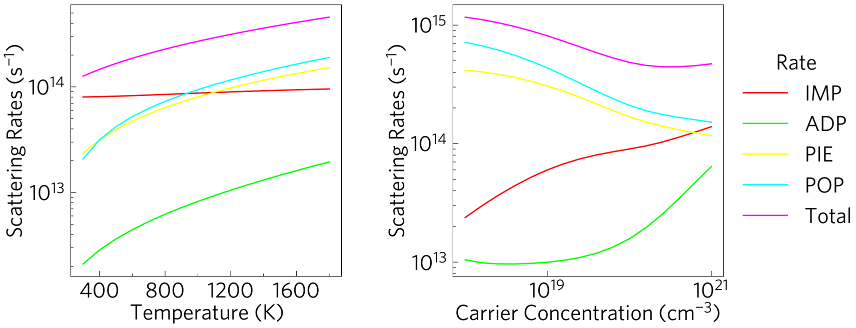

(c) ZnO

Figure 22.3: Scattering rates broken down by mechanism for (a) Zn_2NBr, (b) Zn_2NI and (c) ZnO under optimal ZT conditions.

for Zn_2NI is as much as three times higher than ZnO, showing that while both factors work together, the scattering is far more important. These trends are much the same for the electronic contribution to the thermal conductivity, thanks to the Wiedemann–Franz law. The Seebeck coefficient is not especially high for any of the materials, due to the disperse, single-banded CBM, and is generally the same for both the CRTA and MRTA, as it is not strongly affected by electron scattering. The exception is at high carrier concentrations in Zn_2NI. In the CRTA, the Seebeck coefficient seems to "avoid" $0\,\mathrm{S\,cm^{-1}}$, with the values for 1×10^{20}–$1 \times 10^{21}\,\mathrm{carriers\,cm^{-3}}$ remaining very similar. The MRTA, in contrast blows right past $0\,\mathrm{S\,cm^{-1}}$ and becomes p-type. This peculiar behaviour is most likely and artefact of the calculation and could not be reproduced in experiment, however it does have real precedent in these types of calculations. In narrow-bandgap systems, high temperatures can excite charge carriers across the band gap in both directions, and if there are few charge carriers in the system (i.e the darker lines in these graphs), these can be overwhelmed, leading to an ambipolar doping regime. This causes an increase in conductivity as there are many more charge carriers, but a massive reduction in Seebeck, as the electrons and holes diffuse in the same direction, cancelling each other out. The overall Seebeck is then a function of the number of holes and electrons and the relative Seebeck coefficients of the CBM and VBM. In materials with a high Seebeck coefficient in the opposite band (i.e. the valence band for an n-type material like those studied here), the overall Seebeck coefficient can switch signs. While Zn_2NI has a high density of states at the valence band edge, giving a large p-type Seebeck coefficient, this does not explain the cause of the behaviour, but it does give some background as to why this artefact manifested in this way.

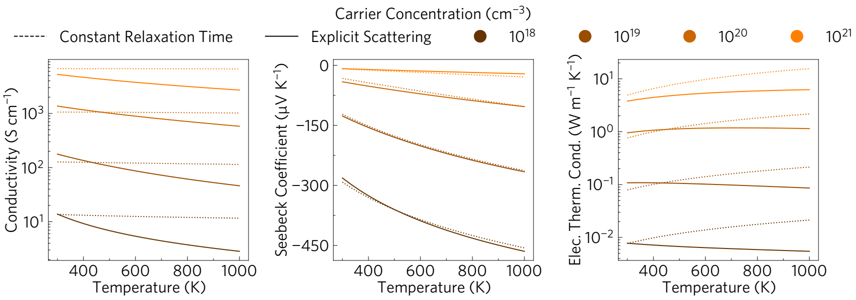

(a) Zn_2NBr

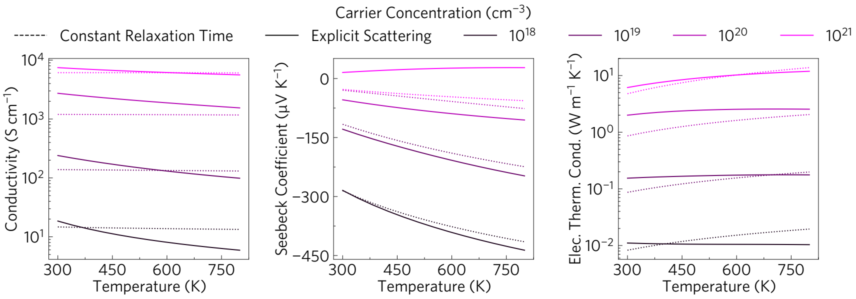

(b) Zn_2NI

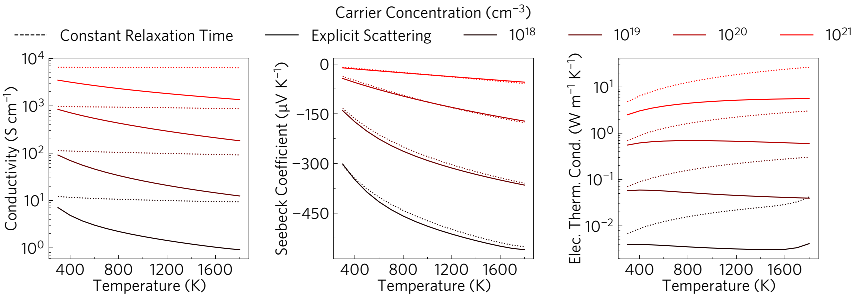

(c) ZnO

Figure 22.4: Electronic transport properties for (a) Zn_2NBr, (b) Zn_2NI and (c) ZnO under various temperatures and carrier concentrations. The dashed lines show the CRTA data, while the solid lines show the MRTA data.

Figure 22.5: Phonon dispersions and DoSs of (a) Zn$_2$NBr, (b) Zn$_2$NI and (c) ZnO, showing the elemental contributions by frequency.

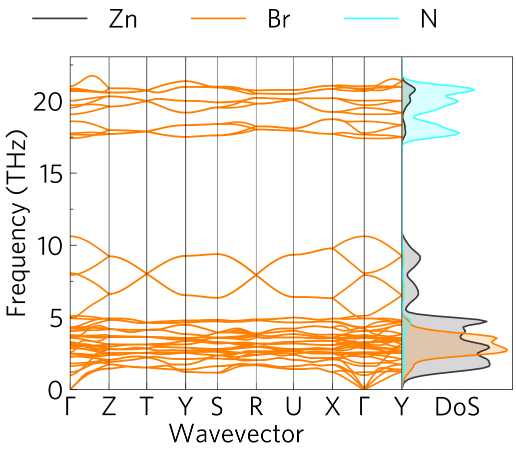

(a) Zn$_2$NBr

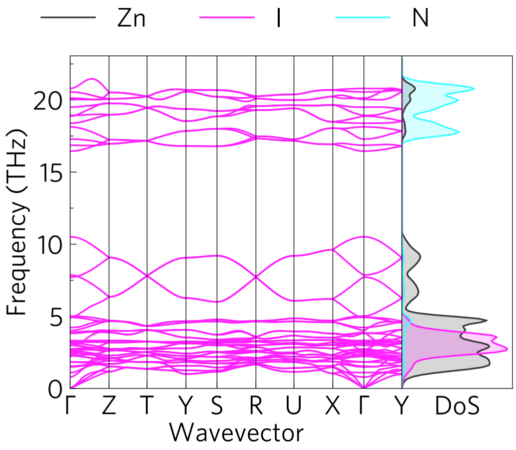

(b) Zn$_2$NI

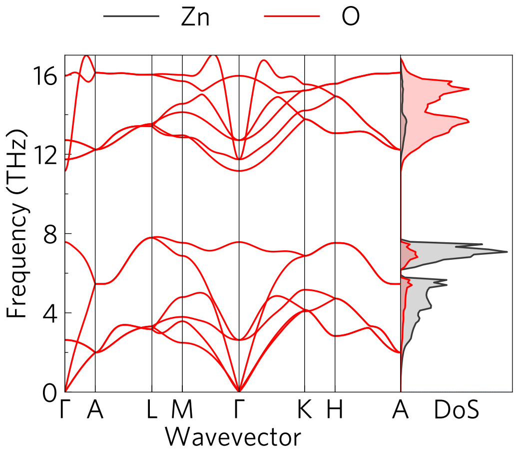

(c) ZnO

Thermal Transport

Compared to ZnO, the phonon dispersions of Zn_2NX are clearly much flatter, indicating low group velocities, but they also share several similarities. For example, low frequency Zn-dominated modes are split from high-frequency N/O-dominated modes by a bandgap (Figure 22.5). This breakdown differs once you consider the halide, which is exclusively found in the low-frequency modes in a relatively small frequency range. In ZnO a large portion of the Zn character can be found in modes around 8 THz, but there is also a significant portion at lower frequencies, whereas in Zn_2NX the vast majority of the Zn character is in the modes below 6 THz, in the same region as the halide. The opposite it true of the N, which is almost exclusively found above the bandgap, in contrast to the O in ZnO, which while found predominantly above the band gap, has a clear contribution to lower frequency modes. If you zoom in on the low frequency modes, you can see a large number of avoided crossings of the modes, some of which are highlighted in Figure 22.6.

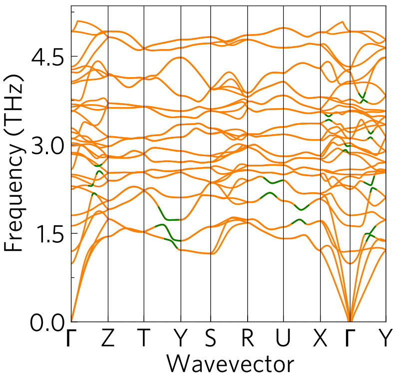

Figure 22.6: A close up of the phonon dispersion of Zn_2NBr below 5 THz, with a non-exhaustive selection of avoided crossings highlighted in green.

Avoided crossings can be a sign of symmetry-forbidden transitions between modes, but we think the high density of avoided crossings specifically centred around the halide ion is evidence of rattling of these atoms. Rattling is a process whereby normally heavy atoms vibrate relatively independently of other atoms, archetypally in cage structures such as clathrates.[191] These result in localised, flat bands, and typically produce avoided crossings in the surrounding modes, and act as strong scattering centres. To corroborate this, we can use the data from Phono3py. Figure 22.7 shows four things against frequency on the x-axis on each set of axes:

- In pink there is a "waterfall plot" of mean free paths against frequency, i.e. a plot of mean free path for each band/q-point combination. The scale is shown on the left.
- Projected on the colour axis of the waterfall plot is the lattice thermal conductivity of each band/q-point pair. The

scale is on the colourbar to the right.
- The black line is the cumulative lattice thermal conductivity. The scale is linear and in percent.
- The shaded regions are the atom-decomposed DoSs. The scale is linear and in arbitrary units and the key is on the right.

One of the key differences between the waterfalls of ZnO and Zn$_2$NX is the dip in mean free paths, and correspondingly the lattice thermal conductivity, around 5 THz. The usual pattern is that seen in ZnO, where there is a fairly continuous decrease, which can be broken up with lower mean free path modes around band gaps. This is caused by a fairly constant group velocity, v_g (except for at low frequency where it is higher), and a decreasing lifetime, τ, as mean free path, $\Lambda = v_g\tau$. This is clearly different in Zn$_2$NX, where the mean free paths bounce back, indicating an unusual decrease. Besides the acoustic modes, which are always very conductive due to their high group velocities and low frequencies, which make finding energy-conserving scattering processes difficult, there is an immediate levelling-off of the cumulative lattice thermal conductivity until about 5 THz. Comparing this to the DoSs, this is where the halide modes end entirely, and the Zn-dominated modes begin. We think the correlation of these factors is strong evidence of the halides playing an important role in disrupting thermal transport, probably by rattling. On the left of Figure 22.8, we show that the actual lattice thermal conductivities of Zn$_2$NX are below $2\,\mathrm{W\,m^{-1}\,K^{-1}}$ above 200 K, a dramatic decrease relative to ZnO, whose lattice thermal conductivity does not drop below $10\,\mathrm{W\,m^{-1}\,K^{-1}}$ even at twice the decomposition temperatures of Zn$_2$NX, a reduction factor of 35–53 times over the stability region of Zn$_2$NBr. This will be a major boon to the ZT.

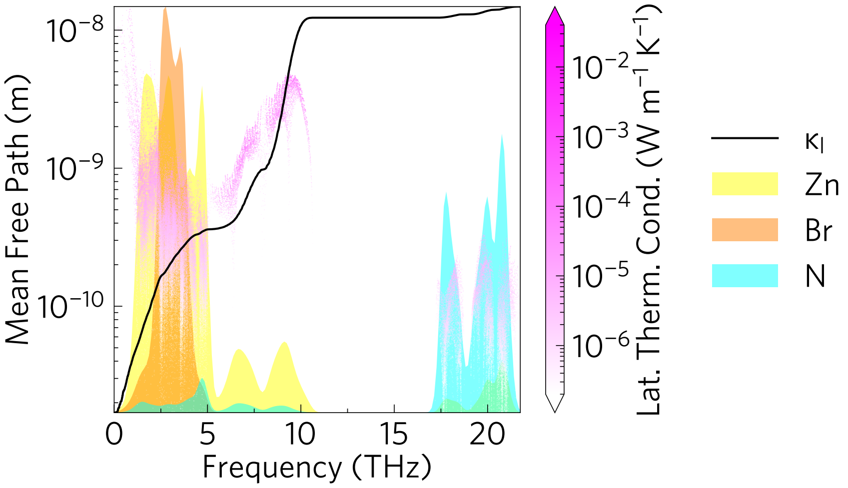

(a) Zn$_2$NBr

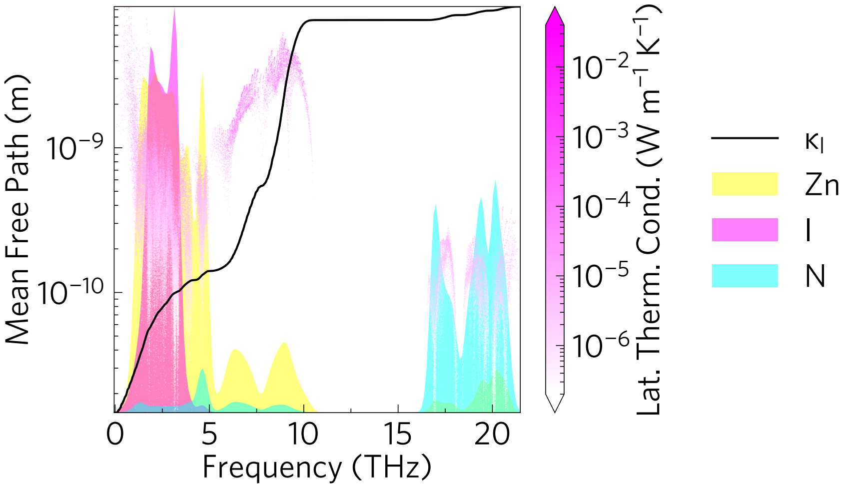

(b) Zn$_2$NI

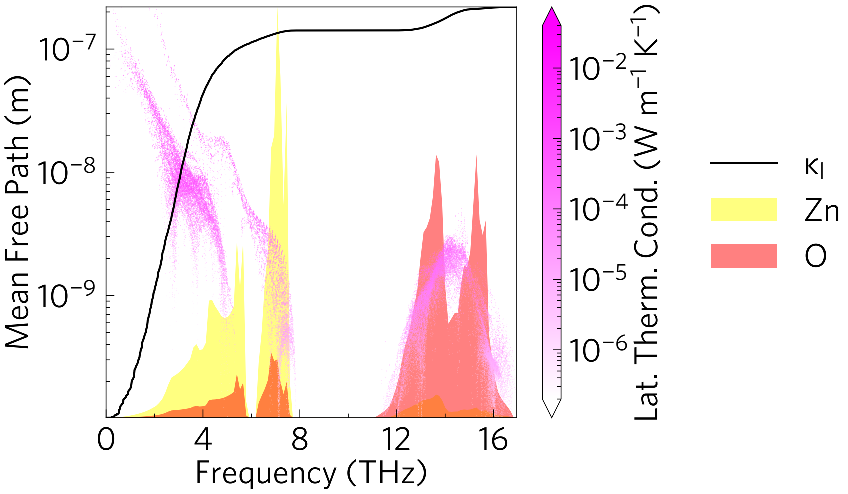

(c) ZnO

Figure 22.7: Waterfall plots of mean free path with lattice thermal conductivity projected, atom-decomposed DoSs and cumulative lattice thermal conductivity against frequency of (a) Zn$_2$NBr, (b) Zn$_2$NI and (c) ZnO. The logarithmic y-axis is shown for the mean free paths, while the DoSs and cumulative lattice thermal conductivity plots are shown on linear scales of arbitrary units and percent respectively.

Figure 22.8: Lattice thermal conductivities on the left and ZTs on the right split by direction against temperature of (a) Zn_2NBr, (b) Zn_2NI and (c) ZnO.

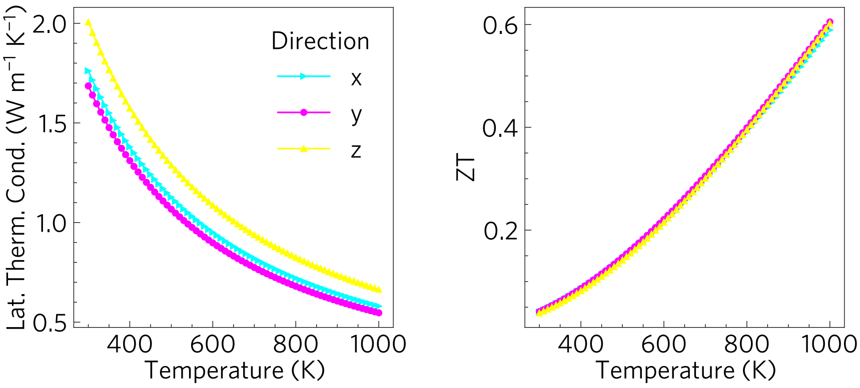

(a) Zn_2NBr

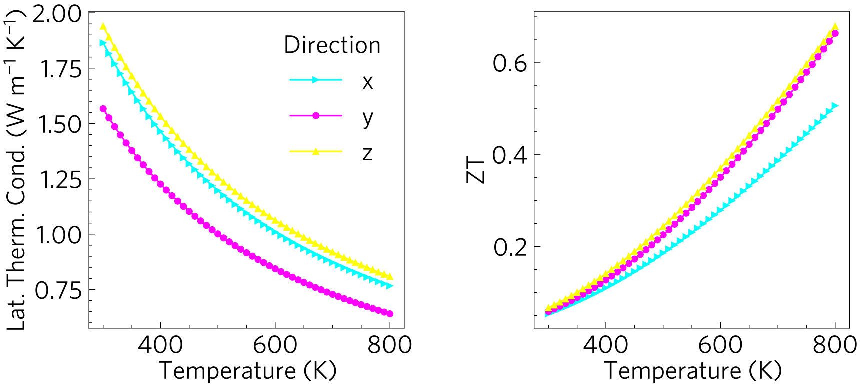

(b) Zn_2NI

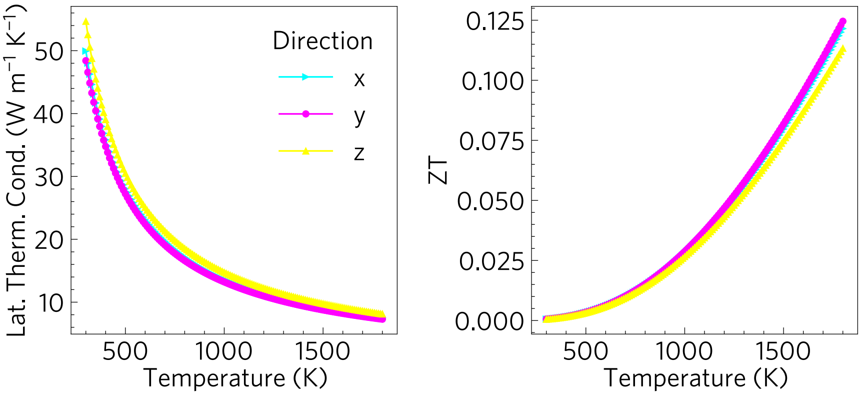

(c) ZnO

ZT

Combining the electronic and phononic transport properties, we come to the *ZT*. The right of Figure 22.8 and Figure 22.9 show that greatly reduced lattice thermal conductivity has enhanced the *ZT* by around five times, despite the reduced Seebeck coefficient and thermal stability. Comparing them between 300–800 K, the range between room temperature and slightly below the lowest decomposition temperature, the lattice thermal conductivity of Zn_2NX varies much more slowly with temperature. This results in a correspondingly slower variation in *ZT*, which varies by a factor of 10 for Zn_2NX but a factor of 20 for ZnO, leading to higher average *ZT*s over that temperature range for Zn_2NBr and Zn_2NI of 0.19 and 0.29, which are 47 % of their maxima, compared to 0.0053 for ZnO, which is 38 % of its maxima, making Zn_2NX potentially even more useful for real devices. In addition, the carrier concentration required to maximise *ZT* is reduced by five times, from 1.59×10^{20} carriers cm^{-3} to around 3×10^{19} carriers cm^{-3}. This will make it easier to dope Zn_2NX to the carrier concentrations required to achieve the maximum *ZT*. It also has the effect (although cause and effect are particularly intertwined here) of making the Seebeck higher in Zn_2NX higher under optimal-*ZT* conditions, despite being lower when temperature and carrier concentrations are the same. Zn_2NBr has the highest Seebeck coefficient of 188 µV K^{-1}, 50 % more than ZnO, but less than half the electrical conductivity, which balances out to give a similar power factor of 0.0524 W m^{-1} K^{-2} (recall that $PF = \alpha^2\sigma$). Combined with a much reduced thermal conductivity results in a large increase in *ZT*. Zn_2NI, on the other hand, has a slightly higher optimal carrier concentration and 10 % lower Seebeck than Zn_2NBr, and an electrical conductivity even higher than ZnO. This combines to make a power factor almost twice that of ZnO and Zn_2NBr, at 0.112 W m^{-1} K^{-2}. Although the thermal conductivity of Zn_2NX are very similar, the lower thermal

Figure 22.9: Directionally averaged ZTs against temperature and carrier concentration of (a) Zn$_2$NBr, (b) Zn$_2$NI and (c) ZnO.

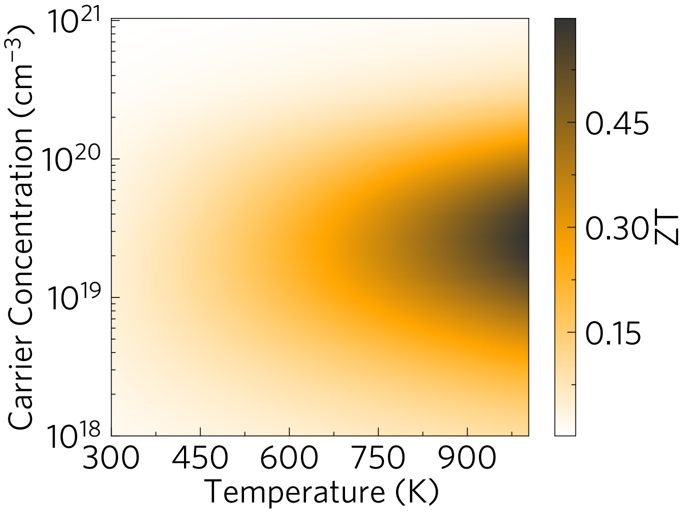

(a) Zn$_2$NBr

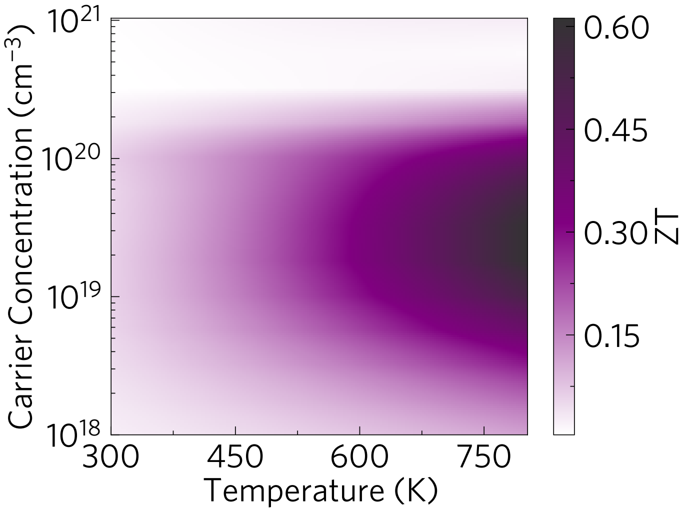

(b) Zn$_2$NI

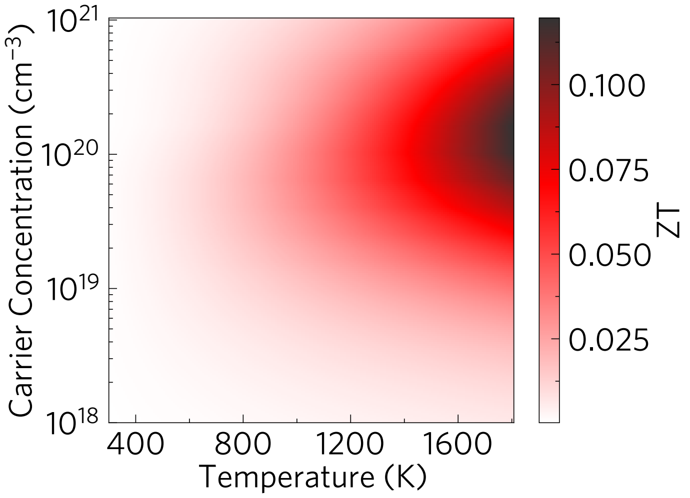

(c) ZnO

Table 22.2: Directionally averaged transport properties of each material under optimal-ZT conditions. Shown are the temperature, carrier concentration, electrical conductivity, Seebeck coefficient, power factor, electronic and lattice contributions to the thermal conductivity and their total and ZT.

	Zn_2NBr	Zn_2NI	ZnO
T (K)	1000	800	1800
n (carriers cm^{-3})	2.68×10^{19}	3.16×10^{19}	3.59×10^{20}
σ ($S\,cm^{-1}$)	148	388	337
α ($\mu V\,K^{-1}$)	-188	-169	-128
PF ($W\,m^{-1}\,K^{-2}$)	0.0524	0.112	0.0552
κ_e ($W\,m^{-1}\,K^{-1}$)	0.277	0.709	1.04
κ_l ($W\,m^{-1}\,K^{-1}$)	0.597	0.739	7.64
κ ($W\,m^{-1}\,K^{-1}$)	0.874	1.448	8.68
ZT	0.599	0.612	0.120

stability of Zn_2NI means that the lattice thermal conductivity is slightly higher, at $0.739\,W\,m^{-1}\,K^{-1}$ compared to Zn_2NBr's $0.597\,W\,m^{-1}\,K^{-1}$, and the higher carrier concentration causes a higher electronic component of the thermal conductivity, at $0.709\,W\,m^{-1}\,K^{-1}$ rather than $0.277\,W\,m^{-1}\,K^{-1}$. This results in a 66 % higher total thermal conductivity, but the maximum directionally averaged ZT is nevertheless slightly greater, at 0.612 as opposed to 0.599 in Zn_2NBr. Once you consider directionality, Zn_2NI has easily the highest ZT of 0.672 in the z direction. Comparing all three materials isothermally at 800 K also shows Zn_2NI to be the superior thermoelectric, as the reduced values Zn_2NBr and ZnO are 0.376 and 0.014 respectively, although this does bring the optimal doping carrier concentration for ZnO to the same range as for Zn_2NX, as shown in Table 22.3.

Table 22.3: Directionally averaged transport properties of each material under optimal-ZT carrier concentrations at 800 K. Shown are the temperature, carrier concentration, electrical conductivity, Seebeck coefficient, power factor, electronic and lattice contributions to the thermal conductivity and their total and ZT.

	Zn$_2$NBr	Zn$_2$NI	ZnO
T (K)	800	800	800
n (carriers cm^{-3})	3.73×10^{19}	3.16×10^{19}	1.58×10^{19}
σ (S cm^{-1})	270	388	58.4
α (µV K^{-1})	-143	-169	-226
PF (W m^{-1} K^{-2})	0.0552	0.112	0.0299
κ_e (W m^{-1} K^{-1})	0.429	0.709	0.0901
κ_l (W m^{-1} K^{-1})	0.742	0.739	17.4
κ (W m^{-1} K^{-1})	1.171	1.448	17.5
ZT	0.376	0.612	0.014

Table 22.4: ZT of each material in each direction and averaged over direction.

ZT (n (cm^{-3}))	Zn$_2$NBr	Zn$_2$NI	ZnO
x	0.589 (2.68×10^{19})	0.528 (1.78×10^{19})	0.122 (1.59×10^{20})
y	0.605 (2.68×10^{19})	0.644 (3.16×10^{19})	0.125 (1.59×10^{20})
z	0.603 (2.68×10^{19})	0.672 (3.16×10^{19})	0.113 (1.59×10^{20})
Average	0.599 (2.68×10^{19})	0.612 (3.16×10^{19})	0.120 (1.59×10^{20})

23 DISCUSSION

The experimental values of ZT for ZnO far exceed those calculated here, at up to 0.65.[94] This is after years of experimentation, finding methods of enhancing the thermoelectric properties, which Zn_2NX have not been subject to. ZnO is often studied as Al-doped ZnO (AZO),[92] but in the record-holding study, it is dually doped with Ga and Al, which is complex and out of the scope of this research. The Ga doping resulted in an impurity phase forming, which would have caused phonon (and electron) scattering. Here, we have not attempted to replicate this, but have instead simulated nanostructuring to 20 nm in ZnO to find out how anion substitution compares to nanostructuring as a means to enhance the thermoelectric performance of ZnO. In ZnO, the lattice thermal conductivity reduces by 42 % at 1,800 K, from $7.64\,\mathrm{W\,m^{-1}\,K^{-1}}$ to $4.41\,\mathrm{W\,m^{-1}\,K^{-1}}$, and the power factor reduces from $0.0542\,\mathrm{W\,m^{-1}\,K^{-2}}$ to $0.0501\,\mathrm{W\,m^{-1}\,K^{-2}}$ with $1 \times 10^{20}\,\mathrm{carriers\,cm^{-3}}$, a reduction of 8 %. This gives a nanostructured ZT of 0.182. This is far less than the ZTs we have seen from Zn_2NX, suggesting this is indeed an effective alternative to nanostructuring. We can also simulate nanostructuring in Zn_2NX. In Zn_2NBr, relatively low intrinsic scattering causes a larger effect of mean free path scattering, resulting a 19 % reduction in conductivity from $148\,\mathrm{S\,cm^{-1}}$ to $120\,\mathrm{S\,cm^{-1}}$ leading to a similar reduction in power factor from $0.0524\,\mathrm{W\,m^{-1}\,K^{-2}}$ to $0.0434\,\mathrm{W\,m^{-1}\,K^{-2}}$. The relatively high phonon scattering on the other hand causes the opposite effect, with a 15 % reduction from $0.597\,\mathrm{W\,m^{-1}\,K^{-1}}$ to $0.507\,\mathrm{W\,m^{-1}\,K^{-1}}$. Overall, this results in a very slight reduction in ZT from 0.599 to 0.595. In Zn_2NI,

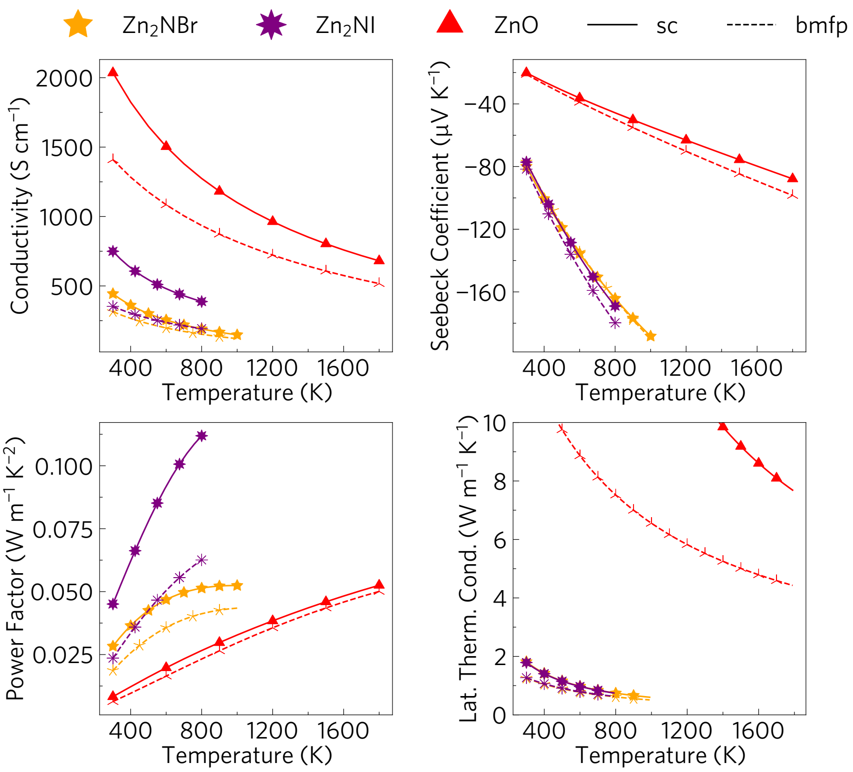

Figure 23.1: Comparison of single crystal (solid lines) and nanostructured (dashed lines) electrical conductivity, Seebeck coefficient, power factor and lattice thermal conductivity against temperature at optimal carrier concentration of Zn$_2$NBr (five-pointed shapes), Zn$_2$NI (eight-pointed shapes) and ZnO (three-pointed shapes).

the effect is greater, with a reduction of conductivity of 50 % from 388 S cm^{-1} to 193 S cm^{-1}, in large part due to the reduction in optimal carrier concentration from 3.16×10^{19} carriers cm^{-3} to 2.15 carriers cm^{-3} which is not seen in the bromide. This carrier concentration reduction also causes the Seebeck coefficient to increase from 169 µV K^{-1} to 180 µV K^{-1}, which overall leads to a power factor reduction of 44 % from 0.112 W m^{-1} K^{-2} to 0.626 W m^{-1} K^{-2}. The reduction in lattice thermal conductivity was also 15 %, from 0.739 W m^{-1} K^{-1} to 0.626 W m^{-1} K^{-1} owing to the lower temperature of 800 K rather than 1,000 K. This leads to a 14 % reduction in ZT from 0.615 to 0.526.

We have seen that the mixed anion nature with the heavy, electron-rich halide ions cause the favourable electrical and thermal conductivities of Zn$_2$NX, primarily through reduced electronic scattering and increased phononic scattering when compared to ZnO. The electron-rich I also accounts for the increased dielectric constant and therefore reduced electronic scattering of Zn$_2$NI compared to Zn$_2$NBr as discussed in the previous chapter.

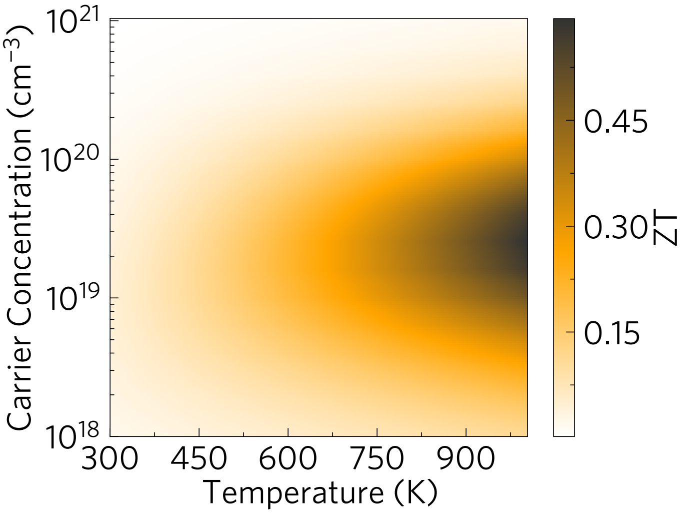

(a) Zn$_2$NBr

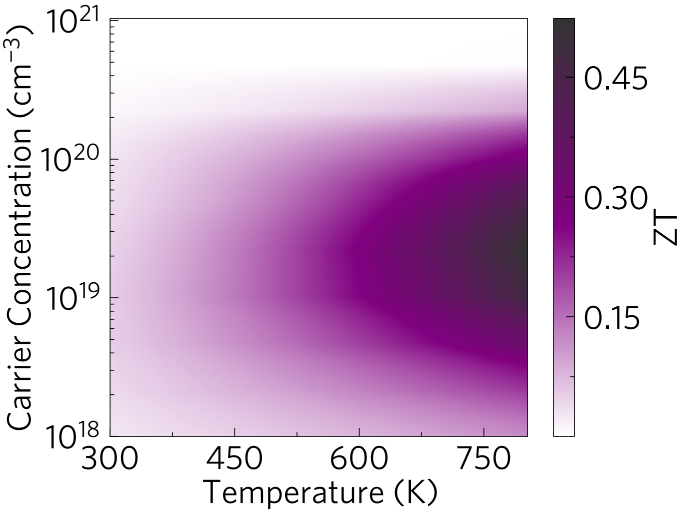

(b) Zn$_2$NI

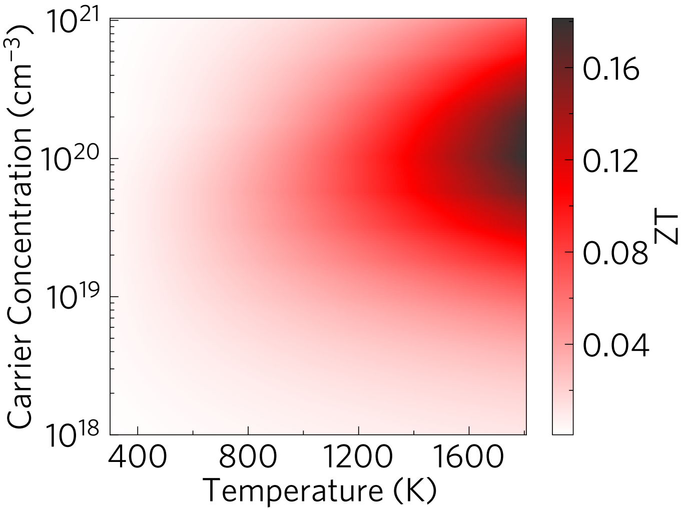

(c) ZnO

Figure 23.2: Nanostructured ZTs against temperature and carrier concentration of (a) Zn$_2$NBr, (b) Zn$_2$NI and (c) ZnO.

Table 23.1: Bond lengths in Zn$_2$NX. The corresponding bonds are shown in Figure 23.3(b). The direction refers to the directions the bonds point in, roughly in order of which is the predominant direction. A single letter does not imply the bond points directly in that direction.

Bond length (Å)	Zn$_2$NBr	Zn$_2$NI	Difference	Direction
Zn–N	1.906	1.918	0.012	ab
	1.896	1.909	0.013	a
	1.877	1.887	0.010	cb
	1.880	1.890	0.010	cb
Zn–X	2.833	3.108	0.275	bc
	2.775	2.993	0.218	ac
	2.652	2.872	0.220	ba
	2.751	2.982	0.231	c

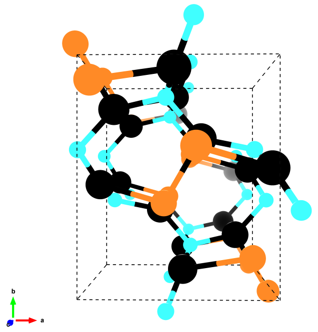

(a) Structure

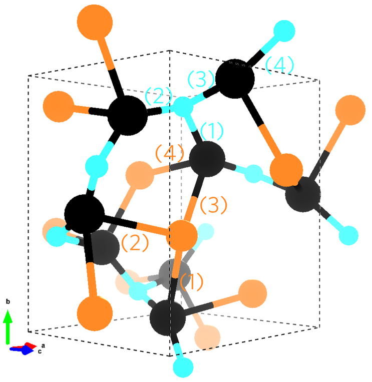

(b) Bonds

Figure 23.3: The structure of Zn$_2$NX (a) shown previously for reference and (b) rotated 50° right about the b axis, with labels corresponding the bond order in Table 23.1. Zn−Br bonds are shown in orange and Zn−N bonds are blue. Drawn predominantly with Vesta.[164]

Another factor in the difference between Zn$_2$NX is the crystal structure. The most obvious distinction is the size of the halide ion, who's radius in crystals is around 182 pm for Br and 206 pm for I,[192] a difference of 24 pm. The bond lengths of of most of the Zn−X bonds increase by 22–23 pm (Table 23.1), in good agreement with this value, but the first bond (c.f. Figure 23.3) increases by 27.5 pm, or almost 15 % larger than the difference in ionic radii. Previously, we observed a lowering of the energy of the predominantly Zn s-state CBM+1, and raising of the halide p-states in the valence band, for which we have two possible explanations. One is that the halide p-states rise in energy down the group, however, if these are lower than the Zn s-states they will create a greater energy overlap and cause the orbitals to separate more in energy, and if they were higher than the Zn s-states the conduction band would have more halide character and the valence band more Zn character. We therefore suggest that the lengthening of the Zn−X bond reduces the spacial overlap of the orbitals, which is particularly strong due to the short-range character of the Zn s-orbitals, causing the narrowing of the separation between these orbitals. This also helps to explain the lower decomposition temperature of the iodide.

Zn$_2$NX have high n-type electrical conductivity and low lattice thermal conductivity, so the limiting factor (besides the low decomposition temperature) is the low Seebeck coefficient. As previously mentioned, a high Seebeck coefficient requires high charge carrier effective mass and low carrier concentrations, so is often difficult to optimise alongside the electrical conductivity, which requires the opposite, but there are ways around this. Multiple bands at the band edge can enable both quantities to be optimised.[58] If the band edge has a degeneracy of two, this doubles the carrier concentration without affecting the conductivity, and if there is a combination of a flat and disperse band, this gives a combination of high and low effective mass charge carriers to give a high Seebeck coefficient and electrical conductivity. The degeneracy does not have to be at the same k-point, and off-Γ edges have added degeneracy depending on the symmetry of the structure and k-point, where off-high-symmetry point band edges provide the greatest benefit, exemplified by Mg_2Pn_3.[60] The valence band of Zn_2NX demonstrates several of these characteristics nicely, with band degeneracy in the VBM at the Γ point in Zn_2NBr and a flat VBM stretching most the way from Γ to Z in Zn_2NI, whilst still having disperse bands in the y direction, as demonstrated by the effective masses (Table 22.1). Unfortunately these are likely to be n-type materials, although we do not yet have the data to be sure about that, but it could be possible to induce these effects in the conduction band. The marked reduction in the energy of the CBM+1 down the group offers the prospect that this could indeed be possible. The most obvious method would be to make Zn_2NAt. This could close the gap completely, and also depends on what structure it takes — the gap in the Pnma (63) structure in Zn_2NI is 0.41 eV smaller than in the $Pna2_1$ structure. If it doesn't, doping with the iodide could potentially tune the gap. Unfortunately, At is synthetic and radioactive with a half-life of 5.41–8.1 hours,[193] so would make a poor choice in the real world, so another option might be to substitute the N for a heavier pnictogen. This might lower the CBM+1 in the same way as the heavier halides have, and with two groups of elements adjust, could enable precise engineering of the band structure. On the other hand, heavier halides have reduced the stability of Zn_2NX, and this may too happen with heavier pnictogens. This may be an intrinsic flaw in the mixed anion premise, with more complex structures having better thermoelectric properties at the cost of a smaller temperature range. Nevertheless, with decomposition temperatures of 750 °C and 600 °C,[187] there is plenty of room to decrease into, and plenty of devices and processes operating at lower temperatures which could have their waste heat recycled, and earth abundant materials are prime candidates for such widespread applications.

24 CONCLUSION

We have studied the effectiveness of anion substitution as a means of enhancing the thermoelectric properties of ZnO, by transforming it into Zn_2NX (X = Cl, Br, I). This resulted in a reduction of the lattice thermal conductivity of 35–53 times when X = Br or I, which we have attributed to the heavy halide atoms slowing down the phonons and acting as rattlers to effectively scatter the low-frequency phonons. The electrical conductivity is also enhanced, due in small part to a decreased electron effective mass, but predominantly due to the reduced scattering. Partly this is due to the effective removal of the piezoelectric scattering, and partly due to the enhanced screening of the polar optical phonon and ionised impurity scattering by the large, electron-rich halide ions, particularly the iodide. While the removal of the piezoelectric scattering is particular to piezoelectric materials, the enhanced screening should apply to any instance of anion substitution into relatively heavy ions, showing the effectiveness of this method beyond the initial intention of reducing the lattice thermal conductivity. The electrical conductivity dependence is still less predictable than the lattice thermal conductivity due to the more complex processes governing it, but this will help, at least. An added benefit in this instance is that the optimal carrier concentration has decreased, making doping it to this level more tractable, but there is also the disadvantage of the lower thermal stability blocking off the highest ZTs. The overall effect is that compared to ZnO's optimal ZT of 0.125 with 1.59×10^{20} carriers cm^{-3} at 1,800 K in the y direction, Zn_2NBr's is 0.605 with 2.68×10^{19} carriers cm^{-3} at 1,000 K in the y direction and Zn_2NI's is 0.672 with 3.16×10^{19} carriers cm^{-3} at 800 K in the z direction. This enhancement of more than five times is much greater than nanostructuring ZnO to 20 nm, which enhances the ZT by 1.5 times, due to the greater lattice thermal conductivity reduction and synergistic increase of electrical conductivity. Furthermore, the low electronic scattering and high phononic scattering of Zn_2NX render nanostructuring them counterproductive. This makes anion substitution, at least for ZnO but likely for other materials too, an effective alternative to nanostructuring, which reduces lattice thermal conductivity but also enhances rather than reduces the electrical conductivity.

Still, more work needs to be done before these materials can be used in real life. In order to reach the high carrier concentrations required, Zn_2NX needs to be heavily doped. While it needs fewer dopants than than ZnO, the increased number of constituents places it in a more complex phase-space, which may reduce the stability window in which it can be doped. A preliminary step may be to calculate the band alignment relative to the vacuum energy level and ZnO in order to to calculate the electron affinity and ionisation potential, to confirm that it is likely to be n-type. If it is still viable, and the structural questions from the last part have been settled, research will still need to be done into the device architecture, including the material for the p-type leg, as well as contact materials.

In an unexpected twist, as the anion increases in size from Cl to I, there is a large decrease in the CBM+1 energy around the Γ point. While this renders Zn_2NX coloured when doped, it raises the tantalising possibility of band engineering an increased Seebeck coefficient if several bands can be made to coincide at the CBM, potentially reducing one of the main disadvantages of these materials. We propose that changing the pnictogen may be a good place to start. Overall, anion substitution is an effective method of enhancing the thermoelectric properties of known materials, showing a five times enhancement from ZnO to Zn_2NX, a class of materials that while promising in itself also opens up an array of potentially even better alternatives for future research.

Part VIII

Conclusions

We have studied methods to find new earth-abundant thermoelectric materials. We first designed and wrote a Python package to make the analysis of thermoelectrics more efficient and less intimidating, and used it to assist in looking at two methods to find new thermoelectric materials. The first was straightforwardly looking at the literature for materials with promising characteristics, such as a complex crystal structure and traits conducive to high electrical conductivity. We found we were able to isolate the traits we expected in $BaBi_2O_6$, but they did not reach optimal levels below the decomposition temperature. Then, we examined anion substitution as a means to enhance the ZT of ZnO as Zn_2NX (X = Cl, Br, I). This was surprisingly effective, as it not only reduced the lattice thermal conductivity, but enhanced the electrical conductivity, a synergy we now expect to be plausible in a wide range of materials where a small anion is replaced by at least one larger one. Unfortunately, this anion substitution also resulted in a reduction of the decomposition temperature, limiting ZT gains. It is probable this is a common limitation to using complex structured materials, anion substituted or otherwise, due to a more complex phase space and structure. Nevertheless, the decomposition temperatures of 600–1,000 K are still high, and many applications fall below them. In these cases, the sources are not as spacially concentrated, and are more likely to be placed closer to more living things, making the use of earth-abundant, non-toxic materials especially important. The diversity of options in anion substituted materials in particular, with two groups of anions to adjust, offers the option of fine-tuning materials, e.g. for band-engineering a high Seebeck coefficient, an option which looks promising in Zn_2NX and materials derived thereof, even if this means lowering the thermal stability further. Overall, we have studied two methods which have successfully found low thermal conductivity, high electrical thermal conductivity (i.e. phonon-glass electron-crystal) materials using relatively earth abundant materials. While these methods won't necessarily find the next ultra-high temperature thermoelectric, they show great promise for finding lower temperature thermoelectrics, for which earth-abundant materials are ideally suited, and anion substitution in particular has the potential to find the holy trifecta of high Seebeck, high electrical conductivity and low lattice thermal conductivity in one material.

Part IX

Appendices

A BaBi$_2$O$_6$

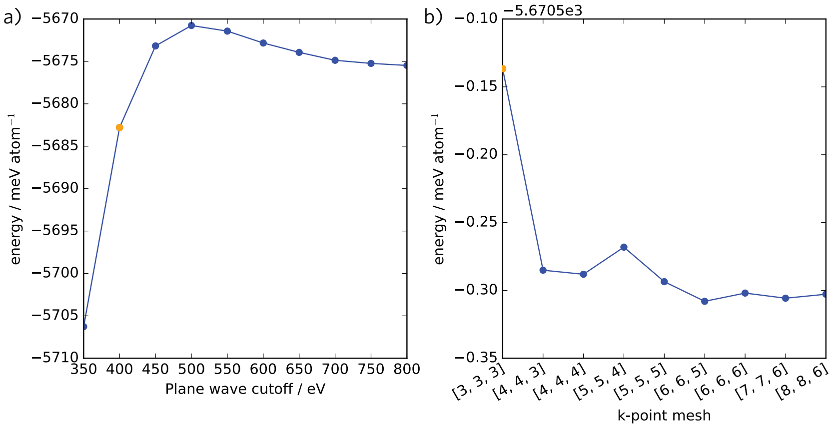

Figure A.1: Convergence of the energy of BaBi$_2$O$_6$ against plane-wave energy cutoff and k-point mesh. The orange dots show the converged value to $5\,\mathrm{meV\,atom^{-1}}$, which are the minimum values used in all subsequent calculations.

B Zn$_2$NX (X = Cl, Br, I)

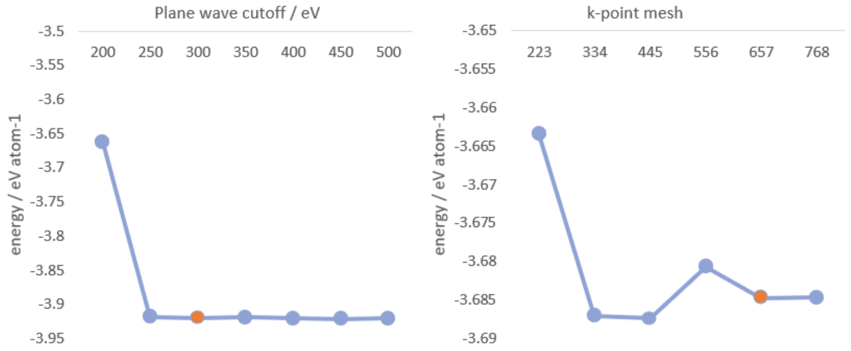

Figure B.1: Convergence of the energy of Zn$_2$NCl against plane-wave energy cutoff and k-point mesh. The orange dots show the converged value to 5 meV atom^{-1}, which are the minimum values used in all subsequent calculations.

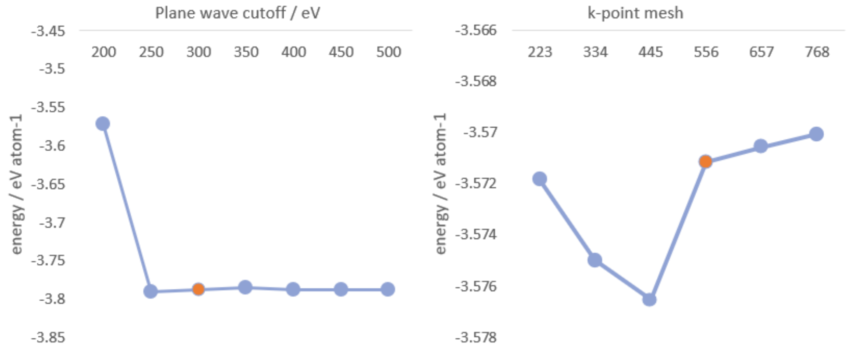

Figure B.2: Convergence of the energy of Zn$_2$NBr against plane-wave energy cutoff and k-point mesh. The orange dots show the converged value to 5 meV atom^{-1}, which are the minimum values used in all subsequent calculations.

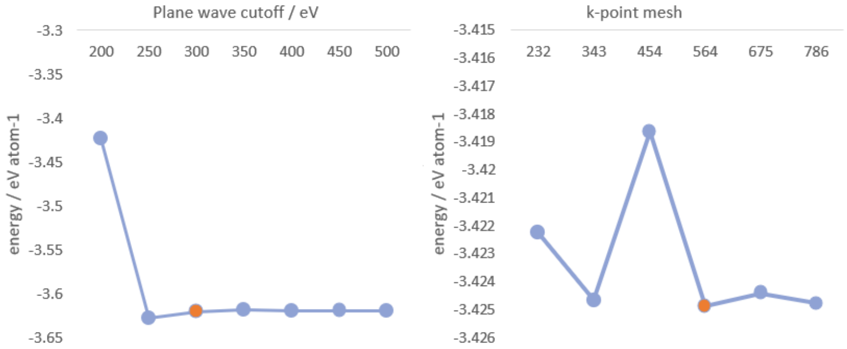

Figure B.3: Convergence of the energy of Zn_2NI in the Pnma (62) structure against plane-wave energy cutoff and k-point mesh. The orange dots show the converged value to 5 meV atom^{-1}, which are the minimum values used in all subsequent calculations.

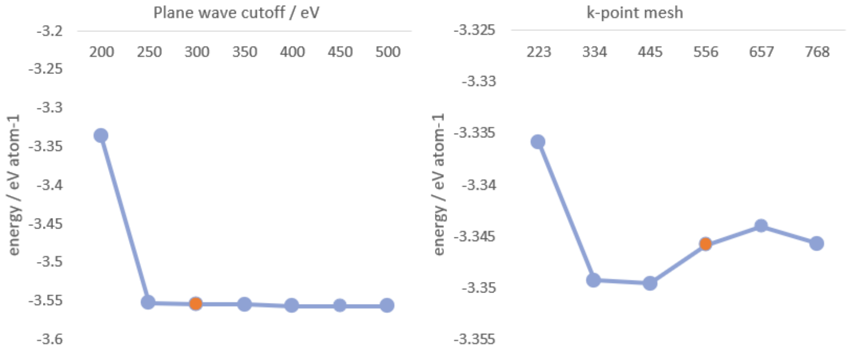

Figure B.4: Convergence of the energy of Zn_2NI in the $Pna2_1$ (33) structure against plane-wave energy cutoff and k-point mesh. The orange dots show the converged value to 5 meV atom^{-1}, which are the minimum values used in all subsequent calculations.

LIST OF FIGURES

BIBLIOGRAPHY

[1] Horowitz, C. A. Paris Agreement. *Int. Leg. Mater.* **2016**, *55*, 740.

[2] IPCC, In *Climate Change 2022: Mitigation of Climate Change. Contribution of Working Group III to the Sixth Assessment Report of the Intergovernmental Panel on Climate Change*; Shukla, P., Skea, J., Slade, R., Khourdajie, A. A., van Diemen, R., McCollum, D., Pathak, M., Some, S., Vyas, P., Fradera, R., Belkacemi, M., Hasija, A., Lisboa, G., Malley, S. L. J., Eds.; Cambridge University Press, Cambridge, UK and New York, NY, USA, 2022.

[3] Ward, P. *The Medea Hypothesis*; Princeton University Press, 2009.

[4] IPCC, In *Climate Change 2022: Impacts, Adaptation, and Vulnerability. Contribution of Working Group II to the Sixth Assessment Report of the Intergovernmental Panel on Climate Change*; Pörtner, H. O., Roberts, D. C., Tignor, M., Poloczanska, E. S., Mintenbeck, K., Alegría, A., Craig, M., Langsdorf, S., Löschke, S., Möller, V., Okem, A., Rama, B., Eds.; Cambridge University Press. Cambridge University Press, Cambridge, UK and New York, NY, USA, 2022.

[5] Lenton, T. M.; Held, H.; Kriegler, E.; Hall, J. W.; Lucht, W.; Rahmstorf, S.; Schellnhuber, H. J. Tipping Elements in the Earth's Climate System. *Proc. Natl. Acad. Sci.* **2008**, *105*, 1786–1793.

[6] McKay, D. A.; Staal, A.; Abrams, J. F.; Winkelmann, R.; Sakschewski, B.; Loriani, S.; Fetzer, I.; Cornell, S. E.; Rockström, J.; Lenton, T. M. Updated Assessment Suggests ¿ 1.5° C Global Warming Could Trigger Multiple Climate Tipping Points. *Science* **2022**, *377*, 944.

[7] King, A. D.; Harrington, L. J. The Inequality of Climate Change from 1.5 to 2 °C of Global Warming. *Geophysical Research Letters* **2018**, *45*, 5030–5033.

[8] Arrhenius, S. On the Influence of Carbonic Acid in the Air Upon the Temperature of the Ground. *Philos. Mag.* **1896**, *41*, 237.

[9] Crawford, E. Arrhenius' 1896 Model of the Greenhouse Effect in Context. *Ambio* **1997**, *26*, 6.

[10] Climate at a Glance: Global Time Series. online, 2022; `https://www.ncdc.noaa.gov/cag/`.

[11] Mora, C.; McKenzie, T.; Gaw, I. M.; Dean, J. M.; von Hammerstein, H.; Knudson, T. A.; Setter, R. O.; Smith, C. Z.; Webster, K. M.; Patz, J. A.; Franklin, E. C. Over Half of Known Human Pathogenic Diseases can be Aggravated by Climate Change. *Nat. Clim. Change* **2022**, *12*, 869.

[12] Vermeulen, S. J.; Campbell, B. M.; Ingram, J. S. I. Climate Change and Food Systems. *Annu. Rev. Environ. Resour.* **2012**, *37*, 195.

[13] Koubi, V. Climate Change and Conflict. *Annu. Rev. Polit. Sci.* **2019**, *22*, 343.

[14] Ritchie, H.; Roser, M.; Rosado, P. Energy. *Our World in Data* **2022**, https://ourworldindata.org/energy.

[15] Firth, A.; Zhang, B.; Yang, A. Quantification of Global Waste Heat and its Environmental Effects. *Appl. Energy* **2019**, *235*, 1314.

[16] Carnot, S. *Réflexions sur la Puissance Motrice du Feu et sur les Machines Propres à Développer Cette Puissance*; Bachelier, 1824.

[17] Ebling, D. G.; Krumm, A.; Pfeiffelmann, B.; Gottschald, J.; Bruchmann, J.; Benim, A. C.; Adam, M.;

Herbertz, R. R.; Stunz, A. Development of a System for Thermoelectric Heat Recovery from Stationary Industrial Processes. *J. Electron. Mater.* **2016**, *45*, 3433.

[18] Starner, T. Human-Powered Wearable Computing. *IBM Systems Journal* **1996**, *35*, 618.

[19] Ebrahimi, A.; Shayegani, A.; Zarandi, M. M. Thermal Performance of Sustainable Element in Moayedi Icehouse in Iran. *Int. J. Archit. Herit.* **2021**, *15*, 740.

[20] Alston, T. A. Anesthesia-Related Ramifications of Benjamin Franklin's Ether-Based Refrigeration. *Journal of Anesthesia History* **2020**, *6*, 29.

[21] Kohlhase, C. E.; Penzo, P. A. Voyager Mission Description. *Space Sci. Rev.* **1977**, *21*, 77.

[22] Molina, M. J.; Rowland, F. S. Stratospheric Sink for Chlorofluoromethanes: Chlorine Atom-Catalysed Destruction of Ozone. *Nature* **1974**, *249*, 810.

[23] Devotta, S.; Waghmare, A. V.; Sawant, N. N.; Domkundwar, B. M. Alternatives to HCFC-22 for Air Conditioners. *Appl. Therm. Eng.* **2001**, *21*, 703.

[24] Kempf, N.; Luo, Z.-Z.; Xie, H.; Daw, J.; Kanatzidis, M. G.; Zhang, Y. Thermoelectric Properties of High-Performance *n*-Type Lead Telluride Measured in Situ in a Nuclear Reactor Core. *J. Mater. Chem. A* **2022**, *10*, 21266.

[25] Shockley, W.; Queisser, H. J. Detailed Balance Limit of Efficiency of *p–n* Junction Solar Cells. *Journal of Appl. Phys.* **1961**, *32*, 510.

[26] Ehrler, B.; Hutter, E. M.; Berry, J. J. The Complicated Morality of Named Inventions. *ACS Energy Lett.* **2021**, *6*, 565.

[27] Bjørk, R.; Nielsen, K. K. The Maximum Theoretical Performance of Unconcentrated Solar Photovoltaic and Thermoelectric Generator Systems. *Energy Convers. Manag.* **2018**, *156*, 264.

[28] Dubey, S.; Sarvaiya, J. N.; Seshadri, B. Temperature Dependent Photovoltaic (PV) Efficiency and its Effect on PV Production in the World — a Review. *Enrgy Proced.* **2013**, *33*, 311.

[29] Kumar, N. M.; Kanchikere, J.; Mallikarjun, P. Floatovoltaics: Towards Improved Energy Efficiency, Land and Water Management. *Int. J. Civ. Eng. Technol.* **2018**, *9*, 1089.

[30] Volta, A. Nuova Memoria Sull'Elettricità Animale. *Annali di Chimica e Storia Naturale* **1794**, *5*, 132.

[31] Seebeck, T. J. In *Ostwald's Klassiker der Exakten Wissenschaften*, 1st ed.; Engelmann, W., Ed.; Deutsche Akademie der Wissenschaften zu Berlin: Leipzig, 1822; Vol. 70; p 265.

[32] Ørsted, H. C. Nouvelles Expériences de M. Seebeck sur les Actions Électro-magnetiques. *Ann. Chim.* **1823**, *2*, 199.

[33] Ørsted, H. C. Notiz von Neuen Electrisch-Magnetischen Versuchen des Herrn Seebeck in Berlin. *Ann. Phys.* **1823**, *4*, 430.

[34] Peltier, J. C. A. Nouvelles Expériences sur la Caloricité des Courants Électrique. *Ann. Chim. Phys.* **1834**, *56*, 371.

[35] Thomson, W. On a Mechanical Theory of Thermo-Electric Currents. *Proceedings of the Royal society of Edinburgh* **1857**, *3*, 91.

[36] Franz, R.; Wiedemann, G. Über die Wärme-Leitungsfähigkeit der Metalle. *Ann. Phys.* **1853**, *165*, 497.

[37] Slack, G. A. In *CRC Handbook of Thermoelectrics*, 1st ed.; Rowe, D. M., Ed.; CRC Press: Boca Raton, 1995; Chapter 34, pp 407–440.

[38] Nolas, G. S.; Poon, J.; Kanatzidis, M. G. Recent Developments in Bulk Thermoelectric Materials. *MRS Bull.* **2006**, *31*, 199.

[39] Kanatzidis, M. G. Advances in Thermoelectrics: From Single Phases to Heirachical Nanostructures and Back. *MRS Bull.* **2015**, *40*, 687.

[40] Hsu, K. F.; Loo, S.; Guo, F.; Chen, W.; Dyck, J. S.; Uher, C.; Hogan, T.; Polychroniadis, E. K.; Kanatzidis, M. G. Cubic $AgPb_mSbTe_{2+m}$: Bulk Thermoelectric Materials with High Figure of Merit. *Science* **2004**, *303*, 818.

[41] Biswas, K.; He, J.; Blum, I. D.; Wu, C.-I.; Hogan, T. P.; Seidman, D. N.; Dravid, V. P.; Kanatzidis, M. G. High-Performance Bulk Thermoelectrics with All-Scale Hierarchical Architectures. *Nature* **2012**, *489*, 414.

[42] Korkosz, R. J.; Chasapis, T. C.; Lo, S.-h.; Doak, J. W.; Kim, Y. J.; Wu, C.-I.; Hatzikraniotis, E.; Hogan, T. P.; Seidman, D. N.; Wolverton, C.; Dravid, V. P.; Kanatzidis, M. G. High ZT in p-Type $(PbTe)_{1-2x}(PbSe)_x(PbS)_x$ Thermoelectric Materials. *J. Am. Chem. Soc.* **2014**, *136*, 3225.

[43] Wu, H. J.; Zhao, L.-D.; Zheng, F. S.; Wu, D.; Pei, Y. L.; Tong, X.; Kanatzidis, M. G.; He, J. Q. Broad Temperature Plateau for Thermoelectric Figure of Merit ZT > 2 in Phase-Separated $PbTe_{0.7}S_{0.3}$. *Nat. Commun.* **2014**, *5*, 4515.

[44] Fu, T.; Yue, X.; Wu, H.; Fu, C.; Zhu, T.; Liu, X.; Hu, L.; Ying, P.; He, J.; Zhao, X. Enhanced Thermoelectric Performance of PbTe Bulk Materials with Figure of Merit zT

> 2 by Multi-Functional Alloying. *J. Materiomics* **2016**, *2*, 141.

[45] Venkatasubramanian, R.; Colpitts, T.; Watko, E.; Lamvik, M.; El-Masry, N. MOCVD of Bi_2Te_3, Sb_2Te_3 and their Superlattice Structures for Thin-Film Thermoelectric Applications. *J. Cryst. Growth* **1997**, *170*, 817.

[46] Zhao, L.-D.; Lo, S.-H.; Zhang, Y.; Sun, H.; Tan, G.; Uher, C.; Wolverton, C.; Dravid, V. P.; Kanatzidis, M. G. Ultralow Thermal Conductivity and High Thermoelectric Figure of Merit in SnSe Crystals. *Nature* **2014**, *508*, 373.

[47] Chen, Z.-G.; Shi, X.; Zhao, L.-D.; Zou, J. High-Performance SnSe Thermoelectric Materials: Progress and Future Challenge. *Prog. Mater Sci.* **2018**, *97*, 283.

[48] Snyder, G. J.; Toberer, E. S. Complex Thermoelectric Materials. *Nat. Mater.* **2008**, *7*, 105.

[49] Bädeker, K. Über die Elektrische Leitfähigkeit und die Thermoelektrische Kraft einiger Schwermetallverbindungen. *Ann. Phys.* **1907**, *327*, 749.

[50] Mattox, D.; Mattox, V. Review of Transparent Conductive Oxides (TCO). Society of Vacuum Coaters. 2007.

[51] Afre, R. A.; Sharma, N.; Sharon, M.; Sharon, M. Transparent Conducting Oxide Films for Various Applications: A Review. *Reviews on advanced materials science* **2018**, *53*, 79.

[52] Takahashi, K.; A, Y.; A, S. *Wide bandgap semiconductors: fundamental properties and modern photonic and electronic devices*; Springer, 2007.

[53] Rumble Jr., J. R., Lide, D. R., Bruno, T. J., Eds. *CRC Handbook of Chemistry and Physics*, 98th ed.; CRC Press, 2017.

[54] Nain, P.; Kumar, A. Theoretical Evaluation of Metal Release Potential of Emerging Third Generation Solar Photovoltaics. *Sol. Energ. Mat. Sol.* **2021**, *227*, 111120.

[55] Nain, P.; Kumar, A. A State-of-Art Review on End-of-Life Solar Photovoltaics. *Journal of Cleaner Production* **2022**, 130978.

[56] Shannon, R. D.; Gillson, J. L.; Bouchard, R. J. Single Crystal Synthesis and Electrical Properties of $CdSnO_3$, Cd_2SnO_4, In_2TeO_6 and $Cdln_2O_4$. *J. Phys. Chem. Solids* **1977**, *38*, 877.

[57] Spooner, K. B.; Ganose, A. M.; Scanlon, D. O. Assessing the Limitations of Transparent Conducting Oxides as Thermoelectrics. *J. Mater. Chem. A* **2020**, *8*, 11948.

[58] Gibbs, Z. M.; Ricci, F.; Li, G.; Zhu, H.; Persson, K.; Ceder, G.; Hautier, G.; Jain, A.; Snyder, G. J. Effective Mass and Fermi Surface Complexity Factor from *ab Initio* Band Structure Calculations. *npj Comput. Mater.* **2017**, *3*, 8.

[59] Nolas, G. S.; Sharp, J.; Goldsmid, H. J. *Thermoelectrics*, 1st ed.; Springer Series in Materials Science; Springer, 2001.

[60] Zhang, J.; Iversen, B. B. Fermi Surface Complexity, Effective Mass, and Conduction Band Alignment in n-Type Thermoelectric $Mg_3Sb_{2-x}Bi_x$ from First Principles Calculations. *J. Appl. Phys.* **2019**, *126*, 085104.

[61] Skelton, J. M.; Parker, S. C.; Togo, A.; Tanaka, I.; Walsh, A. Thermal Physics of the Lead Chalcogenides PbS, PbSe, and PbTe from First Principles. *Phys. Rev. B* **2014**, *89*, 205203.

[62] Togo, A.; Chaput, L.; Tanaka, I.; Hug, G. First-Principles Phonon Calculations of Thermal Expansion in Ti_3SiC_2, Ti_3AlC_2, and Ti_3GeC_2. *Phys. Rev. B* **2010**, *81*, 174301.

[63] Delaire, O.; Ma, J.; Marty, K.; May, A. F.; McGuire, M. A.; Du, M.-H.; Singh, D. J.; Podlesnyak, A.; Ehlers, G.; Lumsden, M. D.; Sales, B. C. Giant Anharmonic Phonon Scattering in PbTe. *Nat. Mater.* **2011**, *10*, 614.

[64] Dolyniuk, J.-A.; Owens-Baird, B.; Wang, J.; Zaikina, J. V.; Kovnir, K. Clathrate Thermoelectrics. *Mater. Sci. Eng. R Rep.* **2016**, *108*, 1.

[65] Liu, Z.-Y.; Zhu, J.-L.; Tong, X.; Niu, S.; Zhao, W.-Y. A Review of $CoSb_3$-Based Skutterudite Thermoelectric Materials. *J. Adv. Ceram.* **2020**, *9*, 647.

[66] Liu, W.-S.; Zhang, B.-P.; Li, J.-F.; Zhang, H.-L.; Zhao, L.-D. Enhanced Thermoelectric Properties in $CoSb_{3-x}Te_x$ Alloys Prepared by Mechanical Alloying and Spark Plasma Sintering. *Journal of Applied Physics* **2007**, *102*, 103717.

[67] Su, X.; Li, H.; Wang, G.; Chi, H.; Zhou, X.; Tang, X.; Zhang, Q.; Uher, C. Structure and Transport Properties of Double-Doped $CoSb_{2.75}Ge_{0.25-x}Te_x$ ($x = 0.125$–0.20) with in Situ Nanostructure. *Chem. Mater.* **2011**, *23*, 2948.

[68] Trivedi, V.; Battabyal, M.; Balasubramanian, P.; Muralikrishna, G. M.; Jain, P. K.; Gopalan, R. Microstructure and Doping Effect on the Enhancement of the Thermoelectric Properties of Ni Doped Dy Filled $CoSb_3$ Skutterudites. *Sustain. Energy Fuels* **2018**, *2*, 2687.

[69] Shi, X.; Yang, J.; Salvador, J. R.; Chi, M.; Cho, J. Y.; Wang, H.; Bai, S.; Yang, J.; Zhang, W.; Chen, L. Multiple-Filled Skutterudites: High Thermoelectric Figure of Merit Through Separately Optimizing Electrical and Thermal Transports. *J. Am. Chem. Soc.* **2011**, *133*, 7837.

[70] Rogl, G.; Sauerschnig, P.; Rykavets, Z.; Romaka, V.; Heinrich, P.; Hinterleitner, B.; Grytsiv, A.; Bauer, E.; Rogl, P.

(V, Nb)-Doped Half Heusler Alloys Based on {Ti, Zr, Hf}NiSn with High ZT. *Acta Mater.* **2017**, *131*, 336.

[71] Minnich, A.; Dresselhaus, M. S.; Ren, Z. F.; Chen, G. Bulk anostructured Thermoelectric Materials: Current Research and Future Prospects. *Energy & Environmental Science* **2009**, *2*, 466.

[72] Poudel, B.; Hao, Q.; Ma, Y.; Lan, Y.; Minnich, A.; Yu, B.; Yan, X.; Wang, D.; Muto, A.; Vashaee, D.; Chen, X.; Liu, J.; Dresselhaus, M. S.; Chen, G.; Ren, Z. High-thermoelectric performance of nanostructured bismuth antimony telluride bulk alloys. *Science* **2008**, *320*, 634.

[73] Terasaki, I.; Sasago, Y.; Uchinokura, K. Large Thermoelectric Power in $NaCo_2O_4$ Single Crystals. *Phys. Rev. B* **1997**, *56*, R12685.

[74] Ma, Q. H.; Wang, Q. W.; Lu, P. X.; Hou, Y. G. Electronic Structures and Thermoelectric Properties of $NaCo_2O_4$ Thermoelectric Material. Advanced Materials Research. 2011; p 2051.

[75] Terasaki, I. Transport Properties and Electronic States of the Thermoelectric Oxide $NaCo_2O_4$. *Phys. B Condens. Matter* **2003**, *328*, 63.

[76] Kurosaki, K.; Muta, H.; Uno, M.; Yamanaka, S. Thermoelectric Properties of $NaCo_2O_4$. *J. Alloys Compd.* **2001**, *315*, 234.

[77] Jakubczyk, E. M.; Mapp, A.; Chung, C. C.; Sansom, C. L.; Jones, J. L.; Dorey, R. A. Enhancing Thermoelectric Properties of $NaCo_2O_4$ Ceramics Through Na Pre-Treatment Induced Nano-Decoration. *J. Alloys Compd.* **2019**, *788*, 91.

[78] Fujita, K.; Mochida, T.; Nakamura, K. High-Temperature Thermoelectric Properties of $Na_xCoO_{2-\delta}$ Single Crystals. *Jpn. J. Appl. Phys.* **2001**, *40*, 4644.

[79] Funahashi, R.; Shikano, M. $Bi_2Sr_2Co_2O_y$ Whiskers with High Thermoelectric Figure of Merit. *Appl. Phys. Lett.* **2002**, *81*, 1459.

[80] Weller, M.; Sacchetti, A.; Ott, H. R.; Mattenberger, K.; Batlogg, B. Melting of the Na Layers in Solid $Na_{0.8}CoO_2$. *Phys. Rev. Lett.* **2009**, *102*, 056401.

[81] Assadi, M. H. N. Hf Doping for Enhancing the Thermoelectric Performance in Layered $Na_{0.75}CoO_2$. *Mater. Today:. Proc.* **2021**, *42*, 1542.

[82] Ohtaki, M. Recent Aspects of Oxide Thermoelectric Materials for Power Generation from Mid-to-High Temperature Heat Source. *J. Ceram. Soc. Jpn.* **2011**, *119*, 770.

[83] Einhorn, M.; Williamson, B. A. D.; Scanlon, D. O. Computational Prediction of the Thermoelectric Performance of LaZnOPn (Pn = P, As). *J. Mater. Chem.A* **2020**, *8*, 7914.

[84] Li, J.-B.; Wang, J.; Li, J.-F.; Li, Y.; Yang, H.; Yu, H.-Y.; Ma, X.-B.; Yaer, X.; Liu, L.; Miao, L. Broadening the Temperature Range for High Thermoelectric Performance of Bulk Polycrystalline Strontium Titanate by Controlling the Electronic Transport Properties. *J. Mater. Chem. C* **2018**, *6*, 7594.

[85] Kovalevsky, A. V.; Yaremchenko, A. A.; Populoh, S.; Thiel, P.; Fagg, D. P.; Weidenkaff, A.; Frade, J. R. Towards a High Thermoelectric Performance in Rare-Earth Substituted $SrTiO_3$: Effects Provided by Strongly-Reducing Sintering Conditions. *Phys. Chem. Chem. Phys.* **2014**, *16*, 26946.

[86] Wang, J.; Zhang, B.-Y.; Kang, H.-J.; Li, Y.; Yaer, X.; Li, J.-F.; Tan, Q.; Zhang, S.; Fan, G.-H.; Liu, C.-Y.; Miao, L.; Nan, D.; Wang, T.-M.; Zhao, L.-D. Record High Thermoelectric Performance in Bulk $SrTiO_3$ via Nano-Scale Modulation Doping. *Nano Energy* **2017**, *35*, 387.

[87] Daniels, L. M.; Savvin, S. N.; Pitcher, M. J.; Dyer, M. S.; Claridge, J. B.; Ling, S.; Slater, B.; Corà, F.; Alaria, J.; Rosseinsky, M. J. Phonon-Glass Electron-Crystal Behaviour by A Site Disorder in n-Type Thermoelectric Oxides. *Energy Environ. Sci.* **2017**, *10*, 1917.

[88] Wang, Y.; Sui, Y.; Fan, H.; Wang, X.; Su, Y.; Su, W.; Liu, X. High Temperature Thermoelectric Response of Electron-Doped $CaMnO_3$. *Chem. Mater.* **2009**, *21*, 4653.

[89] Zhang, F. P.; Lu, Q. M.; Zhang, X.; Zhang, J. X. Electrical Transport Properties of $CaMnO_3$ Thermoelectric Compound: a Theoretical Study. *J. Phys. Chem. Solids* **2013**, *74*, 1859.

[90] Molinari, M.; Tompsett, D. A.; Parker, S. C.; Azough, F.; Freer, R. Structural, Electronic and Thermoelectric Behaviour of $CaMnO_3$ and $CaMnO_{(3-\delta)}$. *J. Mater. Chem.A* **2014**, *2*, 14109.

[91] Tsubota, T.; Ohtaki, M.; Eguchi, K.; Arai, H. Thermoelectric Properties of Al-Doped ZnO as a Promising Oxide Material for High-Temperature Thermoelectric Conversion. *J. Mater. Chem.* **1997**, *7*, 85.

[92] Ohtaki, M.; Tsubota, T.; Eguchi, K.; Arai, H. High-Temperature Thermoelectric Properties of $(Zn_{1-x}Al_x)O$. *J. Appl. Phys.* **1996**, *79*, 1816.

[93] Bérardan, D.; Guilmeau, E.; Maignan, A.; Raveau, B. In_2O_3: Ge, a Promising n-Type Thermoelectric Oxide Composite. *Solid State Commun.* **2008**, *146*, 97.

[94] Ohtaki, M.; Araki, K.; Yamamoto, K. High Thermoelectric Performance of Dually Doped ZnO Ceramics. *J. Electron. Mater.* **2009**, *38*, 1234.

[95] Lee, J. G. *Computational Materials Science: An Introduction*; CRC Press: Boca Raton, 2011.

[96] Schrödinger, E. An Undulatory Theory of the Mechanics of Atoms and Molecules. *Phys. Rev.* **1926**, *28*, 1049.

[97] Born, M.; Oppenheimer, R. Zur Quantentheorie der Molekeln. *Ann. Phys.* **1927**, *389*, 457.

[98] Hartree, D. R. The Wave Mechanics of an Atom with a Non-Coulomb Central Field. Part I. Theory and Methods. *Math. Proc. Camb. Philos. Soc.* **1928**, *24*, 89.

[99] Fock, V. Näherungsmethode zur Lösung des Quantenmechanischen Mehrkörperproblems. *Z. Phys. A* **1930**, *61*, 126.

[100] Slater, J. C. The Theory of Complex Spectra. *Phys. Rev.* **1929**, *34*, 1293.

[101] Pauli, W. Über den Zusammenhang des Abschlusses der Elektronengruppen im Atom mit der Komplexstruktur der Spektren. *Z. Phys. A* **1925**, *31*, 765.

[102] Hohenberg, P.; Kohn, W. Inhomogeneous Electron Gas. *Phys. Rev.* **1964**, *136*, B864.

[103] Kohn, W.; Sham, L. J. Self-Consistent Equations Including Exchange and Correlation Effects. *Phys. Rev.* **1965**, *140*, A1133.

[104] Martin, R. M. *Electronic Structure: Basic Theory and Practical Methods*; Cambridge University Press, 2004; p 135–151.

[105] Perdew, J. P.; Burke, K.; Ernzerhof, M. Generalized Gradient Approximation Made Simple. *Phys. Rev. Lett.* **1996**, *77*, 3865.

[106] Perdew, J. P.; Chevary, J. A.; Vosko, S. H.; Jackson, K. A.; Pederson, M. R.; Singh, D. J.; Fiolhais, C. Atoms, Molecules, Solids, and Surfaces: Applications of the Generalized Gradient Approximation for Exchange and Correlation. *Phys. Rev. B* **1992**, *46*, 6671.

[107] Nguimdo, G. M. D.; Joubert, D. P. A Density Functional (PBE, PBEsol, HSE06) Study of the Structural, Electronic and Optical Properties of the Ternary Compounds $AgAlX_2$ (X= S, Se, Te). *Eur. Phys. J. B* **2015**, *88*, 113.

[108] De La Pierre, M.; Orlando, R.; Maschio, L.; Doll, K.; Ugliengo, P.; Dovesi, R. Performance of Six Functionals (LDA, PBE, PBESOL, B3LYP, PBE0, and WC1LYP) in the Simulation of Vibrational and Dielectric Properties of Crystalline Compounds. The Case of Forsterite Mg_2SiO_4. *J. Comput. Chem.* **2011**, *32*, 1775.

[109] He, L.; Liu, F.; Hautier, G.; Oliveira, M. J. T.; Marques, M. A.; Vila, F. D.; Rehr, J. J.; Rignanese, G.-M.; Zhou, A. Accuracy of Generalized Gradient Approximation Functionals for Density-Functional Perturbation Theory Calculations. *Phys. Rev. B* **2014**, *89*, 064305.

[110] Perdew, J. P.; Ruzsinszky, A.; Csonka, G. I.; Vydrov, O. A.; Scuseria, G. E.; Constantin, L. A.; Zhou, X.; Burke, K. Restoring the Density-Gradient Expansion for Exchange in Solids and Surfaces. *Phys. Rev. Lett.* **2008**, *100*, 136406.

[111] Skelton, J. M.; Tiana, D.; Parker, S. C.; Togo, A.; Tanaka, I.; Walsh, A. Influence of the Exchange–Correlation Functional on the Quasi-Harmonic Lattice Dynamics of II–VI Semiconductors. *J. Chem. Phys.* **2015**, *143*, 064710.

[112] Tran, F.; Blaha, P. Accurate Band Gaps of Semiconductors and Insulators with a Semilocal Exchange-Correlation Potential. *Phys. Rev. Lett.* **2009**, *102*, 226401.

[113] Becke, A. D.; Johnson, E. R. A Simple Effective Potential for Exchange. *J. Chem. Phys.* **2006**, *124*, 221101.

[114] Waroquiers, D.; Lherbier, A.; Miglio, A.; Stankovski, M.; Poncé, S.; Oliveira, M. J. T.; Giantomassi, M.; Rignanese, G.-M.; Gonze, X. Band Widths and Gaps from the Tran-Blaha Functional: Comparison with Many-Body Perturbation Theory. *Phys. Rev. B* **2013**, *87*, 075121.

[115] Heyd, J.; Scuseria, G. E.; Ernzerhof, M. Hybrid Functionals Based on a Screened Coulomb Potential. *J. Chem. Phys.* **2003**, *118*, 8207.

[116] Heyd, J.; Scuseria, G. E. Efficient Hybrid Density Functional Calculations in Solids: Assessment of the Heyd–Scuseria–Ernzerhof Screened Coulomb Hybrid Functional. *J. Chem. Phys.* **2004**, *121*, 1187.

[117] Heyd, J.; Peralta, J. E.; Scuseria, G. E.; Martin, R. L. Energy Band Gaps and Lattice Parameters Evaluated with the Heyd–Scuseria–Ernzerhof Screened Hybrid Functional. *J. Chem. Phys.* **2005**, *123*, 174101.

[118] Chen, S.; Gong, X. G.; Walsh, A.; Wei, S.-H. Crystal and Electronic Band Structure of Cu_2ZnSnX_4 (X= S and Se) Photovoltaic Absorbers: First-Principles Insights. *Appl. Phys. Lett.* **2009**, *94*, 041903.

[119] Janesko, B. G.; Henderson, T. M.; Scuseria, G. E. Screened Hybrid Density Functionals for Solid-State Chemistry and Physics. *Phys. Chem. Chem. Phys.* **2009**, *11*, 443.

[120] Scanlon, D. O.; Morgan, B. J.; Watson, G. W.; Walsh, A. Acceptor Levels in p-Type Cu_2O: Rationalizing Theory and Experiment. *Phys. Rev. Lett.* **2009**, *103*, 096405.

[121] Stroppa, A.; Kresse, G. Unraveling the Jahn-Teller Effect in Mn-doped GaN Using the Heyd-Scuseria-Ernzerhof Hybrid Functional. *Phys. Rev. B* **2009**, *79*, 201201.

[122] Allen, J. P.; Scanlon, D. O.; Watson, G. W. Electronic Structure of Mixed-Valence Silver Oxide AgO from Hybrid Density-Functional Theory. *Phys. Rev. B* **2010**, *81*, 161103.

[123] Oba, F.; Choi, M.; Togo, A.; Seko, A.; Tanaka, I. Native Defects in Oxide Semiconductors: a Density Functional Approach. *J. Phys.: Condens. Matter* **2010**, *22*, 384211.

[124] Stroppa, A.; Picozzi, S. Hybrid Functional Study of Proper and Improper Multiferroics. *Phys. Chem. Chem. Phys.* **2010**, *12*, 5405.

[125] Burbano, M.; Scanlon, D. O.; Watson, G. W. Sources of Conductivity and Doping Limits in CdO from Hybrid Density Functional Theory. *J. Am. Chem. Soc* **2011**, *133*, 15065.

[126] Deák, P.; Aradi, B.; Frauenheim, T. Polaronic Effects in TiO_2 Calculated by the HSE06 Hybrid Functional: Dopant Passivation by Carrier Self-Trapping. *Phys. Rev. B* **2011**, *83*, 155207.

[127] Kehoe, A. B.; Scanlon, D. O.; Watson, G. W. Nature of the Band Gap of Tl_2O_3. *Phys. Rev. B* **2011**, *83*, 233202.

[128] Scanlon, D. O.; Kehoe, A. B.; Watson, G. W.; Jones, M. O.; David, W. I. F.; Payne, D. J.; Egdell, R. G.; Edwards, P. P.; Walsh, A. Nature of the Band Gap and Origin of the Conductivity of PbO_2 Revealed by Theory and Experiment. *Phys. Rev. Lett.* **2011**, *107*, 246402.

[129] Scanlon, D. O.; Watson, G. W. Understanding the p-Type Defect Chemistry of $CuCrO_2$. *J. Mater. Chem.* **2011**, *21*, 3655.

[130] Walsh, A.; Chen, S.; Wei, S.-H.; Gong, X.-G. Kesterite Thin-Film Solar Cells: Advances in Materials Modelling of Cu_2ZnSnS_4. *Adv. Energy Mater.* **2012**, *2*, 400.

[131] Fritsch, D.; Morgan, B. J.; Walsh, A. Self-Consistent Hybrid Functional Calculations: Implications for Structural, Electronic, and Optical Properties of Oxide Semiconductors. *Nanoscale Res. Lett.* **2017**, *12*, 19.

[132] Kresse, G.; Hafner, J. *Ab Initio* Molecular Dynamics for Liquid Metals. *Phys. Rev. B* **1993**, *47*, 558.

[133] Kresse, G.; Hafner, J. *Ab Initio* Molecular Dynamics for Open-Shell Transition Metals. *Phys. Rev. B* **1993**, *48*, 13115.

[134] Kresse, G.; Hafner, J. Norm-Conserving and Ultrasoft Pseudopotentials for First-Row and Transition Elements. *J. Phys.: Condens. Matter* **1994**, *6*, 8245.

[135] Kresse, G.; Furthmüller, J. Efficiency of *ab-Initio* Total Energy Calculations for Metals and Semiconductors Using a Plane-Wave Basis Set. *Comput. Mater. Sci.* **1996**, *6*, 15.

[136] Blöchl, P. E. Projector Augmented-Wave Method. *Phys. Rev. B* **1994**, *50*, 17953.

[137] Kresse, G.; Joubert, D. From Ultrasoft Pseudopotentials to the Projector Augmented-Wave Method. *Phys. Rev. B* **1999**, *59*, 1758.

[138] Brillouin, L. Les Électrons Libres dans les Métaux et le Rôle des Reflexions de Bragg. *J. phys. radium* **1930**, *1*, 377.

[139] Pulay, P. Ab initio Calculation of Force Constants and Equilibrium Geometries in Polyatomic Molecules: I. Theory. *Mol. Phys.* **1969**, *17*, 197.

[140] Feynman, R. P. Forces in Molecules. *Phys. Rev.* **1939**, *56*, 340.

[141] Ganose, A. M.; Jackson, A. J.; Scanlon, D. O. sumo: Command-Line Tools for Plotting and Analysis of Peri-

odic *ab Initio* Calculations. *J. Open Source Softw.* **2018**, *3*, 717.

[142] Bradley, C.; Cracknell, A. *The Mathematical Theory of Symmetry in Solids: Representation Theory for Point Groups and Space Groups*; Oxford University Press, 2009.

[143] Hinuma, Y.; Pizzi, G.; Kumagai, Y.; Oba, F.; Tanaka, I. Band Structure Diagram Paths Based on Crystallography. *Comput. Mater. Sci.* **2017**, *128*, 140.

[144] Togo, A.; Tanaka, I. Spglib: a software library for crystal symmetry search. *arXiv preprint arXiv:1808.01590* **2018**,

[145] Onsager, L. Reciprocal Relations in Irreversible Processes. *Phys. Rev.* **1931**, *37*, 405.

[146] Fermi, E. Sulla Quantizzazione del Gas Perfetto Monoatomico. *Rendiconti Lincei* **1926**, *145*.

[147] Dirac, P. A. M. On the Theory of Quantum Mechanics. *Proc. R. Soc. London A.* **1926**, *112*, 661.

[148] Kim, H.-S.; Gibbs, Z. M.; Tang, Y.; Wang, H.; Snyder, G. J. Characterization of Lorenz Number with Seebeck Coefficient Measurement. *APL materials* **2015**, *3*, 041506.

[149] Madsen, G. K. H.; Singh, D. J. BoltzTraP. A Code for Calculating Band-Structure Dependent Quantities. *Comput. Phys. Commun.* **2006**, *175*, 67.

[150] Madsen, G. K. H.; Carrete, J.; Verstraete, M. J. BoltzTraP2, a Program for Interpolating Band Structures and Calculating Semi-Classical Transport Coefficients. *Comput. Phys. Commun.* **2018**, *231*, 140.

[151] Ganose, A. M.; Park, J.; Faghaninia, A.; Woods-Robinson, R.; Persson, K. A.; Jain, A. Efficient Calculation of Carrier Scattering Rates from First Principles. *Nat. Commun.* **2021**, *12*, 2222.

[152] Fröhlich, H. Electrons in Lattice Fields. *Adv. Phys.* **1954**, *3*, 325.

[153] Verdi, C.; Giustino, F. Fröhlich Electron-Phonon Vertex from First Principles. *Phys. Rev. Lett.* **2015**, *115*, 176401.

[154] Sjakste, J.; Vast, N.; Calandra, M.; Mauri, F. Wannier Interpolation of the Electron-Phonon Matrix Elements in Polar Semiconductors: Polar-Optical Coupling in GaAs. *Phys. Rev. B* **2015**, *92*, 054307.

[155] Togo, A.; Tanaka, I. First Principles Phonon Calculations in Materials Science. *Scr. Mater.* **2015**, *108*, 1.

[156] Maradudin, A. A.; Fein, A. E. Scattering of Neutrons by an Anharmonic Crystal. *Phys. Rev.* **1962**, *128*, 2589.

[157] Togo, A.; Chaput, L.; Tanaka, I. Distributions of Phonon Lifetimes in Brillouin Zones. *Phys. Rev. B* **2015**, *91*, 094306.

[158] Spooner, K. B.; Ganose, A. M.; Leung, W. W. W.; Buckeridge, J.; Williamson, B. A. D.; Palgrave, R. G.; Scanlon, D. O. $BaBi_2O_6$: A Promising *n*-Type Thermoelectric Oxide with the $PbSb_2O_6$ Crystal Structure. *Chem. Mater.* **2021**, *33*, 7441.

[159] Kavanagh, S. R.; Savory, C. N.; Scanlon, D. O.; Walsh, A. Hidden Spontaneous Polarisation in the Chalcohalide Photovoltaic Absorber $Sn_2SbS_2I_3$. *Mater. Horiz.* **2021**, *8*, 2709.

[160] Brlec, K.; Spooner, K. B.; Skelton, J. M.; Scanlon, D. O. $Y_2Ti_2O_5S_2$ — a Promising n-Type Oxysulphide for Thermoelectric Applications. *J. Mater. Chem.A* **2022**, *10*, 16813.

[161] Basso, R.; Lucchetti, G.; Zefiro, L.; Palenzona, A. Rosiaite, $PbSb_2O_6$, a New Mineral from the Cetine Mine, Siena, Italy. *Eur. J. Mineral.* **1996**, *8*, 487.

[162] Magneli, A. The Crystal Structure of Lead Metantimonate and Isomorphous Compounds. *Arkiv for Kemi, Mineralogi O Geologi* **1941**,

[163] Mizoguchi, H.; Eng, H. W.; Woodward, P. M. Probing the Electronic Structures of Ternary Perovskite and Pyrochlore Oxides Containing Sn^{4+} or Sb^{5+}. *Inorg. Chem.* **2004**, *43*, 1667.

[164] Momma, K.; Izumi, F. VESTA 3 for Three-Dimensional Visualization of Crystal, Volumetric and Morphology Data. *J. Appl. Crystallogr.* **2011**, *44*, 1272.

[165] McDonough, W. F. In *Earthquake Thermodynamics and Phase Transformations in the Earth's Interior*, 1st ed.; Teisseyre, R., Majewski, E., Eds.; Academic Press: San Diego, 2001; Chapter 1, pp 1–25.

[166] Kubelka, P. Ein Beitrag zur Optik der Farbanstriche (Contribution to the Optic of Paint). *Z. Tech. Phys.* **1931**, *12*, 593.

[167] Perdew, J. P.; Wang, Y. Accurate and Simple Density Functional for the Electronic Exchange Energy: Generalized Gradient Approximation. *Phys. Rev. B* **1986**, *33*, 8800.

[168] Saiduzzaman, M.; Yanagida, S.; Takei, T.; Moriyoshi, C.; Kuroiwa, Y.; Kumada, N. Hydrothermal Synthesis, Crystal Structure, and Visible-Region Photocatalytic Activity of $BaBi_2O_6$. *ChemistrySelect* **2017**, *2*, 4843.

[169] Funahashi, R.; Matsubara, I.; Sodeoka, S. Thermoelectric Properties of $Bi_2Sr_2Co_2O_x$ Polycrystalline Materials. *Appl. Phys. Lett.* **2000**, *76*, 2385.

[170] Zhao, L. D.; Berardan, D.; Pei, Y. L.; Byl, C.; Pinsard-Gaudart, L.; Dragoe, N. $Bi_{1-x}Sr_xCuSeO$ Oxyselenides as Promising Thermoelectric Materials. *Appl. Phys. Lett.* **2010**, *97*, 092118.

[171] Rahim, W.; Skelton, J. M.; Scanlon, D. O. α-$Bi_2Sn_2O_7$: a Potential Room Temperature n-Type Oxide Thermoelectric. *J. Mater. Chem. A* **2020**, *8*, 16405.

[172] Rahim, W.; Skelton, J. M.; Scanlon, D. O. Ca_4Sb_2O and Ca_4Bi_2O: Two Promising Mixed-Anion Thermoelectrics. *J. Mater. Chem.A* **2021**, *9*, 20417.

[173] Buckeridge, J. SC-Fermi. `https://github.com/jbuckeridge/sc-fermi`, Accessed 28 February 2018.

[174] Muta, H.; Kurosaki, K.; Yamanaka, S. Thermoelectric Properties of Rare Earth Doped $SrTiO_3$. *J. Alloys Compd.* **2003**, *350*, 292.

[175] Pei, Y.-L.; Liu, Y. Electrical and Thermal Transport Properties of Pb-Based Chalcogenides: PbTe, PbSe, and PbS. *J. Alloys Compd.* **2012**, *514*, 40.

[176] Gillet, M.; Aguir, K.; Lemire, C.; Gillet, E.; Schierbaum, K. The Structure and Electrical Conductivity of Vacuum-Annealed WO_3 Thin Films. *Thin Solid Films* **2004**, *467*, 239.

[177] Yang, G.; Tao, H.; Qin, P.; Ke, W.; Fang, G. Recent Pprogress in Electron Transport Layers for Efficient Perovskite Solar Cells. *J. Mater. Chem.A* **2016**, *4*, 3970.

[178] Loferski, J. J. Theoretical Considerations Governing the Choice of the Optimum Semiconductor for Photovoltaic Solar Energy Conversion. *J. Appl. Phys.* **1956**, *27*, 777.

[179] Goldstein, B. Properties of Photovoltaic Films of CdTe. *Phys. Rev.* **1958**, *109*, 601.

[180] Green, M. A.; Emery, K.; Hishikawa, Y.; Warta, W.; Dunlop, E. D. Solar Cell Efficiency Tables. *Prog. Photovoltaic Res. Applic.* **2000**, *23*, 805.

[181] Scarpulla, M. A. et al. CdTe-Based Thin Film Photovoltaics: Recent Advances, Current Challenges and Future Prospects. *Sol. Energ. Mat. Sol.* **2023**, *255*, 112289.

[182] Chen, W. S.; Stewart, J. M.; Stanbery, B. J.; Devaney, W. E.; Mickelsen, R. A. Development of Thin Film Polycrystalline $\mathrm{CuIn_{1-x}Ga_xSe_2}$ Solar Cells. 19th IEEE Photovoltaic Specialists Conference. 1987; p 1445.

[183] Nakamura, M.; Yamaguchi, K.; Kimoto, Y.; Yasaki, Y.; Kato, T.; Sugimoto, H. Cd-Free $\mathrm{Cu(In,Ga)(Se,S)_2}$ Thin-Film Solar Cell with Record Efficiency of 23.35 %. *IEEE J. Photovolt.* **2019**, *9*, 1863.

[184] Nitsche, R.; Sargent, D. F.; Wild, P. Crystal Growth of Quaternary 1_2246_4 Chalcogenides by Iodine Vapor Transport. *J. Cryst. Growth* **1967**, *1*, 52.

[185] Ito, K.; Nakazawa, T. Electrical and Optical Properties of Stannite-Type Quaternary Semiconductor Thin Films. *Jpn. J. Appl. Phys.* **1988**, *27*, 2094–2097.

[186] Ravindiran, M.; Praveenkumar, C. Status Review and the Future Prospects of CZTS Based Solar Cell — A novel Approach on the Device Structure and Material Modeling for CZTS Based Photovoltaic Device. *Renewable Sustainable Energy Rev.* **2018**, *94*, 317.

[187] Liu, X.; Wessel, C.; Pan, F.; Dronskowski, R. Synthesis and Single-Crystal Structure Determination of the Zinc Nitride Halides $\mathrm{Zn_2NX}$ (X= Cl, Br, I). *J. Solid State Chem.* **2013**, *203*, 31.

[188] Reeber, R. R. Lattice Parameters of ZnO from 4.2 to 296 K. *J. Appl. Phys.* **1970**, *41*, 5063.

[189] Li, X.; Tao, Y.; Lv, J.; Hu, Z.; Liu, Z.-L. Pressure-Induced Phase Transition of Zinc Nitride Chlorine. *Comput. Mater. Sci.* **2015**, *106*, 175.

[190] Hooke, R. In *De Potentia Restitutiva, or of Spring Explaining the Power of Springing Bodies*; Hooke, R., Ed.; The Royal Society, 1678; Chapter Potentia Restitutiva, or Spring, pp 1–24.

[191] Toberer, E. S.; Zevalkink, A.; Snyder, G. J. Phonon Engineering Through Crystal Chemistry. *J. Mater. Chem.* **2011**, *21*, 15843.

[192] Shannon, R. D. Revised Effective Ionic Radii and Systematic Studies of Interatomic Distances in Halides and Chalcogenides. *Acta Crystallogr. A* **1976**, *32*, 751.

[193] Kondev, F. G.; Wang, M.; Huang, W. J.; Naimi, S.; Audi, G. The NUBASE2020 Evaluation of Nuclear Physics Properties. *Chin. Phys. C* **2021**, *45*, 030001.